ISTANBUL TECHNICAL UNIVERSITY ★ GRADUATE SCHOOL

STATISTICAL INVESTIGATION OF MAGNETOSPHERE-IONOSPHERE-GROUND INTERACTION OVER MID-LATITUDES DURING GEOMAGNETIC STORMS

M.Sc. THESIS

Ezgi GÜLAY

Department of Meteorological Engineering

Atmospheric Sciences Programme

JANUARY 2023

ISTANBUL TECHNICAL UNIVERSITY ★ GRADUATE SCHOOL

STATISTICAL INVESTIGATION OF MAGNETOSPHERE-IONOSPHERE-GROUND INTERACTION OVER MID-LATITUDES DURING GEOMAGNETIC STORMS

M.Sc. THESIS

Ezgi GÜLAY
(511191030)

Department of Meteorological Engineering

Atmospheric Sciences Programme

Thesis Advisor: Prof. Dr. Zerefşan KAYMAZ

JANURARY 2023

İSTANBUL TEKNİK ÜNİVERSİTESİ ★ LİSANSÜSTÜ EĞİTİM ENSTİTÜSÜ

JEOMANYETİK FIRTINALAR SIRASINDA ORTA ENLEMLERDEKİ MANYETOSFER-İYONOSFER-YER ETKİLEŞİMİNİN İSTATİSTİKSEL OLARAK İNCELENMESİ

YÜKSEK LİSANS TEZİ

Ezgi GÜLAY
(511191030)

Meteoroloji Mühendisliği Anabilim Dalı

Atmosfer Bilimleri Programı

Tez Danışmanı: Prof. Dr. Zerefşan KAYMAZ

OCAK 2023

Ezgi GÜLAY, a M.Sc. student of ITU Graduate School student ID 511191039, successfully defended the thesis/dissertation entitled “STATISTICAL INVESTIGATION OF MAGNETOSPHERE-IONOSPHERE-GROUND INTERACTION OVER MID-LATITUDES DURING GEOMAGNETIC STORMS”, which he/she prepared after fulfilling the requirements specified in the associated legislations, before the jury whose signatures are below.

Thesis Advisor : **Prof. Dr. Zerefşan KAYMAZ** ....
Istanbul Technical University

Jury Members : **Prof. Dr. H. Sema TOPÇU** ....
Istanbul Technical University

Prof. Dr. Zafer ASLAN ....
Istanbul Aydın University

Date of Submission : 20 December 2022
Date of Defense : 17 January 2023

"The trip has been long and the cost has been high... but no great thing was ever attained easily. A long tale, like a tall Tower, must be built a stone at a time."

– Stephen King

FOREWORD

In a way that was unimaginable a century ago, technology has evolved into the most important basis of practically everything in the modern world. Everything depends on technological systems, including the most fundamental needs like communication, transportation, lighting, and heating. This requires a thorough investigation of all potential consequences and dangers associated with space weather. Even though the study of space weather is still relatively new in the scientific community, its significance is widely agreed. Thus, it is important to understand the effects of space weather over Türkiye in order to be able to take precautions against possible threats caused by space weather.

I would like to acknowledge use of data provided by NASA/GSFC's Space Physics Data Facility's CDAWeb service, WDC for Geomagnetism Kyoto, SILSO Royal Observatory of Belgium, NOAA Space Weather Prediction Center, NASA/SDO, and the AIA, EVE, and HMI science teams. Additionally I would like to acknowledge the use of data obtained from Kandilli Geomagnetic Observatory, and special thanks to Dr. Cengiz ÇELİK for his support during the data gathering process.

I would really like to thank to my advisor Prof. Dr. Zerefşan KAYMAZ for trusting and encouraging me throughout the last six years and turning this entire time into an exciting journey by inspiring me with her wisdom as being the perfect role model for an academic. I will forever be grateful to her for believing in me and doing her best to raise me as a curious and brave scientist like herself. I would also like to thank my family for their unflagging support for me to go after my dreams throughout my entire life. I also want to thank my friends Berna Yıldız, Kaan Özdoğan, Zeynep Feriha Ünal, Kutay Bölat, and Aylin Yağcı for their emotional support and continuous encouragement throughout my academic journey. Finally, I would like to thank myself for never giving up and always going forward to reach my goals.

December 2022

Ezgi GÜLAY
(Meteorological Engineer)

TABLE OF CONTENTS

Page

ABBREVIATIONS

AE	: Auroral Electrojet
CH	: Coronal Hole
CME	: Coronal Mass Ejection
Dst	: Disturbance Storm Time
EUV	: Extreme Ultraviolet
foF2	: Critical Frequency of F2 Layer
GIC	: Geomagnetically Induced Currents
H0	: Null Hypothesis
H1	: Alternative Hypothesis
HF	: High Frequency
hmF2	: Height maximum of F2 Layer
HSS	: High Speed Stream
IMF	: Interplanetary Magnetic Field
Kp	: Planetary-K
NeXtYZ	: Three-dimensional electron density inversion for Dynasonde
NPP	: No-positive Phase
Pdyn	: Dynamic Pressure
RPP	: Regular Positive Phase
SC	: Sudden Commencement
SEP	: Solar Energetic Particle
TEC	: Total Electron Content
VIPIR	: Vertically Incident Pulsed Radar

SYMBOLS

A	**:** Ampere
B	**:** Geomagnetic Field
Bx	**:** Northward Component of Geomagnetic Field
By	**:** Westward Component of Geomagnetic Field
dBx/dt	**:** Time Derivative of Northward Component of Geomagnetic Field
dBy/dt	**:** Time Derivative of Westward Component of Geomagnetic Field
dH/dt	**:** Time Derivative of Horizontal Geomagnetic Field
E	**:** Electric Field
Ex	**:** Northward Component of Electric Field
Ey	**:** Westward Component of Electric Field
IMF Bt	**:** Total Interplanetary Magnetic Field
IMF Bz	**:** Southward Component of Interplanetary Magnetic Field
N	**:** Number of Samples
ne	**:** Electron Density
r	**:** Pearson Correlation Coefficient
σ	**:** Standard Deviation

LIST OF TABLES

Page

LIST OF FIGURES

Page

STATISTICAL INVESTIGATION OF MAGNETOSPHERE-IONOSPHERE-GROUND INTERACTION OVER MID-LATITUDES DURING GEOMAGNETIC STORMS

SUMMARY

The phrase "space weather" is used to describe the conditions in space, more specifically in the solar system. Space weather is concentrated on the Sun since it is the solar system's primary energy source. The Sun's highly dynamic structure results in energy bursts that can take on a variety of shapes, including sudden energy bursts known as solar flares, bursts of plasma and magnetic field known as coronal mass ejections, and in some cases, an increase in the speed and density of the solar wind due to open magnetic field lines. Severe space weather events are what these phenomena are named since they create extreme changes in the space environment. By producing disruptions in the geomagnetic field and other aspects of the Earth's environment, extreme space weather causes the neutral conditions to shift in a negative way. Extreme space weather has an impact on satellite operations, ionospheric conductivity-based communication, and underground electrical cables.

In this study, it is aimed to understand the effects of space weather on ground and ionospheric levels over mid-latitudes. There are various types of research in the literature about these effects, yet there are three points that separate this study from the other works in the literature. The first point is that this study is done for mid-latitudes rather than the more commonly researched over high and even low latitudes. The second point is that both the measurements for ground level and the ionospheric levels are done in Türkiye, so it is a study specifically done for Türkiye. The third point is that effects on both ground and ionosphere are studied together for the same cases which is unusual among the studies in the literature.

The ground-level part of this study focuses on a phenomenon known as geomagnetically induced current (GIC). The geomagnetic field's rapid changes create an electric field that penetrates the ground itself. The power grid systems and underground pipes are affected by the electric current flowing at ground level. Although high latitude regions are the major danger area for GIC since they experience the most severe consequences there due to magnetic poles, GIC may occur everywhere, and the goal of this study is to look at GICs in the mid-latitude region.

The ionosphere, which is the conducting layer of the atmosphere, is crucial to radio wave transmission in the atmosphere and, long-distance communication across the globe and with satellites in space. Particularly with the advancements in satellite technology, understanding the variations in the ionospheric electron density becomes critically important in many of the applications of these technologies, ranging from the military and navigational systems to the cellphones which are one of extremely essential parts of our daily lives. Thus, in this study, it is aimed to understand the variations in the ionospheric electron density during the geomagnetically disturbed days.

In this study, three data sets have been used over Marmara Region, Türkiye (GG: ~ 40°N, GM: ~38°N). The first data set is geomagnetic field measurements obtained from Kandilli Geomagnetic Observatory located at Iznik (40°N, 29°E). This is the only geomagnetic observatory in Türkiye and is a member of INTERMAGNET. The 1-min resolution data is available on INTERMAGNET. 1-sec resolution data is obtained from the observatory for this study. 36 geomagnetically disturbed days between 2013 and 2015 have been chosen and those data have been used. The second data set is geomagnetic and geoelectric field measurements which obtained from the LEMI-414 magnetotelluric station located at Bozcaada (39°N, 26°E). The magnetotelluric station was operational between 2013 and 2014. Thus, 10 out of the previously mentioned 36 days were available to analyze. Both the geomagnetic and geoelectric field measurements are 1-sec resolution. The last data set is F-layer electron density measurements which obtained from the Dynasonde located at ITU Campus, Istanbul (41°N, 28°E). The data for the same 36 geomagnetically disturbed days have been used which are all 4-min resolution. Additionally, Disturbance Storm Time (Dst) index, and solar wind data from ACE and WIND spacecrafts have been used.

The study consists of two main parts which are case studies and statistical studies. For the case studies, 3 geomagnetically disturbed days have been selected based on Dst from consecutive years, 17 March 2013 which is also known as the 2013 St. Patrick storm, 27 February 2014, and 9 September 2015. Case studies are done thoroughly via time series. The phases of the geomagnetic storms are determined as initial, main, and recovery phases. The variations in different parameters are analyzed. Dst and AE indices are used to determine the strength of the storms. The time derivative of the horizontal geomagnetic field which is considered as a reliable indicator for GIC is the main parameter for the ground-level effect. In the ionospheric part, the main parameter is the F-layer critical electron density difference between the active and quiet day periods. In the ionosphere, geomagnetic storms can have both negative and positive effects on the electron density which means the electron density might increase or decrease during the storm. Thus, while selecting the storms for case studies, this has been considered and both of these examples are shown. In order to be able to see the relationship with the solar plasma, satellite data is used, and the parameters selected are ion density, speed, total and southward interplanetary magnetic field (IMF Bt and Bz), and dynamic pressure. All of these parameters are compared with time series. The only case with electric field measurement is 27 February 2014, and for this case, also the northward and eastward electric field components are analyzed.

The statistical part of the study consists of histogram analysis and linear relationships between physically meaningful pairs. It is aimed to understand the general behavior of the geomagnetic field and the ionosphere during geomagnetic storms with histograms. The averages and the possibilities are found for certain thresholds. Linear relationships between the 72 pairs have been determined by using scatter plots and calculating Pearson correlation coefficients. The reliability of the Pearson correlation coefficients is tested with Student's t-test at a 0.05 significance level. The aim of this analysis is to find out the possible dependency between the parameters, and determine what to expect based on the known variations for geomagnetic storms in various strengths.

In overall, it is aimed to estimate to what extent the geomagnetic field and ionospheric electron density are affected by solar activity at mid-latitudes, and form a milestone to understand which physical processes are effective at our latitudes. Determining what kind of variations are seen in different phases of a storm gives information about the mechanisms driving the seen effect on the ground or in the ionosphere. As similar, determining which geomagnetic index or solar wind parameter also gives information about the affecting mechanism behind the change. It is believed that this study will give insights for future studies which will be done on the space weather effects over Türkiye.

JEOMANYETİK FIRTINALAR SIRASINDA ORTA ENLEMLERDEKİ MANYETOSFER-İYONOSFER-YER ETKİLEŞİMİNİN İSTATİSTİKSEL OLARAK İNCELENMESİ

ÖZET

"Uzay havası" ifadesi, uzaydaki, daha spesifik olarak güneş sistemindeki koşulları tanımlamak için kullanılır. Güneş sisteminin birincil enerji kaynağı olduğu için uzay havası Güneş üzerinde yoğunlaşmıştır. Güneş'in son derece dinamik yapısı nedeniyle güneş patlamaları olarak bilinen ani enerji patlamaları, taç küre kütle püskürmeleri olarak bilinen plazma ve manyetik alan patlamaları, bazı durumlarda açık manyetik alan çizgileri nedeniyle güneş rüzgarının hızında artış gibi olaylar gerçekleşmektedir. Şiddetli uzay havası olayları, uzay ortamında aşırı değişiklikler yaratır. Şiddetli uzay havası olayları, jeomanyetik alanda, Dünya ve çevresinde bozulmalar üreterek, nötr koşulların olumsuz yönde değişmesine neden olur. Şiddetli uzay havasının uydu operasyonları, iyonosferik iletkenliğe dayalı iletişim ve yer altı elektrik kabloları üzerinde olumsuz etkileri vardır.

Bu çalışmada, uzay havasının orta enlemler üzerinde yer ve iyonosfer seviyelerindeki etkilerinin anlaşılması amaçlanmaktadır. Literatürde bu etkilerle ilgili pek çok araştırma bulunmasına rağmen bu çalışmayı literatürdeki diğer çalışmalardan ayıran üç nokta vardır. İlk nokta, bu çalışmanın daha yaygın olarak yüksek ve hatta alçak enlemler üzerinde yapılan araştırmalardan farklı olarak orta enlemler için yapılmış olmasıdır. İkinci nokta ise hem yer seviyesi hem de iyonosferik seviye ölçümlerinin Türkiye'de yapılıyor, yani Türkiye'ye özel yapılmış bir çalışma olmasıdır. Üçüncü nokta, literatürdeki çalışmalardan farklı olarak, aynı jeomanyetik fırtınalar için hem yer hem de iyonosfer üzerindeki etkilerin birlikte çalışılmasıdır.

Dünya, Dünya'yı Güneş'ten gelen güneş enerjili parçacıklardan koruyan güçlü bir manyetik alana sahiptir. Nedeni tam olarak anlaşılamasa da ana teori, Dünya'nın iletken sıvı dış çekirdeğinin, Dünya'nın kendi ekseni etrafında dönüşü sırasında dinamo etkisiyle bir manyetik alan oluşturduğudur. Dünya'nın jeomanyetik alan çizgileri sonsuzluğa ulaşmaz çünkü Güneş de güçlü bir manyetik alana sahiptir. Böylece jeomanyetik alan ve gezegenler arası manyetik alanın (IMF) dinamik basıncının oluştuğu noktalarda manyetosfer adı verilen koruyucu bir tabaka oluşur. Manyetosfer, Güneş'ten gelen materyallerin Dünya atmosferine girmesini engeller, ancak şiddetli uzay havası olayları sonucu Güneş plazması çok hızlı ve yoğun geldiğinde, manyetosfer bozuntuya uğrar. Bu durumda da yüksek enerjili parçacıklar ve Güneş plazması atmosfere etki eder.

Bu çalışmanın yer seviyesi kısmı, jeomanyetik olarak indüklenen akım (GIC) olarak bilinen bir olaya odaklanmaktadır. Jeomanyetik olarak indüklenen akımlar, uzay havasının yer seviyesindeki en belirgin etkisidir. Dünyanın jeomanyetik alanındaki ani değişimlerin bir elektrik alanı oluşturması ve yer altında iletken bir sistemin varlığında elektrik yüklü olması esasına dayanır. Jeomanyetik alandaki hızlı değişimler, yerin kendisine nüfuz eden bir elektrik alanı yaratır. Elektrik şebekesi sistemleri ve yer altı

boruları, yer seviyesinde akan elektrik akımından etkilenir. Yüksek enlemler, manyetik kutuplar nedeniyle en şiddetli sonuçları yaşadıkları için GIC için en riskli bölgeler olmasına rağmen, GIC her enlemde meydana gelebilir ve bu çalışmanın amacı, orta enlemlerdeki GIC'lere bakmaktır.

İyonizasyon işlemi, Güneş'ten gelen aşırı ultraviyole (EUV) radyasyon ve plazmaya dayanmaktadır. Radyasyon, elektronu atmosferdeki nötr gaz atomlarından ayırır ve yüklü iyonlar ve serbest elektronlar oluşur. Böylece atmosferde elektrik yüklü bir bölge oluşur. Atmosferin iletken tabakası olan iyonosfer, atmosferdeki radyo dalgalarının iletimi, dünya çapında ve uzaydaki uydularla uzun mesafeli iletişim için çok önemlidir. Özellikle uydu teknolojisindeki gelişmelerle birlikte, iyonosferdeki elektron yoğunluğundaki değişimlerin anlaşılması, askeri ve seyir sistemlerinden günlük hayatımızın son derece önemli parçalarından biri olan cep telefonlarına kadar bu teknolojilerin birçok uygulamasında kritik önem kazanmaktadır. Bu nedenle, bu çalışmada jeomanyetik fırtınaların olduğu günlerdeki iyonosferik elektron yoğunluğundaki değişimlerin anlaşılması amaçlanmaktadır.

Bu çalışmada Marmara Bölgesi'nde ölçülen üç veri seti kullanılmıştır (GG: ~ 40°K, GM: ~38°K). Birinci veri seti, İznik'te (40°K, 29°D) bulunan Kandilli Jeomanyetik Rasathanesi'nden elde edilen jeomanyetik alan ölçümleridir. Burası Türkiye'deki tek jeomanyetik gözlemevidir ve INTERMAGNET üyesidir. 1 dakikalık çözünürlüklü verileri INTERMAGNET'te mevcuttur. Bu çalışma için gözlemevinden 1 saniyelik çözünürlüklü veriler talep edilmiştir. 2013-2015 yılları arasında 36 tane jeomanyetik fırtınanın olduğu gün seçilmiş ve bu veriler kullanılmıştır. İkinci veri seti ise Bozcaada'da (39°K, 26°D) bulunan LEMI-414 manyetotellürik istasyonundan elde edilen jeomanyetik ve jeoelektrik alan ölçümleridir. Manyetotelürik istasyon 2013 ve 2014 yılları arasında faaliyette kalmıştır. Dolayısıyla, daha önce bahsedilen 36 günün 10'u analiz için mevcuttur. Hem jeomanyetik hem de jeoelektrik alan ölçümleri 1 saniyelik çözünürlüktedir. Son veri seti, İstanbul İTÜ Kampüsü'nde (41°K, 28°D) bulunan Dynasonde'den elde edilen F-tabakası elektron yoğunluğu ölçümleridir. Aynı 36 fırtına için, tümü 4 dakikalık çözünürlükte olan veriler kullanılmıştır. Ek olarak, Bozulma Fırtına Zamanı (Dst) indeksi, Aurora Elektrojet (AE) indeksi, ACE ve WIND uzay araçlarından elde edilen güneş rüzgârı verileri kullanılmıştır.

Bu tez çalışması, vaka çalışmaları ve istatistiksel çalışma olmak üzere iki ana bölümden oluşmaktadır. Vaka çalışmaları için, 2013 St. Patrick fırtınası olarak da bilinen 17 Mart 2013, 27 Şubat 2014 ve 9 Eylül 2015 olmak üzere birbirini takip eden yıllardan Dst değerleri baz alınarak 3 jeomanyetik fırtına seçilmiştir. Vaka çalışmaları, zaman serileri aracılığıyla kapsamlı bir şekilde yapılmıştır. Jeomanyetik fırtınaların evreleri başlangıç, ana ve toparlanma evreleri olarak belirlenmiştir. Farklı parametrelerdeki değişimler analiz edilmiştir. Fırtınaların şiddetini belirlemek için Dst ve AE indeksleri kullanılmıştır. GIC için güvenilir bir gösterge olarak kabul edilen yatay jeomanyetik alanın zamanla türevi, yer seviyesindeki ana parametre olarak seçilmiştir. İyonosferik kısımda ana parametre, aktif ve sakin gün periyotları arasındaki F-katmanındaki kritik elektron yoğunluğu farkıdır. İyonosferde, jeomanyetik fırtınaların elektron yoğunluğu üzerinde hem negatif hem de pozitif etkileri olabilir, bu da fırtına sırasında elektron yoğunluğunun artabileceği veya azalabileceği anlamına gelir. Bu nedenle, vaka çalışmaları için fırtınalar seçilirken bu dikkate alınmış ve bu iki örnek de gösterilmiştir. Güneş plazması ile ilişkiyi görebilmek için uydu verileri kullanılmıştır ve seçilen parametreler iyon yoğunluğu, hız, toplam gezegenler arası manyetik alan (IMF Bt) ve bunun güney bileşeni (IMF Bz) ve dinamik basınçtır. Tüm bu parametreler zaman serileri ile karşılaştırılmıştır.

Elektrik alan ölçümü olan tek fırtına 27 Şubat 2014'tür ve bu durum için elektrik alanın kuzey ve batı bileşenleri de analiz edilmiştir.

Çalışmanın istatistiksel kısmı, histogram analizi ve fiziksel olarak anlamlı çiftler arasındaki doğrusal ilişkiden oluşmaktadır. 27 farklı parametre için histogramlar, 72 parametre çifti için dağılım grafikleri ve korelasyon katsayıları kullanılmıştır. Histogramlar ile jeomanyetik alanın ve iyonosferin jeomanyetik fırtınalar sırasındaki genel davranışının anlaşılması amaçlanmıştır. Belirli eşikler için ortalamalar ve olasılıklar bulunmuştur. 72 çift arasındaki doğrusal ilişki, saçılma grafikleri kullanılarak ve Pearson korelasyon katsayıları hesaplanarak belirlenmiştir. Pearson korelasyon katsayılarının güvenilirliği Öğrenci t-testi ile 0.05 anlamlılık düzeyinde test edilmiştir. Bu analizin amacı, parametreler arasındaki olası bağımlılığı bulmak ve çeşitli şiddetlerdeki jeomanyetik fırtınalar için bilinen varyasyonlara dayanarak ne bekleyeceğinizi belirlemektir.

Bu tezde, bu çalışmanın ön sonuçları açıklanmaktadır. Bu kapsamlı çalışmada olası ilişkileri görmek için bazı yöntemler bir arada kullanılmış ve farklı yöntemler kullanılmıştır. Bu çalışmadan jeomanyetik fırtınalar sırasında ülkemizin bulunduğu enlemlerde yer seviyesinde ve iyonosferik seviyede nasıl değişimler olduğu ile ilgili çeşitli sonuçlara ulaşılmıştır. Yer seviyesinde jeomanyetik alanın yatay bileşeninde zamana bağlı değişimlerin büyüklükleri, bu değişimlerin fırtınanın hangi aşamalarında gözlemlendiği ve buna bağlı olarak hangi doğal fiziksel mekanizmaların bizim enlemlerimizde etkin olduğu, fırtınaların ve aşamalarının hangi jeomanyetik indis ile daha ilişkili olduğu, hangi aşamada nasıl büyüklüklerde değişimler beklenmesi gerektiği gibi sorular tartışılmıştır. Gelecekteki çalışmalar için, daha yüksek vaka sayısına sahip fiziksel olarak anlamlı parametre çiftleri arasındaki ilişkileri bulmak için farklı istatistiksel yöntemlerin kullanılması amaçlanmaktadır. Daha iyi anlaşılması için dağılım eğrileri bulunacaktır. Nedenler ve etkiler arasında daha iyi bağlantılar kurmak için örnek olay incelemelerine üst üste bindirilmiş zaman serisi analizi uygulanacaktır.

Bu çalışmanın, orta enlemlerde jeomanyetik alan ve iyonosferik elektron yoğunluğunun güneş aktivitesinden ne ölçüde etkilendiğini tahmin etmek ve enlemlerimizde hangi fiziksel süreçlerin etkili olduğunu anlamak için bir kilometre taşı oluşturması amaçlanmaktadır. Bir fırtınanın farklı evrelerinde ne tür değişimlerin görüldüğünü belirlemek, yerde veya iyonosferde görülen etkiye sebep olan mekanizmalar hakkında bilgi verir. Benzer şekilde, hangi jeomanyetik indeksin veya güneş rüzgârı parametresinin yer ve İyonosferde daha çok etkili olduğunun belirlenmesi de değişimin ardındaki etki mekanizması hakkında bilgi verir. Bu çalışmanın gelecekte Türkiye üzerinde uzay havasının etkileri konusunda yapılacak çalışmalara ışık tutacağı düşünülmektedir.

1. INTRODUCTION

Technology dependence is a part of life in the 21st century. The security of technical systems must be maintained by extensive research in order to preserve the existing standard of living. Even though hazards have always been studied, awareness of potential dangers increases as more information about nature itself is learned. One of the relatively recent areas of science that is utilized to describe the current conditions in space, namely in the Solar System, is Space Weather. The primary areas of interest for space weather are the severe solar surface activity and how they affect Earth. Extreme space weather may have a wide range of effects on many things, such as communications, power supply systems, GPS systems, satellite communications, and weather. Extreme space weather events can result in geomagnetically induced current (GIC) which is a phenomenon that affects underground pipelines and power grids. With the use of precautions, the impacts of the GIC are controllable; nevertheless, understanding the space weather as its cause and how it relates to the GIC is necessary before making any preparations for safety precautions. The conducting layer of the atmosphere called the ionosphere is also affected by space weather. These effects can be harmful such as radio wave disturbance, signal scintillation, and disturbed reception. Thus, the effects on the ionosphere also should be understood well in order to take precautions.

1.1 Sun and Space Weather

1.1.1 Sun

Life on Earth depends on the Sun, the heart of our Solar System. It is mainly a plasma ball with a highly complex dynamic structure. The regions of the Sun can be characterized in two sections, its interior and its atmosphere.

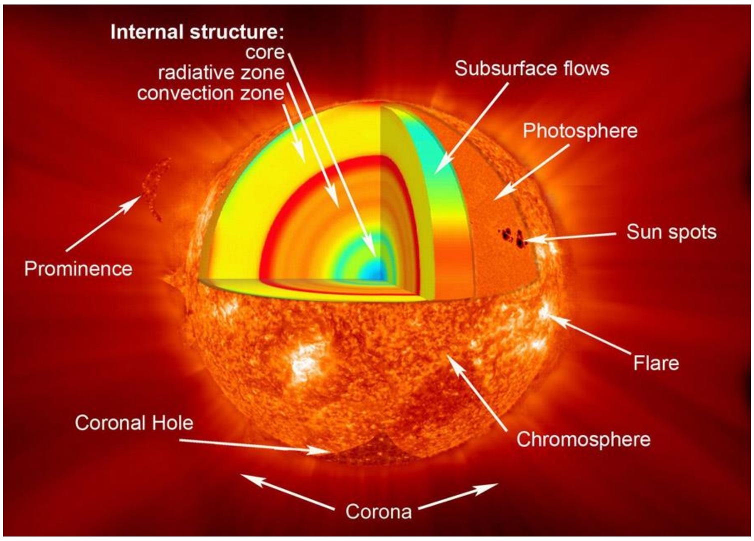

Figure 1.1 : Structure of the Sun (UCAR, 2012).

The interior of the Sun has three regions. The most inner part is called its core. The energy of the star is created in the core by nuclear fusion. The upper region is the radiation zone. The radiation zone is responsible for the transportation of energy via radiative diffusion and thermal conduction. The outer part of the inner structure is the convection zone. In the convection zone energy is transported via convection.

The atmosphere of the Sun also has three regions. The inner part is called the photosphere where electromagnetic radiation starts to escape from the Sun. It is the visible region of the Sun; thus, it can be observed with naked eye. It is the region where granules are located. The region in the middle is called the chromosphere. This region is seen as red in the case of a solar eclipse. It is the region where filaments and prominences rise to the corona which is the outer atmosphere of the Sun. It extends millions of kilometers into the solar system. It can only be observed during an eclipse or with coronagraphs. This is the region where coronal loops and holes, coronal mass ejections (CMEs), and flares form.

Due to its complex dynamic structure, the Sun has its cycles. Among these cycles, due to the historic data we have, the most important one is the 11-year cycle. As the Sun rotates, due to the angular speed difference and fluid-like state, the polarity of the Sun's magnetic field changes. Thus, creates a cycle where there are the solar minimum and maximum phases. The currents solar cycle we are in is solar cycle 25 which started approximately at the beginning of 2020, and the next solar maximum is expected to be around 2025.

1.1.2 Space weather

The conditions of the near-Earth environment and changes happening due to Solar wind and plasma are called space weather. It is mainly concerned with the varying changes in the magnetosphere, ionosphere, and thermosphere due to changes in the Solar wind conditions. The effects of the space weather can be harmful in many areas extending from the ground level to the satellites. The main source of all the changes is the Sun. Thus, it is important to understand and investigate the dynamics of the Sun.

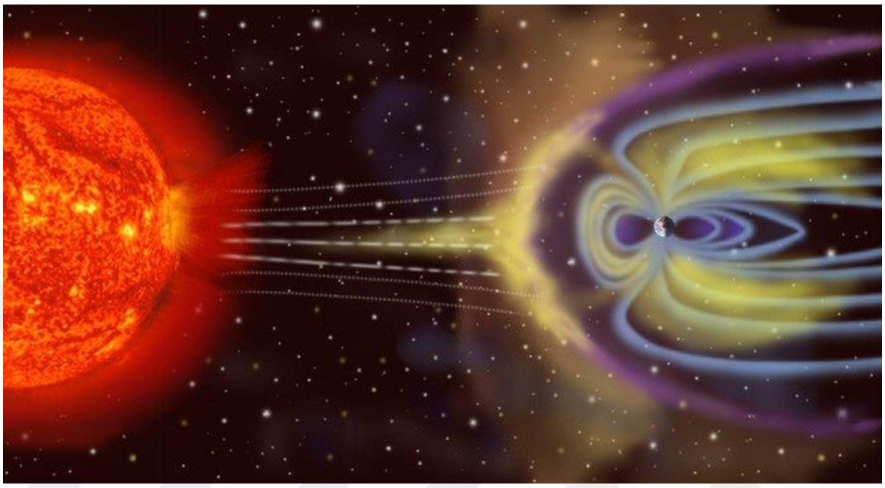

Figure 1.2 : Illustration of Solar Wind-Magnetosphere interaction (NASA, 2015).

1.1.3 Sources of space weather

The structure of the Sun is highly complex mainly due to its magnetic field lines. The energy of the Sun is created in its core and it is transferred to its surface via different mechanisms. The magnetic free energy the Sun has converted to electromagnetic radiation, kinetic and thermal energy. During the release of its energy, different mechanisms occur, and they result in affecting the near-Earth environment. These mechanisms are called space weather drivers and the main ones can be listed as coronal mass ejections (CMEs), high speed streams (HSS), and solar flares.

1.1.3.1 Coronal mass ejection

CMEs occur at the Solar corona by reconnection of the magnetic field lines. The magnetic field lines leave and return to the surface at the Solar corona, and they form loops. When the two opposite magnetic field lines come together, reconnections occur and the loop leaves the surface. The plasma leaves the Sun with hundreds of km/s velocity with its magnetic field and travels away from the Sun radially. The velocity of the CME varies between 200 and 3000 km/s. These ejections are monitored via coronagraph imageries located at the L1 point. It can be estimated whether the CME is directed toward Earth or not. Most of the significant geomagnetic storms are caused by CMEs (Richardson & Cane, 2012). The arrival of tons of Solar plasma and its encounter with the magnetosphere creates sudden changes in geomagnetic parameters since the effect is transferred everywhere via magnetic field lines.

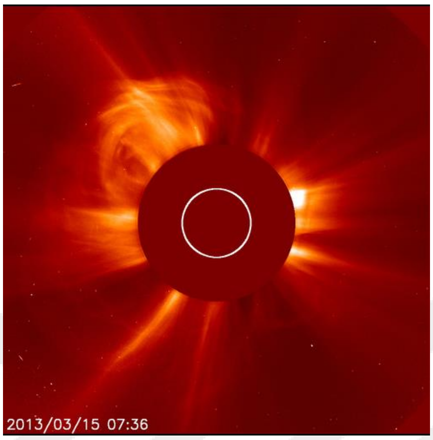

Figure 1.3 : Coronograph imagery via SOHO LASCO C2 on 15 march 2013 (NASA, n.d.-b).

1.1.3.2 High speed stream

The solar wind continuously breezes from the Sun radially. The average speed of the ambient solar wind is approximately 400 km/s. When the solar wind speed exceeds 400 km/s, it is referred to as high speed stream (HSS). HSS is caused mainly by structures called coronal holes (CHs). Coronal holes are the areas on the Sun's surface where the magnetic field lines are open. They seem darker in the images since it is cooler than their surroundings. Coronal holes are can be detected from the imagery of the Sun in different wavelengths. The solar wind breezes faster from these regions, and they are called Coronal Hole High Speed Streams (CH HSS). HSS can also be caused due to a CME. The severity and the frequency of the CME-sourced HSS are greater than CH HSS, still, they are significant in the terms of causing minor to strong geomagnetic storms (Gerontidou et al., 2018).

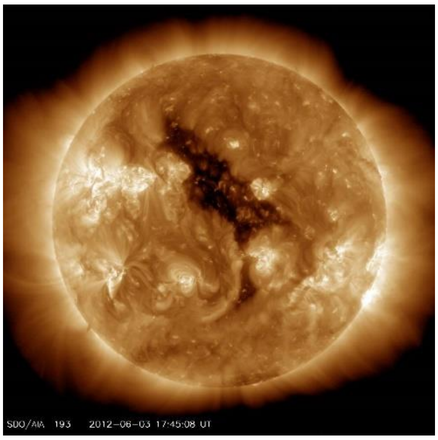

Figure 1.4 : SDO 193 image (NASA, 2012).

1.1.3.3 Solar flares

Solar flares are sudden bursts of energy from the active regions of the photosphere. The released energy consists of energetic high-speed ions. They are not predictable and cannot be prepared beforehand since it reaches Earth in minutes. The only part which can be estimated is that they occur in active regions and they can be monitored via imageries. Like the CMEs, they also form with magnetic reconnection. The effects of the flares are seen in radio communication and propagation. They mainly affect the ionosphere in the near-Earth environment. During the solar maximum, more frequent and severe solar flares are expected due to the higher amounts of Sunspots and active regions.

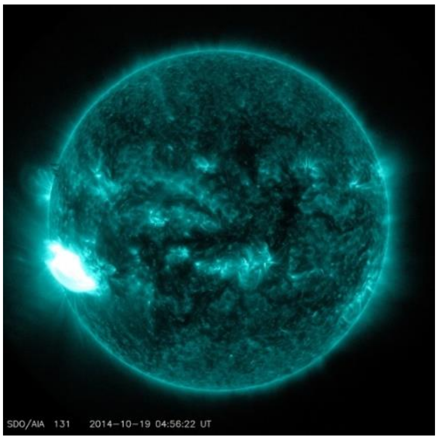

Figure 1.5 : SDO 131 image (NASA, 2014).

1.1.4 Effects of space weather

There are different kinds of technological systems which might be affected by various space weather drivers, even though they all disturb the near-Earth environment. For example, the ground-level effects require strong disturbances; thus, most CMEs are responsible for geomagnetically induced currents (GICs), or radio blackout storms are a consequence of solar flares. Some of the affected areas by space weather are ground level (GICs), ionosphere, and satellites.

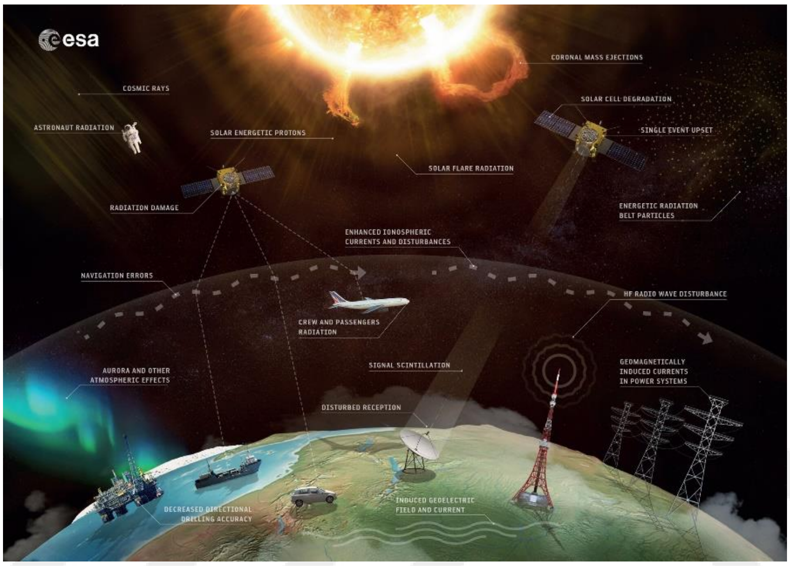

Figure 1.6 : Space weather effects (ESA, 2018).

Satellites are affected by the charged solar particles directly since some of them are not under the protection of the magnetosphere. How much and in what way they are affected varies greatly based on their location such as whether they are in the inner or outer radiation belt. Deep spacecraft charging is one of the most common and dangerous effects of space weather over spacecrafts. It may cause structural damage which might harm the critical systems, and cause spacecraft to give false commands, or give damage to the storage data and the software itself. Drag effect is also a harmful consequence, especially for low-orbiting satellites. The density in the upper atmosphere changes during geomagnetic storms since the radiation and energy amounts change. Thus, the altitude of the satellite may change, and the satellite might go out of orbit and might even get lost if it cannot be detected by ground detectors.

Radio communication is highly vulnerable to space weather since it depends on the ionosphere which can easily vary due to changes in solar conditions. In radio communication high frequency radio waves are important, and it depends on the ionospheric structure and density so the transmission path of a wave can be determined. HF radio waves are used in many areas such as by commercial airlines, and amateur radio operators. The ionosphere can be affected by space weather in several ways. One of them is solar flares. The x-rays coming from the Sun cause ionization at the bottom (D) layer of the ionosphere, and this results in a way that the layer becomes either a reflector or an absorber for different wavelengths and since the solar flares cannot be predicted before, the necessary precautions cannot be taken. Another way is energetic particle precipitation. The energetic particles coming from the Sun enters the Earth's ionosphere through the magnetic poles with magnetic field lines, and cause ionization, especially at the D layer. This situation is mostly seen in high latitudinal regions.

Geomagnetically induced currents (GICs) are the most eminent effect of space weather at ground level. It is based on the principle that the sudden changes in the Earth's geomagnetic field create an electric field, and in the presence of a conducting system underground, they are electrically charged. This might result in blackouts in cities due to problems occurring in power lines and transformers.

1.2 Ionosphere

The layers of Earth's atmosphere are usually classified as temperature gradients. Yet, when the ionization ratio is considered, there is a layer that is important, especially in communication. This layer is called the ionosphere and it is a conducting layer that extends from approximately 60 km to 800 km or higher. Even though the main source of ionization in the atmosphere is the Sun, cosmic rays also have a role, especially during solar minimum. Additionally, in diurnal variations, the effect of the Sun is dominant during the day, and galactic cosmic rays are more efficient during the night.

The ionization process is based on the extreme ultraviolet (EUV) radiation and plasma coming from the Sun. The radiation strips the electron from the neutral gas atoms in the atmosphere, and charged ions and free electrons form. This process is called photoionization. Thus, an electrically charged region forms in the atmosphere.

The structure of the ionosphere varies diurnally, seasonally, annually, and latitudinally. The atmospheric density and the absorption of solar energy are different at every altitude; thus, the atmospheric chemistry and ionization levels vary greatly.

Magnetospheric ring currents, as well as the electrojet currents also affect the ionization levels. These are the reasons the ionosphere behaves differently in low, mid, and high latitudes, as well as at different heights.

1.2.1 Vertical structure

The atmospheric density is different at every altitude. Thus, the ionization levels change with height as well. The ionosphere consists of 3 or 4 layers based on the idealized vertical structure of the ionosphere. The structure of the ionosphere changes at night due to the lack of solar radiation. During the day, the layers of the ionosphere are D, E, F1, and F2. Yet at night, F1 and F2 layers combine into one F layer.

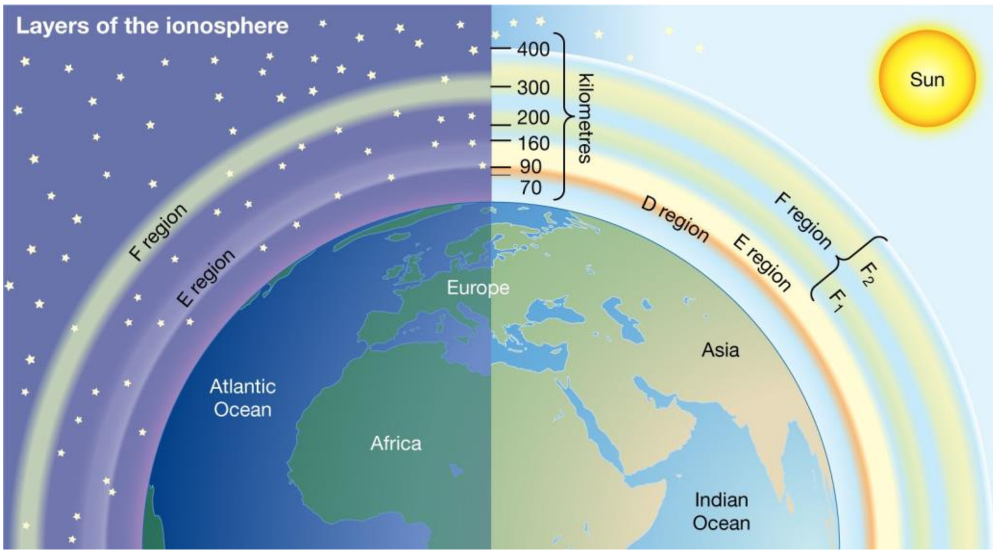

Figure 1.7 : Structure of Ionosphere (McElroy, n.d.).

The lowest layer is the D layer which roughly extends between 60 and 90 km. X-ray photons are cosmic ray particles that are highly energetic and are most dominant at the D layer. The recombination rates which means returning to the neutral form of an atom by recombination of ions and electrons are high at this level. Thus, this layer is not considered plasma since the atmosphere is weakly ionized. The dominant ions in this layer are NO^+ and O_2^+. D layer is crucial in radio communication. The ionization rates get much lower at night due to the lack of solar radiation; thus, the D layer barely exists at night due to the galactic cosmic rays.

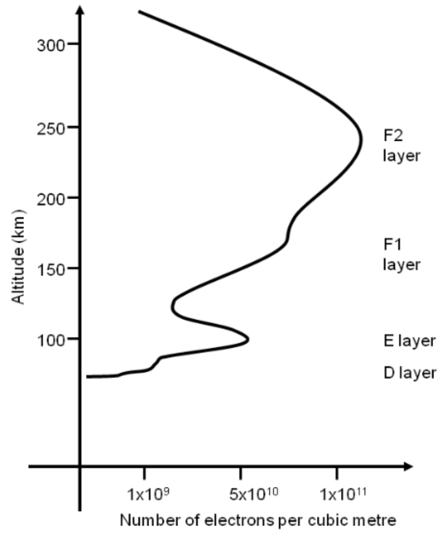

Figure 1.8 : Vertical structure of ionosphere (Scott, 2022).

E layer extends between 90 and 150 km. The height of peak electron density is roughly around 110 km. It exists both day and night time. In this layer, the main source of ionization is short-wavelength ultraviolet radiation, and medium-frequency radio waves are reflected. In high latitudes, electron and proton precipitating has a significant role in ionization. There is also a layer that only occurs in special situations which is called the sporadic E layer. Sporadic E layer forms around similar altitudes as the E layer, and might even have greater electron density. The high amounts of electrons cause the refraction of high-frequency waves.

The outer layer of the ionosphere is the F layer during the night. It extends between 150 km to 500 km. The main ionization source at this layer is extreme ultraviolet radiation from the Sun, and the main atom that gets ionized is oxygen. During the day, the F layer is separated into two layers as F1 and F2 layers. High-frequency radio signaling to long distances is usually made through the F layer since it is the layer that has the greatest electron density. The F2 layer is the most important layer here for radio communication since it is present for the whole day.

1.3 Geomagnetic Field

Earth has its own protective shield against the solar wind and galactic cosmic rays which is believed caused by its conductive outer liquid core. This core of the Earth acts as a dynamo and creates a magnetic field around the Earth which is called the geomagnetic field. The geomagnetic field is mainly a magnet and the magnetic field lines go from the south magnetic pole to the north.

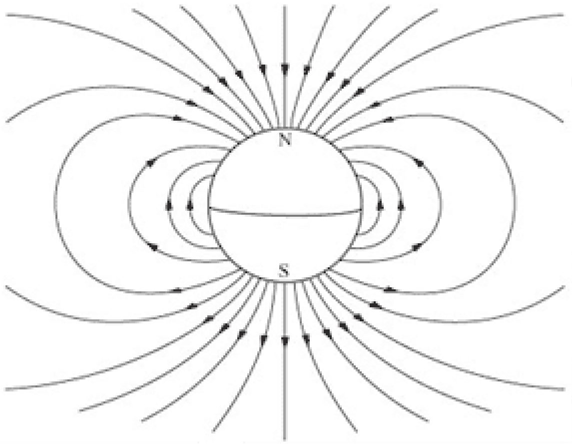

Figure 1.9 : Earth's geomagnetic field (United States Geological Survey, n.d.).

The geomagnetic field is a vector which means it has a direction and strength at each point.

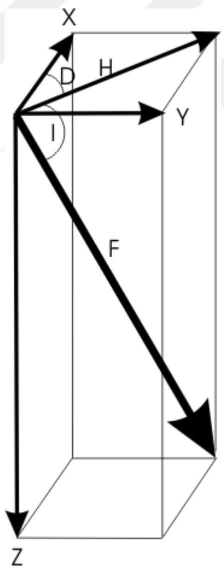

Figure 1.10 : Geomagnetic field components (Natural Resources Canada, 2020).

As shown in the Figure 1.10, the geomagnetic field can be defined as vectors and angles. The northward component is X, the eastward component is Y, and the vertical component is Z. F represents the total strength of the geomagnetic field and it's the vectorial sum of all the components. H is the horizontal component which means the vectorial sum of northward and eastward components. D is called the magnetic declination angle and it is the angle between X and H. I is the magnetic inclination angle, and it is the angle between H and F.

1.3.1 Geomagnetically induced currents

Faraday's induction law suggests that the rapid changes in a magnetic field create an electric field. In the equation (1.1) below, E represents the electric field, B represents the magnetic field, and t is the time. In nature itself, magnetic fields and electrical currents that change in time exists without any artificial forcing. In the ionosphere, oceans, and Earth itself, there are natural electrical currents. During intense geomagnetic storms, rapid changes occur in the geomagnetic field. This change causes an electric field to form and if there are conducting systems beneath the ground such as transmission lines, railroads, or pipelines, these conducting systems get electrically charged. This electric current is called geomagnetically induced current (GIC). As a result, that the reactive power might increase, voltage problems and excessive heating might occur, and transformers might get harmed in a way not to perform any longer (Oyedokun & Cilliers, 2018).

$$\nabla \times \vec{E} = -\frac{\delta \vec{B}}{\delta t} \tag{1.1}$$

In 21st century, technological developments are at a level that almost everything depends on electrical power systems which are vulnerable to the electrical currents occurred due to geomagnetic storms. The impact of geomagnetic storms on electrical power systems is hard to estimate since there are various parameters to consider. The occurring electrical current flow follows a path to correspond to both naturally existing conducting structures and the artificial structures made by humans. The flow on the artificial paths turns to quasi DC which means that the current flows in one direction, occurs. This extra current in the path causes saturation in the core of the transformers since the current exceeds the planned range of the transformer. Once the transformer is saturated, the voltages and the currents get larger in extreme values. Thus, the transformers might get heated and some parts of it might get damaged. The most famous GIC event in history is the 1989 Hydro-Quebec blackout which lasted for 12 hours (Odenwald, 2017). As technology develops, the socioeconomic impacts of blackouts increase such as in the October 2003 event which caused one and a half hours of blackout in southern Sweden and cost approximately half a million USD loss (Pulkkinen et al., 2005).

1.4 Literature Review

In this section comprehensive literature research on GIC and ionospheric storms will be explained.

1.4.1 Geomagnetically induced currents

Transmission lines, telecommunications cables, pipelines, and most significantly, electric power grids are all affected by GICs. The occurrence of GICs, their mechanism, their connection to space weather, and their consequences on technological systems have all been the subject of several research. In their 2017 publication, Kalafatoğlu and Kaymaz describe how they used magnetic field and electric field measurements over Bozcaada, Türkiye, to investigate the GIC. With four case studies between 2013 and 2014, this study conducted across the mid-latitudes demonstrated the GIC's occurrence as a result of increased solar activity (Kalafatoğlu Eyigüler & Kaymaz, 2017). Another research demonstrates the link between the electric and magnetic fields when the geomagnetic disturbance above Bozcaada is noticeably low (Kalafatoglu et al., 2015).

Viljanen et al. explored the general fluctuations in the horizontal component, such as solar cycle dependence, seasonal and daily variations, as well as the link between the time derivative of the horizontal component of the geomagnetic field and the ionospheric currents (Viljanen et al., 2001a). According to certain findings, there is a significant probability of GIC occurrence at the solar minimum, in the spring and fall, and at night over high latitudes. By examining changes in the time derivative of the horizontal magnetic field between 1982 and 2001, they were able to study GICs and demonstrate that powerful GICs were linked to deviations more than 1 nT/s in the time derivative of the horizontal magnetic field (Viljanen et al., 2001a). In a follow-up to their earlier research, (Viljanen et al., 2006) used the time derivative of the horizontal magnetic field to examine GICs more than 1 nT/s for solitary (in their terminology) substorms, defined as Dst > -40 nT, and storm-time, defined as Dst -40 nT, substorm occurrences. They looked at GIC occurrences as a function of the substorm phase and concerning the ionospheric equivalent current systems. Their research demonstrated that as latitudes fell toward the south in the north, the greatest variance of the horizontal magnetic field's time derivative decreased. They also found that, for isolated occurrences, the time of the maximum in the horizontal magnetic field's time derivative peaked at lower latitudes and happened 5 minutes after the event began.

The analysis by Pulkkinen, Lindahl, Viljanen, and Pirjola is based on the Halloween storm of 2003, which resulted in a one-hour blackout across a large area and an estimated loss of 0.5 million US dollars in Sweden. The research demonstrates that the GIC was caused by a combination of substorms, sudden commencement, and enhanced ionospheric convection. The historic Hydro-Quebec blackout in 1989 was followed by the Halloween storm, which was the largest GIC event ever to be recorded (Pulkkinen et al., 2005).

According to Kappenman's case study in the paper he published, GIC is a hazard not just at high latitudes but may also be seen at low latitudes. The geomagnetic disturbances at low latitudes are reportedly caused by sudden commencements with small amplitude changes, despite the fact that electrojet-driven large amplitude changes in the geomagnetic field at high latitudes are well documented. Additionally, it has been proposed that measurements of space weather might reveal the rapid beginnings. Consequently, the GICs may be found at all latitudes. GIC magnitudes were discovered to range from a few tens of Amperes (A) to many hundreds of Amperes depending on latitude and magnetospheric activity level. In high latitude areas of the US, recorded GICs on the order of 200 A (Kappenman, 2003).

All of the most recent GIC researches that have been published in various publications are included in the 24 March 2016 edition of Space Weather. The source, latitude fluctuations, storm-substorm relationships, modeling, dangers on ground systems, and measurement systems are all covered in this special collection of GIC research. GICs and their effects at various latitudes have been extensively investigated and are well understood.

Different methods for calculating geoelectric fields were employed in the GIC research. The geoelectric fields on the ground were collected from the electrical power grids for the majority of GIC research. Nevertheless, it might be difficult to determine the grid characteristics in many places of the world. The changes in the electric field are linked to the geomagnetic fluctuations that may be observed on the ground.

Therefore, using Faraday's induction rule offers a different strategy for evaluating GICs at a certain place. According to Faraday's Law, changes in the geomagnetic field over time lead to changes in the geoelectric field. The fluctuations in these two parameters, namely the temporal rate of change of the magnetic and/or electric fields, may thus be directly measured on the ground and used to compute GICs. As a result, numerous studies have employed temporal derivatives of the magnetic field to deduce the GIC changes in the lack of electric field measurements (Fiori et al., 2014; Zhang et al., 2015).

1.4.2 Ionosphere

Across the past several decades, a great deal of research has been done on Earth's upper thermosphere and ionosphere over mid-latitudes in both geomagnetically quiet and disturbed conditions. Ionospheric characteristics fluctuate throughout a wide variety of timescales, from long-term shifts to those that last just a few days, hours, or minutes. The magnetospheric ring current and the out-flying impacts of the polar electrojets both contribute to the effects of geomagnetic activity on the mid-latitude ionosphere. The effects of a geomagnetic storm on the ionospheric F region electron density are different from those in the lower ionosphere due to variations in the physical mechanisms causing the changes in ionization. Lastovicka provided a summary of how geomagnetic storms affect the lower ionosphere, intermediate atmosphere, and troposphere (Lastovicka, 1996). The F layer's reaction to direct and indirect storm-induced disruptions can have positive (increase in electron density) or negative (decrease in electron density) consequences, depending on the storm's beginning time, location, and season. Additionally, the impact of storms on the electron density might vary depending on the altitude inside the F layer (Buresova et al., 2007).

In one research, the reaction and behavior of the sporadic E-layer and the ionospheric F2 during three intense individual geomagnetic storms from the winters of 2012, 2013, and 2015 were investigated and compared. The data was obtained from cutting-edge digital ionosonde in midlatitude, Hungary. The type of the ionospheric storm was determined by the local timing of its abrupt onset. In this manner, one no-positive phase (NPP) storm and two regular positive phases (RPP) ionospheric storms have been examined. At dawn or early in the morning, it is possible to see a noticeable rise in the electron density of the F-layer in all three situations. Additionally, it can be seen how the ionospheric layers disappear at night during geomagnetically disturbed times. The findings of the study imply that the fade-out effect is unrelated to the presence of sporadic E-layers (Berényi et al., 2018).

The impacts of the solar wind on Earth's environment are investigated in a study conducted by Buresova et. al. The near-Earth environment's increased solar wind energy dissipation is a major contributor to subsequent disturbances in the upper atmosphere and ionosphere. In the paper, it is discussed how solar wind-induced geomagnetic storms express themselves in the ionospheric environment. Regarding seasonal predilection, during the storm's main phase, only negative phases predominate in the summer, but both negative and positive phases are more likely to occur in the winter. Occasionally, improvements in electron density have been seen many hours before the start of a geomagnetic storm. Additionally, it has been noted that there were brief intervals throughout the storm's main phase when the electron density's divergence from the median was negligible. The effect on electron density at the F1 region heights in European upper middle latitudes has been shown to be negative, if any at all, regardless of the sign of the storm effect on F2-layer ionization. Significant summer/winter asymmetry is also present in the F1-layers reaction to magnetic disturbances. Compared to middle and lower middle latitudes, the stormy high latitude F area is more changeable and is significantly impacted by magnetospheric processes, particularly strong electric fields, which are often present during geomagnetic storms (Buresova et al., 2007).

An ionosonde located at the Istanbul Technical University (ITU) Maslak campus was used in one research to make measurements of the ionosphere above Istanbul, Türkiye. The study offers average statistics for critical F2 layer properties measured over a one-year period for diurnal, monthly, seasonal, and noon-midnight periods. The F2 layer critical frequency, its peak height, and the projected total electron content are those characteristics. According to the data, Istanbul's general average behavior is in line with the results of earlier studies of the mid-latitude ionosphere. These are the variations between the summer and winter in TEC, hmF2, and foF2, as well as the presence or absence of ionospheric anomalies. The diurnal changes of foF2 have also been divided into groups known as types. The types' presence and the diurnal, monthly, and seasonal changes we showed for all ionospheric data point to several physical causes that work throughout the year. These modifications can take the form of fluctuations in the geomagnetic and solar cycles, atmospheric composition, and thermospheric neutral winds. It has been demonstrated that there is a good relationship between the types and geomagnetic activity, which suggests one of the causative processes that should be taken into account for the diurnal fluctuations of electron density over mid-latitudes (Moral et al., 2020).

1.5 Purpose of Thesis

The effects of geomagnetic storms can be seen at ground level, ionosphere, and near-Earth environment. In this study, the effects on the ground and ionospheric levels are investigated. The purpose of the thesis is to understand the variations in the ground and ionospheric levels over Türkiye in order to raise awareness and take precautions. There are thorough researches based on the effects of space weather globally, yet most of them are done for high latitudes, especially for the ground-level effects. The phenomenon called geomagnetically induced current (GIC) is a risk for ground-based structures such as power grids and transformers which provides electricity to the cities. The ionosphere is affected by space weather via changes in the ionization levels which is important for high-frequency radio wave and satellite communication, and GPS operations. It is crucial to understand the variations seen in the geomagnetic field and ionospheric electron density to calculate risks and take precautions. This is the first thorough study done to understand the situation in both ground and ionospheric levels over Türkiye during the geomagnetic storms which include statistical analysis for 3 years at the peak of the 24^{th} solar cycle, and it will be a milestone for further investigations of space weather effects over Türkiye.

2. DATA

Throughout this project, three main data sets have been used for research purposes. These data sets belong to the three focus areas of the study. Basically, the space weather-related changes on both ionospheric F-layer and ground level are studied. Thus, the three main data sets consist of ionospheric level electron density, and ground-level geomagnetic and geoelectric field data have been used. Additionally, to support the theory of space weather relations, various geomagnetic and solar wind data have been used. Solar wind data are obtained from satellites, and geomagnetic indices are obtained from several geomagnetic observatories and online data sources.

2.1 Geomagnetic Field

The geomagnetic field data used in the study is obtained from Iznik Geomagnetic Observatory operated by Bogazici University, Kandilli Observatory and Earthquake Research Institute at Iznik, Türkiye. The geographic coordinates of the station are 40.5°N and 29.7°E. The geomagnetic coordinates are 37.7°N and 109.7°E. The elevation of the observatory is 256 meters and it is located outside the city center. Iznik Geomagnetic Observatory has been operating since 2005 and a member of the International Real-time Magnetic Observatory Network since 2007. In this observatory, geomagnetic variations are measured with the Danish Meteorological Institute (DMI) three-axis fluxgate magnetometer, and the absolute measurements are done with DI-flux theodolite. Additionally, the total geomagnetic field is measured using a proton magnetometer. The data are available in second and minute resolution and its unit is nT (Celik et al., 2013).

In this study, 1-second resolution data have been used in XYZ coordinates. The main parameter used is the time derivative of the horizontal magnetic field since it is closely related to geomagnetically induced currents (GIC) (Viljanen et al., 2001).

Figure 2.1 : Location of Iznik geomagnetic observatory (Çelik et al., 2013).

The horizontal magnetic field is the vectorial sum of the northward (B_x) and eastward (B_y) components of the total geomagnetic field (B).

$$\vec{H} = \sqrt{\vec{B}_x^{\ 2} + \vec{B}_y^{\ 2}} \tag{2.1}$$

The time derivative of horizontal magnetic field equation;

$$\frac{d\vec{H}}{dt} = \sqrt{\left(\frac{d\vec{B}_x}{dt}\right)^2 + \left(\frac{d\vec{B}_y}{dt}\right)^2} \tag{2.2}$$

2.2 Geomagnetic and Electric Field

In this study, the main geomagnetic field data are gathered from Iznik geomagnetic observatory, yet in the ground level part of the study, geoelectric field data also have been used. The magnetotelluric station used in geomagnetic and geoelectric field measurements is located at Bozcaada (seen in the figure) where the geomagnetic coordinates are 39.5°N and 26°E, and geomagnetic coordinates are 37.5°N and 106.1°E. The site where is station is located is away from the city, buildings that can produce a significant amount of electricity, busy roads, and building on a hill. The system is buried in 80 cm depth on a 100 x 100 m area. For the measurements, Long-period Magnetotelluric Station produced by ElectroMagnetic Innovation (LEMI-417) has been used. The system includes one electrometer, one fluxgate magnetometer, four electrodes, and one electric unit. There are electrical currents within the Earth itself.

Yet, there are also electrical currents that originate from outside sources such as by ionosphere and magnetosphere. The magnetotelluric currents consist of both natural and external electrical currents. LEMI-417 focuses on measuring natural magnetic and electric fields and their variations from the base. The geomagnetic field is measured in three axes as XYZ and the electric field is measured in two directions, XY as in eastward and northward directions. The measurements are in 1-second resolution. The unit of the geomagnetic field is nT, and μV/m.

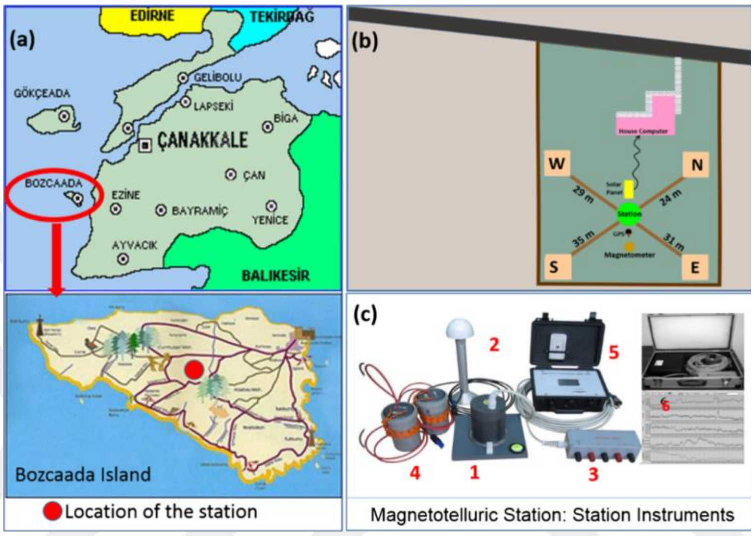

Figure 2.2 : (a) A map of the region and island Bozcaada, Çanakkale, Türkiye, where the instruments were installed. (b) Plan of the instrumental set up in the field. (c) Instruments that came with magnetotelluric station; (1) Magnetometer, (2) GPS receiver, (3) Electrodes, (5) Station, (6) An example of raw data (Kalafatoğlu Eyigüler & Kaymaz, 2017).

The main principle behind the study is Faraday's law as can be seen from the equations 2.3, 2.4, and 2.5.

$$\nabla \times \vec{E} = -\frac{dB}{dt} \tag{2.3}$$

$$\overrightarrow{E_x} \propto -\frac{\overrightarrow{dB_y}}{dt} \tag{2.4}$$

$$\overrightarrow{E_y} \propto -\frac{\overrightarrow{dB_x}}{dt} \tag{2.5}$$

As Faraday's law suggests, sudden changes in the geomagnetic field form an electric field. This is the reason for studying a geomagnetic field to estimate the changes in the electric field. Moreover, make a connection between geomagnetically induced currents and geomagnetic field fluctuations. As the law suggests, the northward component of the electric field (E_x) is closely related to the time derivative of the eastward component of the geomagnetic field (dB_y/dt), and vice versa. Thus, in this study horizontal components of geomagnetic and electric fields are focused.

The magnetotelluric station was working and collecting data between September 2013 and October 2014. All the available days in which the data is available have been considered and 10 of them were in the selected 36 days. Thus, in the statistical part of the study, 10 days with electric field measurements are included. 9 September 2015 is chosen for the thorough case studies. The Table 2.1 shows the days included in the statistical part of the study.

Table 2.1 : Case days with LEMI measurements.

Storm Day	Minimum Dst
2 October 2013	-72
9 October 2013	-69
15 October 2013	-49
30 October 2013	-56
16 November 2013	-40
8 December 2013	-66
27 February 2014	-97
12 April 2014	-87
30 April 2014	-67
12 September 2014	-88

2.3 Ionospheric Measurements

Ionosondes are special radars developed to observe the ionospheric level electron density. The basic components of an ionosonde are the transmitter, receiver, controller, and data processor. The transmitter produces high-frequency pulses ranging between 0.1 MHz to 33 MHz and sends them to the ionosphere. The reflecting signals are collected by the receiver. The delay time between the transmission time of the signal and the receiving time is calculated by the controller. Delay time is an essential part of the process since it is used to estimate the heights of the ionospheric layers for the ionograms.

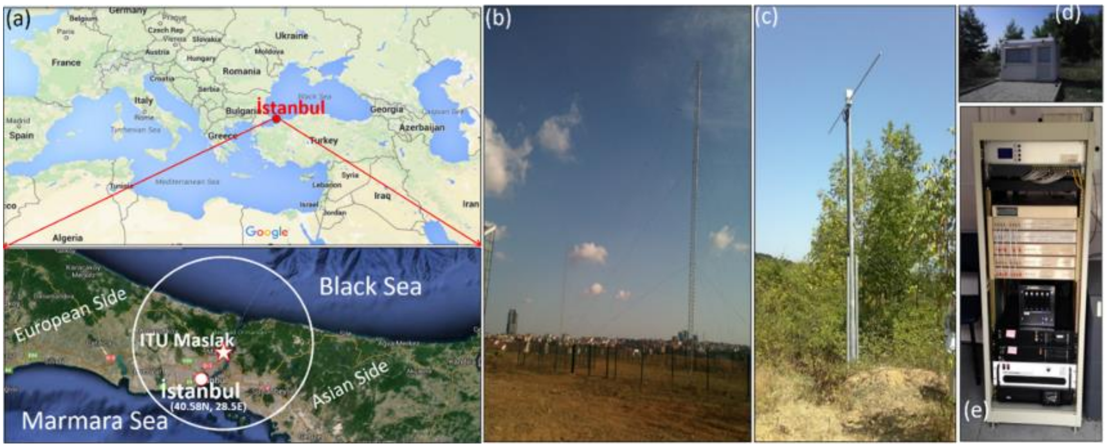

Figure 2.3 : (a) Location of the experiment site in Istanbul, Türkiye (40.58oN, 28.5oE), (b) Transmitter, (c) Receiver, (d) Shelter and (e) Radar (Moral et al., 2020).

Dynasonde or VIPIR (Vertically Incident Pulsed Radar) are names given for a specific ionosonde type. ITU Dynasonde system is built by Scion Associates, Inc. which is the VIPIR part of the system. The software is developed by the University of Colorado Boulder. In Dynasonde, the pulses are sent vertically to the ionosphere and use model assumptions at a minimum. Its ranging altitude is between 70 and 800 km. The software of the Dynasonde is called NeXtYZ and it gives 79 different parameters to the user such as total electron content (TEC), the critical frequency, and the critical height of every ionospheric layer in different modes. Its working principle consists 'pulsets' which are called for transmitted pulse groups. Pulsets usually have 4-8 pulses in a designed pattern and approximately 1 kHz frequency offsets. An echo is generated when a signal is reflected from a layer of the ionosphere. The importance of the Dynasonde technology becomes clearer at this point since there are lots of echoes in the surrounding produced by weather conditions such as rain, broadcast signals, electrostatic voice, etc. The software of the Dynasonde eliminates the false echoes based on their time of arrival. The total echo of the Dynasonde consists of these complex amplitudes caused by false echoes, and different parameters such as the time, location of the antenna, and radio frequency.

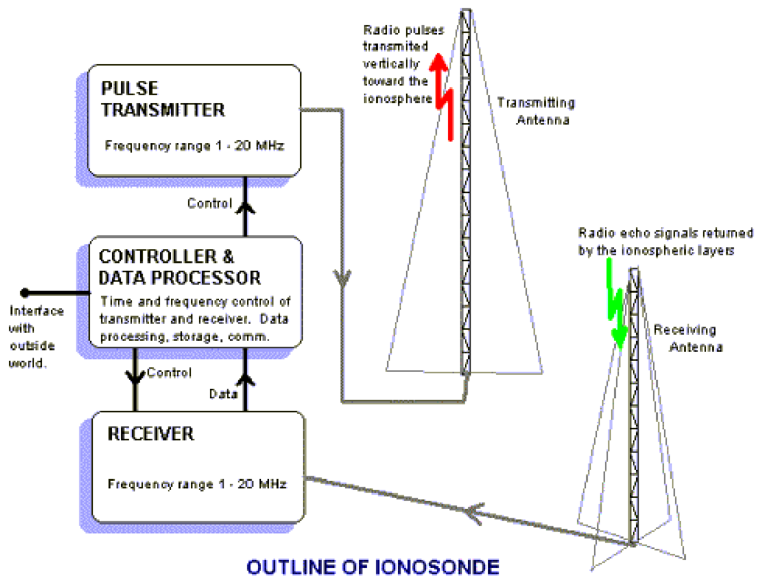

Figure 2.4 : Outline of ionosonde (Australian Space Academy, n.d.).

NeXtYZ gives an output called an ionogram also known as vertical incidence sounding. An ionogram represents the virtual heights of every ionospheric layer against frequency, yet they usually are shown in electron density rather than frequency. In the Figure 2.5 there is an example of an ionogram for 12 April 2014 at 09.00 UTC over Istanbul. All the layers of the ionosphere and the radio frequency at every height can be seen.

The ITU Dynasonde where the data are obtained is located at Istanbul Technical University Ayazaga Campus, Istanbul. The geographic coordinates are 41°N, and 29°E. The geomagnetic coordinates are 39°N and 108°E. The Dynasonde was installed in September 2012 and continued to gather data until 2018. The data resolution is 4 minutes between 2012 and 2013 November, and 2 minutes after November 2013. At the site of the Dynasonde, there is one transmitter, a transmitting antenna that is 25 meters high, 4 receivers, and 4 receiving dipole antennas which are 5 meters each. High-frequency (HF) pulses are sent vertically to the ionosphere with a ranging frequency of 0.1 to 25 MHz.

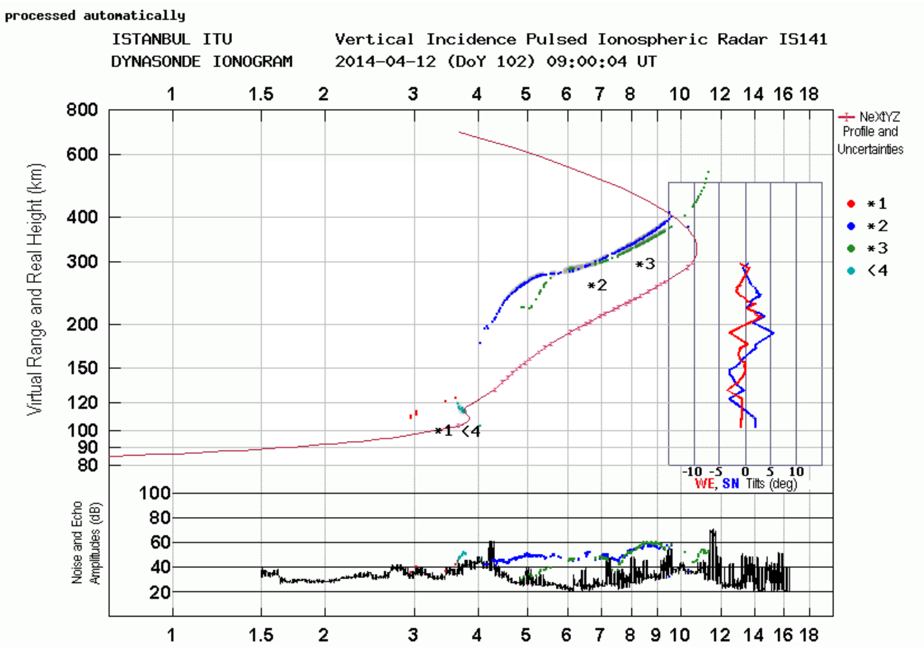

Figure 2.5 : Ionogram example from ITU Dynasonde.

For this study, the main parameter was chosen as F-layer electron density. Electron density values and trends vary daily, seasonally, and annually over mid-latitudes (Moral et al., 2020). Thus, to be able to analyze 36 days in a 3-year period, the difference between the quiet and active days for electron density has been decided as the main parameter instead of the active day's value solely. The reference quiet days have been chosen from the same month and year to avoid any seasonal and annual variations. NeXtYZ software does not give the maximum electron density directly. Instead, it gives the F-layer critical frequency which can be used to obtain maximum electron density.

$$f_{critical} = \frac{0.0091}{\cos\alpha}\sqrt{n_{e_{max}}} \tag{2.6}$$

Here in the equation, $f_{critical}$ is given by NeXtYZ as fof2, ne_{max} is the maximum electron density, and α is the incidence angle which is taken as 0 since the pulses are sent vertically with Dynasonde. Thus, $cos\alpha$ is 1. The equation for maximum electron density is like the following equation 2.7. The unit for electron density is used as #/cc.

$$n_{e_{max}} = \left(\frac{f_{critical}}{0.0091}\right)^2 \tag{2.7}$$

2.4 Geomagnetic Indices

In order to obtain the disturbances in the magnetosphere and determine whether there is a geomagnetic storm or a magnetospheric substorm that occurred or not, some indices are used. These are mainly products of measurements from ground magnetometers. The most common indices and the ones used in this study are Disturbance Storm Time (Dst), Auroral Electrojet (AE), and Kp (Planetary K) indices.

2.4.1 Dst

Dst is one of the main indices used to determine geomagnetic disturbances. Dst is calculated from the horizontal magnetic field. The measurements used for this index are done from 4 low latitude stations. The Dst index are available since 1957. It has a 1-hour resolution and its unit is nT. Even though, it mainly indicates the changes in the equatorial ring currents, magnetopause Chapman-Ferraro, and tail currents are included in it. When the solar wind first interacts with the magnetosphere, it causes a compression. This compression is measured in the stations through the magnetic field lines. In some cases, this compression effect can be seen via positive Dst values at the beginning of the storm which is called Sudden Commencement (SC). The negative Dst value indicates ring currents injection. Smaller the Dst value, the greater the disturbance in the ring current.

The strength of the geomagnetic storm can be classified with the Dst value. The main acceptance of the classification suggests that the storms with a -100 nT or less minimum Dst values are great or intense, the ones between -50 and -100 nT are moderate, and the ones between -30 and -50 nT are weak storms (Gonzalez et al., 1994).

2.4.2 AE

AE stands for auroral electrojets which are mainly used for magnetospheric substorm indications. AE is obtained by two different indices which are AU (Auroral Upper) and AL (Auroral Lower). They are calculated by the magnetic field measurements done at the 13 auroral stations around 70°N, and they indicate the electrical currents and ionospheric conductance. AU and AL are the greatest strengths of eastward and westward electrojets respectively. AU and AL are superposed for every day and while the upper envelope gives AU, the lower envelope gives AL. AE is the difference between AU and AL. Its resolution is in 1 minute, and are mostly available since 1957. Even though there is not an officially accepted threshold for the substorms, approximately 500 nT of AE might be considered to show a magnetospheric substorm.

2.4.3 Kp

Kp is an extension of the Planetary-K index. It is measured from 13 stations which are located at subauroral latitudes. It is calculated with the disturbances in horizontal geomagnetic field components. It is based on the range between the greatest and lowest values in 3-hour periods. The K index is obtained from the conversion of the range to the local K index in a quasi-logarithmic scale. At this point, the K index is a local value for each station. (GFZ Postdam, n.d.). After the standardizing procedure, the Kp index is obtained. Its scale is between 0 and 9 with no units. While the Kp values between 1 and 4 indicate quiet geomagnetic conditions, Kp 5 indicates a minor geomagnetic storm, and Kp 9 is an extreme geomagnetic storm (NOAA, n.d.-b).

2.5 Solar Wind Data

In this study, solar wind data are obtained from ACE and WIND spacecrafts. The main parameters used are the strength of the southward interplanetary magnetic field (IMF Bz), and dynamic pressure (P_{dyn}). The other parameters used in the statistical part of the study are the strength of the total interplanetary magnetic field (IMF Bt), solar wind ion density, and solar wind velocity. IMF Bz and dynamic pressure are two of the key parameters which affect the strength of the geomagnetic disturbances. IMF Bz is the main responsible for magnetic reconnection which causes disturbance in the magnetotail dynamics and consequently magnetic substorms. Dynamic pressure is responsible for the compressing at the nose of the magnetopause, thus, its effect is highly important in the dayside magnetosphere. Even though there is no threshold for dynamic pressure solely in terms of geomagnetic disturbance, IMF Bz is considered a possible indicator in geomagnetic disturbance estimations, and the threshold might be taken as approximately -10 nT.

$$P_{dyn} = 2nmV^2 \tag{2.8}$$

In the equation for dynamic pressure, n stands for ion number density, m represents the mass of a proton, and V represents the solar wind velocity. The equation is multiplied under the assumption of there are equal numbers of electrons and protons in the coming plasma, and the mass of an electron is ignored. In this study, nPa is used as the dynamic pressure unit.

Advanced Composition Explorer (ACE or Explorer 71) is a NASA spacecraft launched in 1997 to explore solar energetic particles, interplanetary medium, and other sources of disturbance. Even though the mission duration was estimated at 5 years, it is still a data source to this day. The other spacecraft used WIND is also a NASA spacecraft. It launched in 1994 and the data is still available. Both ACE and WIND are stationed at Lagrange point 1, and the data are obtained from the NASA Space Physics Data Facility web page (NASA, n.d.)

3. METHODS

This study can be examined in two parts as statistical analysis and case studies. The aim of the statistical part of the study is to determine the general behavior of ionosphere and ground-level interactions over mid-latitudes. This part consists of approximately 40 storm parameters which are mostly the maximum or minimums of each storm. There are distributions and correlations for 36 geomagnetically disturbed days. The case study part consists of 3 thorough analyses for every subject including both ground and ionospheric levels.

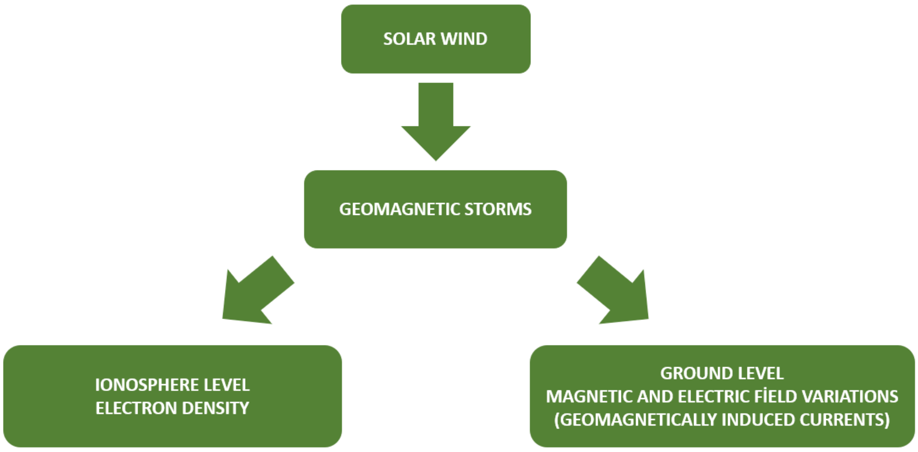

Figure 3.1 : Flowchart of the study.

In the basic method that has been followed, the main source is Sun, thus, the solar wind. Solar wind causes geomagnetic disturbances in the magnetosphere and affects the near-Earth environment, and creates geomagnetic storms. The effects of these storms can be measured and felt in many areas and levels, yet in this study, the effects in the ground and ionospheric levels are investigated. The Figure 3.2 summarizes the basic information about the data that has been used, the measurements, and the parameters which have been considered.

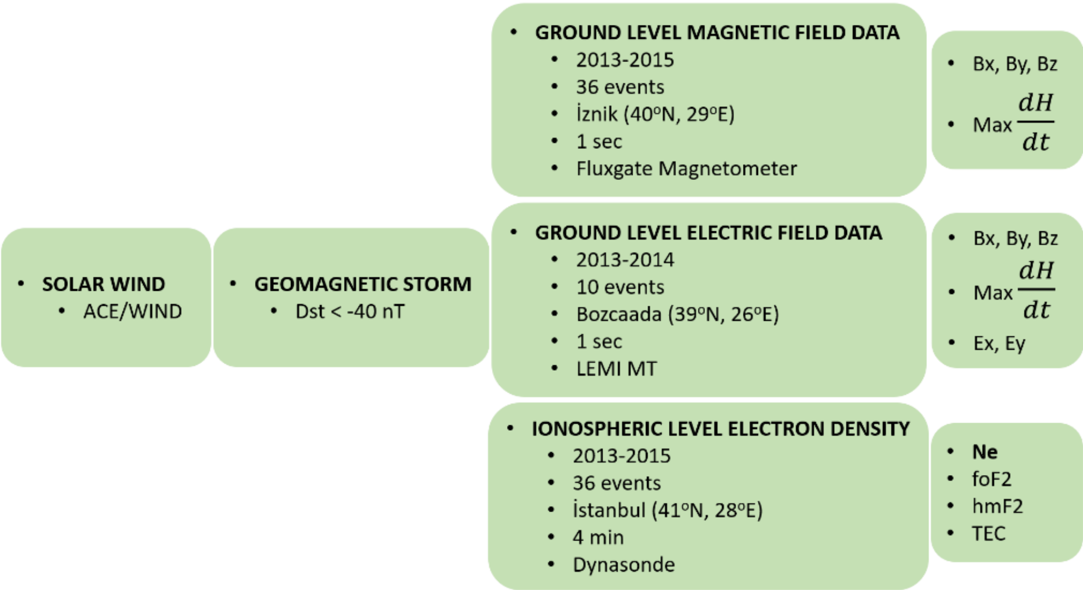

Figure 3.2 : Summary of the data have been used.

In the Figure 3.3 the places where the data measured over Marmara region can be seen as Istanbul, Bozcaada, and Iznik.

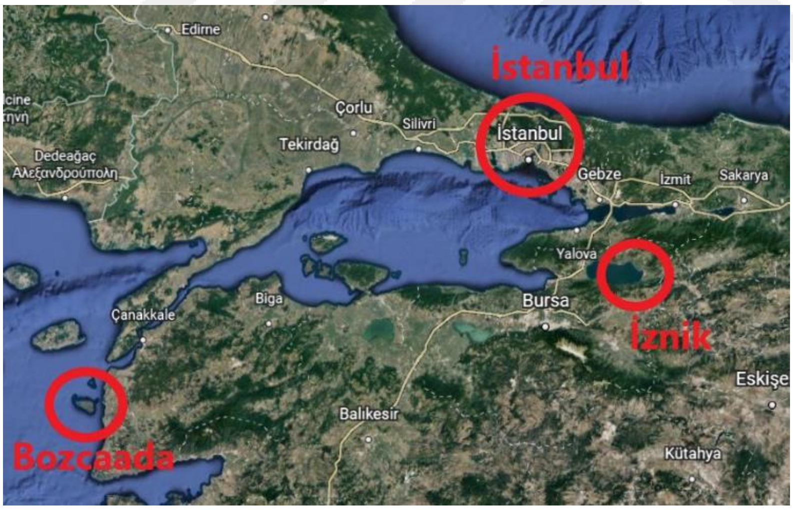

Figure 3.3 : Map of the locations where the data are measured.

3.1 Selection of Cases

Solar cycle 24 approximately started in 2008 and ended in 2019. The solar maximum was in 2014. In this study, the time around the solar maximum has been chosen to study. Thus, it has been focused on 2013 and 2015. 73 geomagnetically disturbed days have been chosen between 2013 and 2015 based on the Dst index. Among these 73 days, only 36 of them the 1-sec resolution geomagnetic field measurements were available. Hereby, 36 geomagnetically disturbed days have been chosen to study between 2013 and 2015. The selection criteria for geomagnetically disturbed days is that the minimum Dst should be lower than -40 nT for the chosen day. The storm days have been selected as the day when the Dst reaches its local minimum. The Table 3.2 shows the days included in the statistical part of the study.

Table 3.1 : Complete list of selected cases and their minimum Dst values.

Storm Day	Minimum Dst
17 January 2013	-52
26 January 2013	-51
1 March 2013	-55
17 March 2013	-132
29 March 2013	-59
24 April 2013	-48
1 May 2013	-72
18 May 2013	-61
25 May 2013	-59
1 June 2013	-124
7 June 2013	-78
29 June 2013	-102
6 July 2013	-87
10 July 2013	-56
14 July 2013	-81
4 August 2013	-50
27 August 2013	-59
2 October 2013	-72
9 October 2013	-69
15 October 2013	-49
30 October 2013	-56
7 November 2013	-50
9 November 2013	-80
16 November 2013	-40
8 December 2013	-66
19 February 2014	-119
27 February 2014	-97
12 April 2014	-87
30 April 2014	-67
12 September 2014	-88
10 November 2014	-65
18 February 2015	-64
17 March 2015	-222
7 September 2015	-70
9 September 2015	-98
20 September 2015	-69

Among these 36 cases, 3 cases have been chosen to study thoroughly based on the interest of the study. These 3 cases are 17 March 2013 which is also known as St. Patrick Storm 2013, 27 February 2014, and 9 September 2015. 17 March 2013 has been chosen since it is a famous storm and has one of the greatest dH/dt values with smooth electron density data. On 27 February 2014, geoelectric field measurements, and ionospheric electron density time series show a positive effect throughout the storm. On 9 September 2015, the ionospheric electron density difference shows a negative effect. Thus, to be able to compare cases with negative and positive ionospheric effects, 27 February 2014 and 9 September 2015 were appropriate selections.

3.2 Case Analysis

Three cases from 3 different years have been thoroughly analyzed in this part. The solar origins of the storms have been determined via various coronagraph and solar imagery obtained from NASA SDO and LASCO. The geomagnetic effects of these cases have been investigated with geomagnetic indices and different model outputs. For each case, the time series of dH/dt and electron density differences, and solar wind parameters are analyzed.

3.2.1 Phase analysis

Initial, main, and recovery phases can be used to categorize geomagnetic storm phases. When the Dst index is larger than 0, which indicates a sudden commencement, that time period is known as the initial phase. The period of time between the sudden drop in Dst and its local minimum is the main phase. The recovery phase, which lasts until Dst reaches -15 nT, is the period during which the geomagnetic field returns to its normal state (Partamies et al., 2013).

3.3 Statistical Analysis

The first of this part is the histograms since one of the main goals of this study is to find the general behavior during the storms. Thus, looking for the histograms is one of the basic steps toward that goal to see the distribution of the values.

The most comprehensive part of the study is the correlation between parameters. The most basic correlation method is chosen at the beginning of the study. The linear relationship between the parameters is determined via scatter plots and the calculation of Pearson correlation coefficients. Pearson correlation coefficient shows the linear correlation between two data sets. It is basically the ratio of the covariance of the variables to the product of their standard deviations.

$$\rho(A,B) = \frac{1}{N-1}\sum_{i=1}^{N}\left(\frac{A_i-\mu_A}{\sigma_A}\right)\left(\frac{B_i-\mu_B}{\sigma_B}\right) \tag{3.1}$$

This equation gives the Pearson correlation coefficient which is also commonly referred to as r. In this equation N represents the number of observations, μ represents the mean, and σ represents the standard deviation. Pearson correlation coefficient does not have any units and the value varies between -1 and 1. -1 indicates the perfect inverse linear correlation while 1 indicates perfect linear correlation. The closer the coefficient to 0, the worse the correlation (Turney, 2022).

3.3.1 Student's t-test

The intensity and direction of the linear link between two variables are indicated by the correlation coefficient, or r. However, the number of observed data points in the sample also affects how reliable the linear model is. It is important to consider the sample size 'n' together with the correlation coefficient value 'r'. To determine if the linear relationship in the sample data is strong enough to utilize to predict the relationship in the population, a hypothesis test of the "significance of the correlation coefficient" is conducted.

Null and alternative hypothesis (H0 and H1, respectively) are determined to be able to perform the test. In this study, null hypothesis is that there are no relationships between two variables, and the alternative hypothesis is that there is a relationship between the variables. In order to considered a correlation coefficient as statistically significant, null hypothesis has to be rejected and alternative hypothesis has to be accepted.

$$t_{score} = \frac{r\sqrt{n-2}}{\sqrt{1-r^2}} \tag{3.2}$$

T-score is calculated with the Equation 3.2 and compared with the critical t-value found from the t-distribution table. In this study, the significance level is decided as 95%, and based on this two t-value is used for calculations for 36 and 10 samples. For 36 samples, the degree of freedom is 34, and the critical t-value is 2.032 for two-tailed t-test. For 10 samples, the degree of freedom is 8, and the critical t-value is 2.306. In the situation where calculated t-score is greater then the critical t-value, the null hypothesis is rejected. In the Figure 3.4, the area shown as A represent the acceptance of null hypothesis, and the area shown with P represents the rejection of null hypothesis. The -t and t on the figure represents the critical t-values determined via t-distribution table. If the calculated t-score is in the area represented as P, it means that the correlation coefficient is statistically significant. Additionally, p-value is another indicator to understand in which significance level the coefficient is statistically significant. The p-value can be decided based on the calculated t-score on t-distribution table. It is more significant at the p-value approaches to 0.

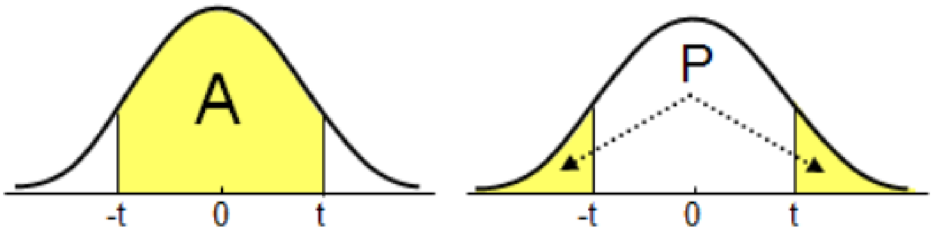

Figure 3.4 : t-distribution*(*T-Distribution Table (Two-Tailed), *n.d.)*.

3.3.2 Parameters

The statistical part of the study consists of 36 cases and various parameters. Each of these parameters was chosen to answer a specific question. These parameters can be classified into 5 categories which are geomagnetic indices, geomagnetic field, solar wind, ionospheric electron density, and electric field (based on 10 cases available).

3.3.2.1 Geomagnetic indices

The most commonly used geomagnetic indices Dst, AE, and Kp are included in the analysis. These 3 indices indicate the strength of the storm; thus, it is possible to see how the other parameters depend on the strength of the storm.

Maximum Dst represents the sudden commencement which is the compression made by the solar material to the nose of the magnetosphere. In order to be able to see if there is a dependence between any of the other parameters and this compression, maximum Dst is also included in the analysis.

3.3.2.2 Geomagnetic field

In the geomagnetic field part of the study, the main parameter is the maximum time derivative of the horizontal geomagnetic field (dH/dt), yet there are 14 parameters chosen to investigate in this study. Other than the max dH/dt during the whole storm, the maximum in each phase (initial, main, and recovery) has been studied to determine in which phase of the storm the maximum dH/dt is seen and in which phase it is expected to see the maximum dH/dt.

The timing of the maximum dH/dt is also been investigated based on the Dst index. The maximum dH/dt during the minimum Dst is chosen to see whether the maximum dH/dt is expected during the peak of the storm. With the same logic, the maximum dH/dt during the sudden commencement is chosen to see if there is a relation between the compression at the magnetopause and the maximum dH/dt. The other way is also included such as the Dst value around a 1-hour window of the maximum dH/dt.

The last parameter chosen for the geomagnetic field data is the duration of the whole storm as well as each phase of the storm. The motivation behind this selection is to estimate if there is a relation between the duration of any phase of the storm with other parameters such as the geomagnetic indices. Additionally, the maximum dH/dt in each phase of the storm has been analyzed in order to determine in which phase the maximum dH/dt is expected.

3.3.2.3 Solar wind

The parameters for solar wind are ion density, solar wind velocity, total IMF, southward IMF, and dynamic pressure. Even though the main focus was on the IMF Bz and dynamic pressure, the dependency on the other parameters is among the concerns of this study.

3.3.2.4 Ionospheric electron density

For the statistical part, the maximum electron density difference between active and quiet days is the main parameter. In the ionosphere, the effect of the geomagnetic storm can be negative or positive, which means the electron density might increase or decrease. Even though the reason behind is not understood properly, the aim here is to be able to see the general behavior over mid-latitudes. Thus, 4 parameters have been chosen. The first one is the absolute maximum difference to see the absolute value without concerning whether it is negative or positive. Additionally, it is average throughout the storm. And finally, the negative and positive differences are to determine whether the difference values are higher when the effect is negative or positive.

A spike removal algorithm has been used for the electron density data. The analyses are done with MATLAB tool and a custom package has been used which is written by Dr. Erol Kalkan. This function interpolates between prior and subsequent data points to replace spikes (outliers) that surpass the threshold value, or it replaces them with NaN depending on the user's preference. The mean of windowed data that is centered on spike sites, plus or minus a certain number of standard deviations, is the threshold. To find spikes, this algorithm applies histogram approach of Solomon et al. (Solomon et al., 2001) (Kalkan, 2019). Window size to compute mean and standard deviation for thresholding has been chosen as 20, and number of standard deviations above and below mean has been chosen as 1 since they gave the best results.

3.3.2.5 Electric field

There are only 10 cases for this section due to the past measurement capabilities. The maximum eastward and northward electric fields, and the maximum time derivatives of eastward and northward geomagnetic fields, since the main goal is to show Faraday’s Law.

4. CASE ANALYSIS AND RESULTS

3 cases from different years have been analyzed in this section. The cases are chosen from 3 subsequent years to answer different questions. These cases are 17 March 2013, 27 February 2014, and 9 September 2015. Each case has been analyzed thoroughly to understand the changes caused by solar storms at both ground and ionospheric levels.

4.1 17 March 2013

17 March 2013 is also known as the St. Patrick storm 2013 in the space weather literature. Figure shows that the Dst value decreased up to -132 nT on 17 March at 21.00 UTC, and AE increased up to 2689 nT on the same day at 16:51 UTC according to the official website of World Data Center for Geomagnetism, Kyoto. Based on NASA CCMC Donki webpage (NASA, n.d.-a), the Kp level increased up to 6 on the same day at 06.00 UTC which indicates a moderate storm according to NOAA Space Weather Scales (NOAA, n.d.-a).

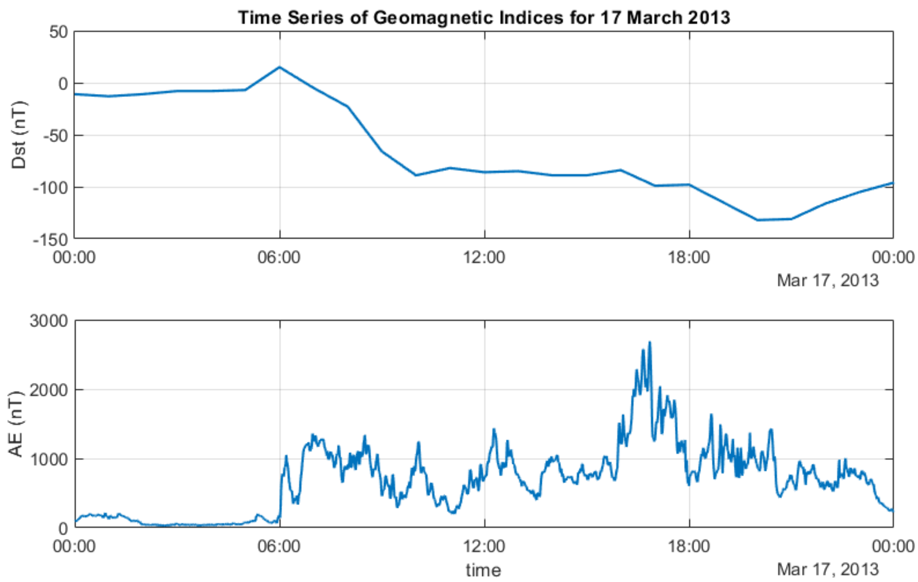

Figure 4.1 : Time series of Dst and AE for 17 March 2013.

Based on the coronagraph imagery obtained via SOHO LASCO, a CME erupted on the Sun on 15 March 2013 06:54 UTC with an M1.2 class flare which peaked at 06.58 UTC. The speed of the CME was 1485 km/s which makes it an O-type CME based on the official website of NASA CCMC DONKI. The CME caused a solar energetic particle (SEP) event on 16 March. The CME arrived at Earth on 17 March at 05:59 UTC and caused an interplanetary shock (IPS). The Kp level increased up to 6 at 06:00 and a geomagnetic storm alert has been given.

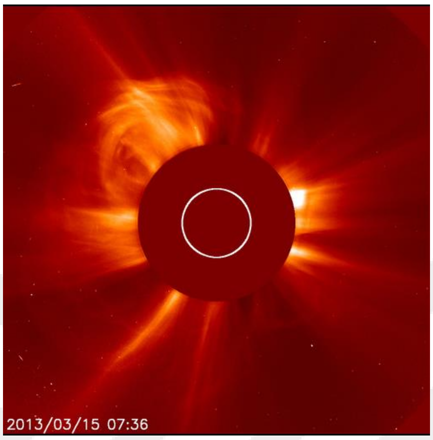

Figure 4.2 : Coronagraph imagery via SOHO LASCO C2 on 15 March 2013 (NASA, n.d.-b).

The first parameter which has been analyzed is the time derivative of the horizontal geomagnetic field (dH/dt). In the figure, the panels show the Dst and dH/dt for the whole storm period. Based on the criteria selected the storm started on 17 March at 05:30 UTC, and the initial phase only lasted about 30 minutes before the main phase start at 17 March 06:00 UTC at the time the CME arrive. The main phase lasts 14 hours and the recovery phase starts on 17 March at 20:00. The recovery phase lasts more than average which had been found and explained in the following sections. It lasts 111 hours which is approximately 4.5 days, and the storm ends on 22 March at 11:00 UTC.

Even though, as will be explained later in this study as the outcome of the statistical study that the maximum dH/dt of a storm rarely occurs in the initial phase, in this particular case the maximum dH/dt 1.18 nT/s occurs on 17 March 06:01:09 UTC. In this case, the maximum dH/dt is affected by the sudden commencement. The maximum dH/dt is also exceeds the threshold of 1 nT/s. Thus, it can be considered a significant storm for the occurrence of GIC. After the sudden changes and significantly high dH/dt values around the sudden commencement, there is another local peak around 18:00 UTC which is 2 hours before the peak of the storms where the Dst is at its lowest value at 20:00 UTC. The time series which includes only 17 March can be seen in the Figure 4.3. It can be said from the Figure 4.3 that the most fluctuations and greater dH/dt values are seen between the sudden commencement and the peak of the storm.

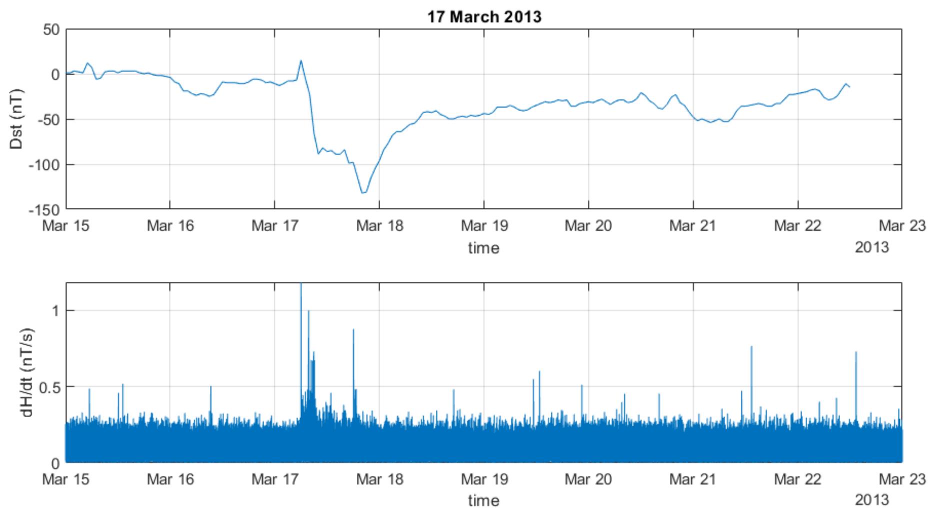

Figure 4.3 : Time series of Dst and dH/dt for 17 March 2013 storm.

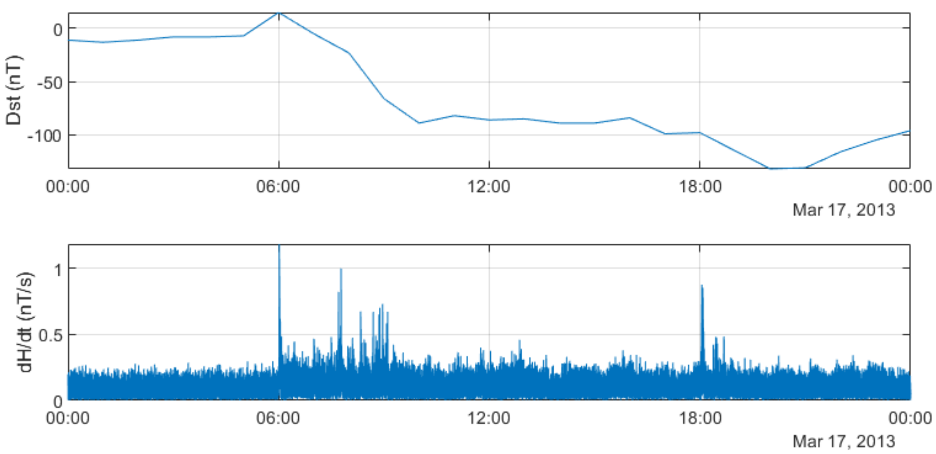

Figure 4.4 : Time series of Dst and dH/dt for 17 March 2013.

In the Figure 4.5, in addition to the Dst and dH/dt, time series of the solar wind parameters IMF Bt and Bz, dynamic pressure, ion density, and velocity are seen for the entire storm period. Here it can clearly be seen that the maximum dH/dt values are seen mostly at the initial and main phases. The total IMF is reached up to 22 nT during the beginning of the main phase and slowly returns to the nominal conditions

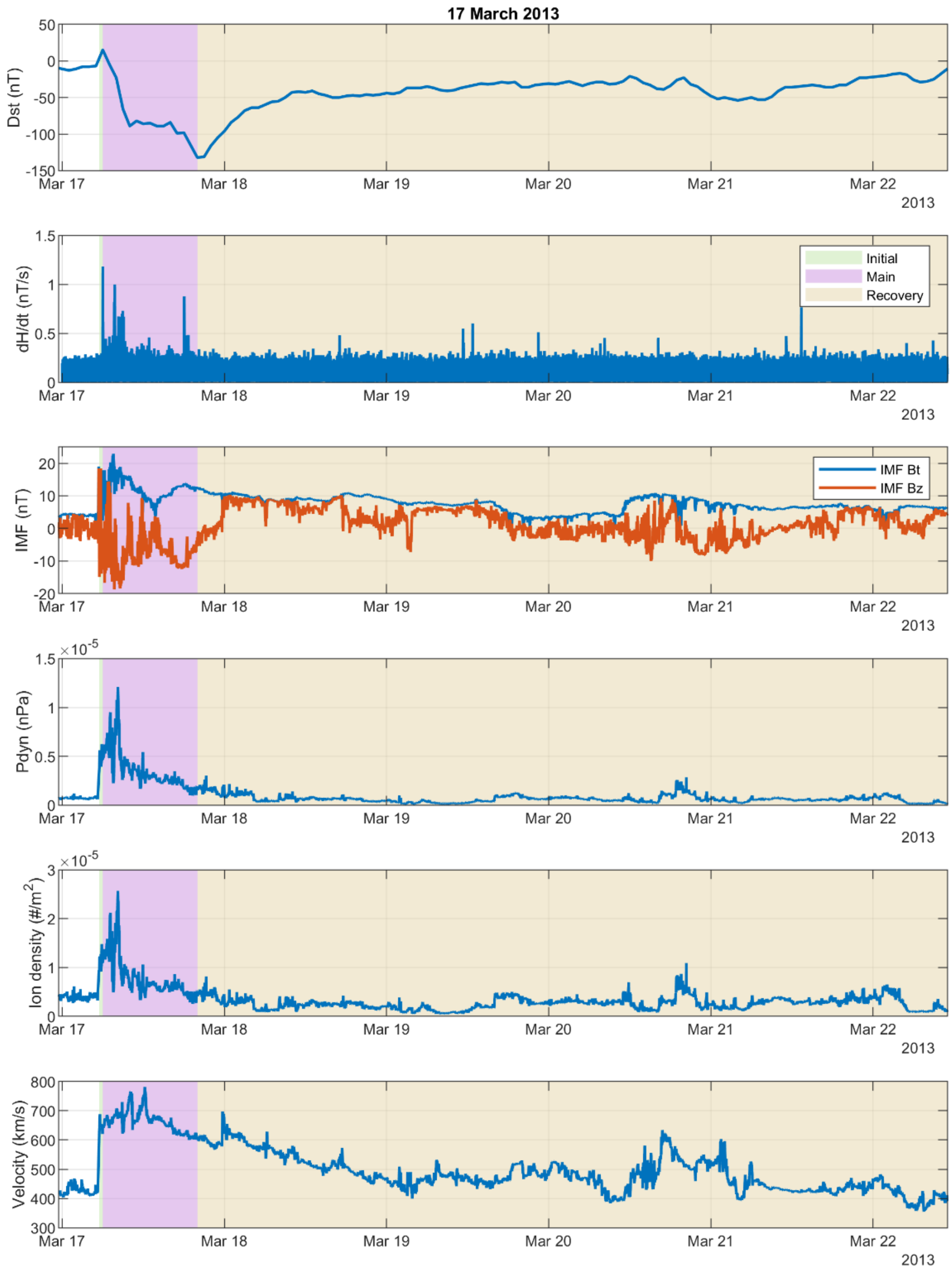

Figure 4.5 : Time series of Dst, dH/dt, IMF Bt and Bz, Pdyn, ion density, and velocity for 17 March 2013 storm.

throughout the storm. The southward IMF is also reached -18 nT strength also during the beginning of the main phase, and it continues to fluctuate until the end of the storm. Dynamic pressure is another important parameter that reaches up to 1.2x10-5 nPa at the same time when both total and southward IMF reaches their maximums, and return to their nominal values until the storm ends. Ion density follows the same trend as dynamic pressure as it reaches 2.6x10-5 #/m3. Velocity follows a different trend due to its nature. It sharply increases as the storm begins and does not return to its nominal values until very late in the recovery phase. According to this figure, it can be assumed that almost every fluctuation in dh/dt happens during the main phase of the storm where all the solar wind data shows great changes.

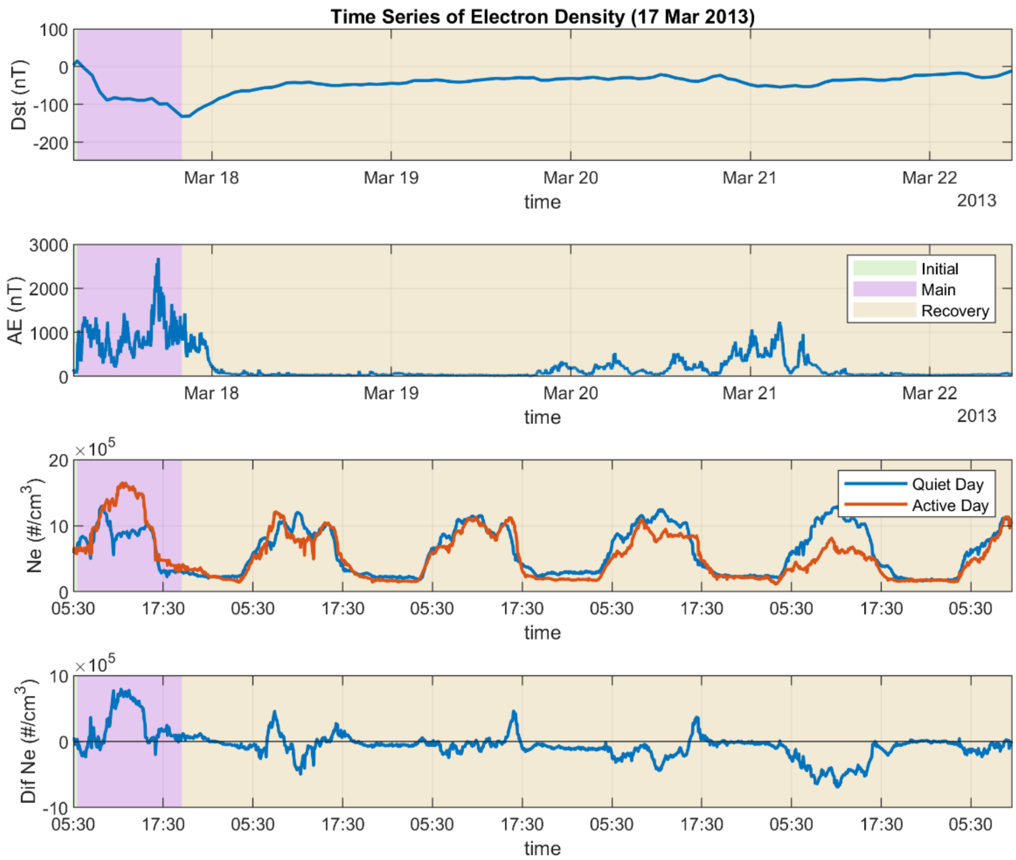

Figure 4.6 : Time series of Dst, AE, electron density, and electron density difference for 17 March 2013 storm.

In the Figure 4.6, in addition to the geomagnetic indices Dst and AE, the electron density for quiet and active days, and the difference between them are seen for the whole storm period. The quiet day period chosen for this case is 7-12 March 2013 when geomagnetic conditions are quiet. The difference is found by subtracting the quiet day electron density from the active day period. The electron density panels show that during this storm the effect in the ionosphere was positive which means the electron density increases during the storm as a reference to the quiet day. When the entire storm period is considered, it can be seen that the most effect is seen in the main phase of the storm. The electron density reaches up to $1.7x10^6$ #/cc at 12:04 UTC which means during 14:04 local time (LC), two hours after noon. The effect is solely positive during the main phase of the storm. The electron density difference is 7.9x10^5 #/cc at 11:52 UTC. Even though there are both positive and negative effects throughout the storm period, the maximums are seen at the main phase. Both Dst and AE show their greatest variations during the main phase as well. One thing which should be considered for this period is 21 March. On 21 March a negative effect is seen and seems like the electron density decreases and the only change in the geomagnetic

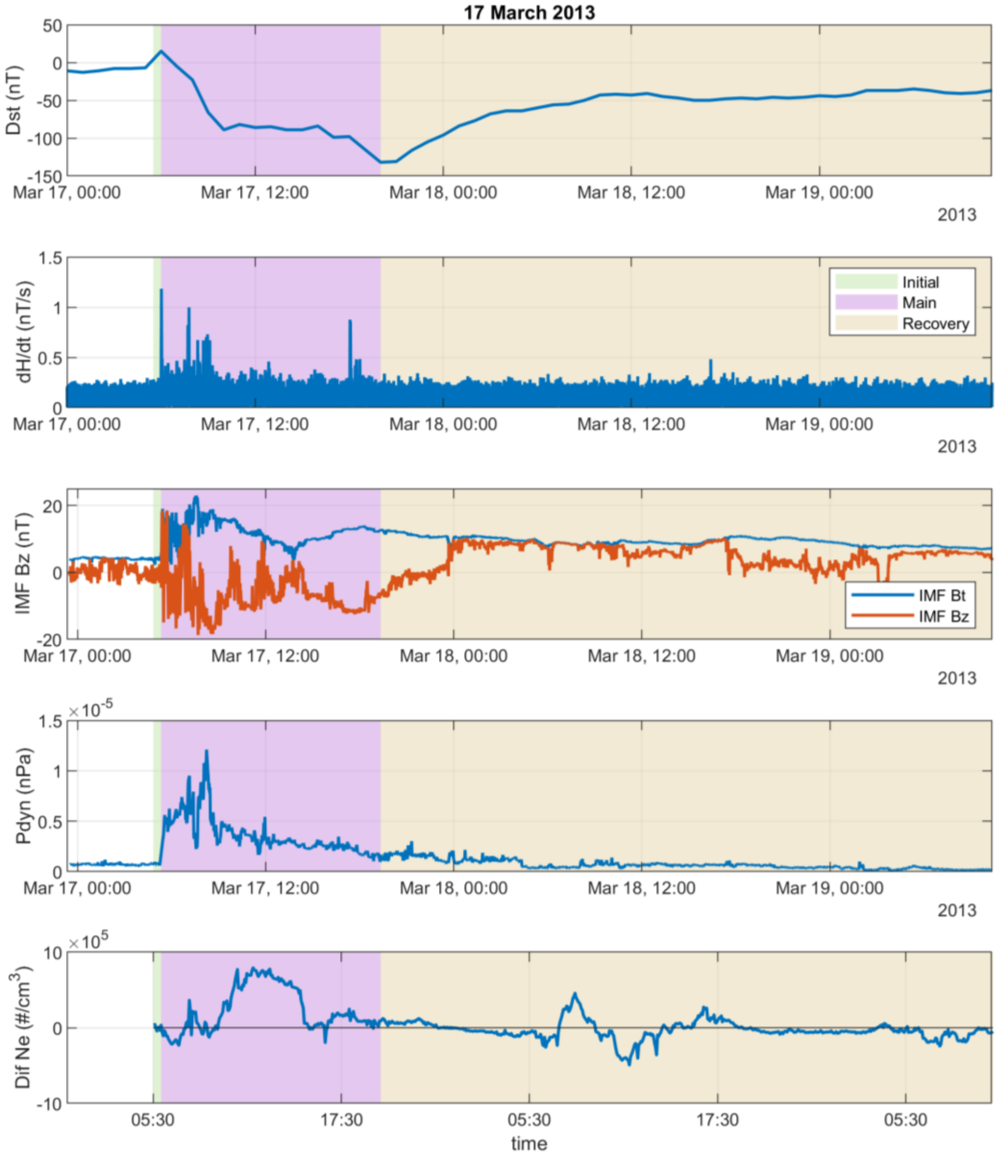

Figure 4.7 : Time series of Dst, dH/dt, IMF Bt and Bz, Pdyn, and electron density difference for 17 March 2013 storm.

indices is AE which starts to fluctuate and reaches its local maximum at around 04:00 UTC, 8 hours before the local minimum for electron density difference. Further investigations should be made in order to determine whether the electron density decrease on 21 March is related to the increase in AE or not.

In the Figure 4.7, the time series for the most significant parameters are seen. It is clear that all of the greatest variations are seen during the main phase of the storm including dH/dt, IMF Bt and Bz, dynamic pressure, and the difference in electron density. The changes in dH/dt seem almost perfectly aligned with Dst, and IMF Bz. Yet on the other hand, as expected ionosphere does not respond to the changes in geomagnetic conditions quickly. The electron density starts to increase a few hours after the storm starts. The reason behind the positive and negative effects on the electron density difference on 18 March is not clear. However, the most significant effect on the first day of the storm also shows alignment with the parameters but with a natural delay.

4.2 27 February 2014

27 February 2014 is the only case study that includes electric field measurements in this study. The minimum Dst reached, in this case, is -97 nT on 27 February at midnight which can be classified as a moderate storm based on the Dst value. The maximum AE is 1171 nT which reached its peak on 27 February at 18:54 UTC. Kp level reached 6 on the same day at 16:00-19:00 UTC period which indicates a moderate storm as well. In the Figure 4.8, the Dst and AE values for 27 February, 2014 can be seen for the entire storm period. In this case, the trend of the Dst and AE indices are almost the same as they both reach their extremes around the same phases of the storm.

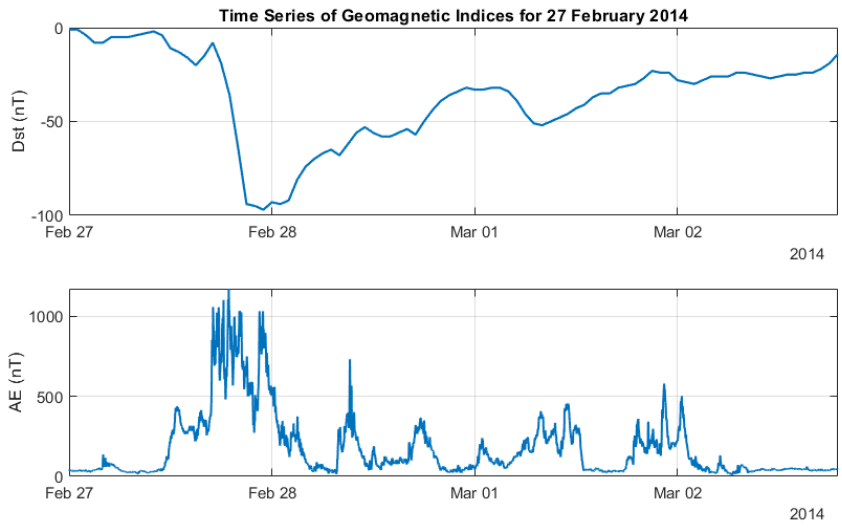

Figure 4.8 : Time series of Dst and AE for 27 February 2014 storm.

This storm is caused by a CME eruption detected on SOHO LASCO imagery on 25 February 2014 at 01:25 UTC and had a speed of 1670 km/s which is an O-type CME. The CME erupted with an X4.9 flare which peaked on 25 February at 00:41 UTC. This CME caused SEP on 25 February almost 5 hours after the eruption. The CME arrived at Earth on 27 February at 16:10 UTC and caused a geomagnetic storm based on the increase in Kp on the same day 2 hours after the arrival at 18:00 UTC.

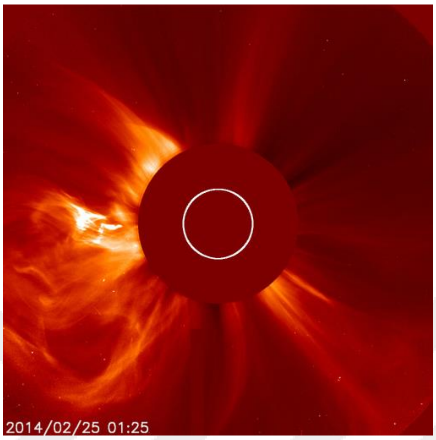

Figure 4.9 : Coronagraph imagery via SOHO LASCO C2 on 27 February 2014 (NASA, n.d.-b).

The first parameter to analyze is dH/dt throughout the storm which starts on 27 February 00:00 UTC and ends on 2 March 19:00 UTC. Based on the Figure 4.9, Even though, the maximum dH/dt is seen on 1 March at 04:01 UTC which is in the recovery of the storm, the main fluctuations in dH/dt are seen in the main phase of the storm which is between 16:51 and 21:43 UTC on 27 February. The maximum dH/dt seen in this period is 0.55 nT/s which is considerably small if the 1 nT/s threshold is considered. When the Dst trend is considered, it can be seen that there is another decrease on 1 March between 00:00 and 12:00 UTC, since that was a highly active period with lots of CMEs, that decrease might have happened due to a less significant CME. Thus, that maximum dH/dt at 04:01 UTC might be a result of that less significant geomagnetic disturbance during the recovery of the main storm.

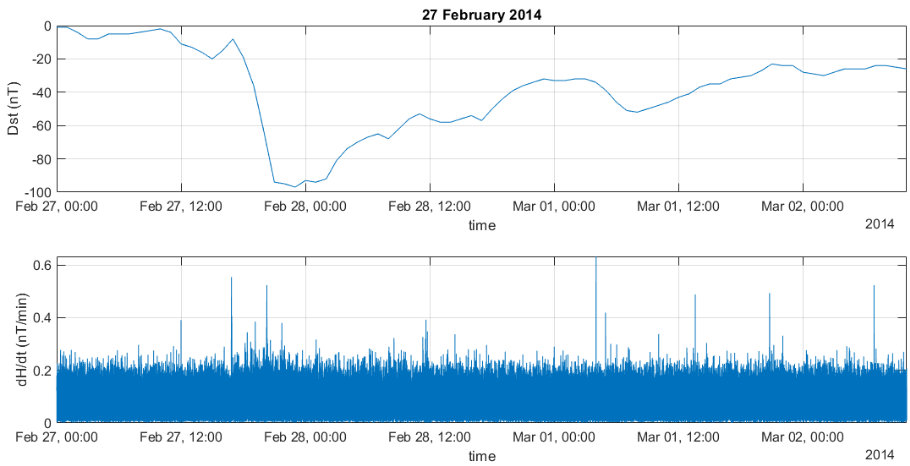

Figure 4.10 : Time series of Dst and dH/dt for 27 February 2013 storm.

The Figure 4.10, shows the Dst, dH/dt, and solar wind parameters for the entire storm period with colored storm phase identification. The delay time for this case is calculated as 65 minutes based on the average solar wind velocity on 27 February by dividing the L1 point where WIND is located 1500000 km away from Earth by the average solar wind speed. As mentioned the main fluctuations and increases in dH/dt are seen in the main phase of the storm, and the first look at the solar wind parameters also shows the same trend. The total IMF Bt increases up to 20 nT during the main phase of the storm and slowly returns to its nominal conditions with the recovery phase. The more important parameter southward IMF decreases up to -18 nT also during the main phase, and follows a similar pattern with IMF Bt, yet IMF Bz keeps fluctuating more than IMF Bt. Dynamic pressure and the ion velocity are also at their maximum levels of $8.2x10^{-6}$ nPa and $4.5x10^{-5}$ #/m^3 during the main phase and slowly return to their nominal conditions at the same timing with IMF Bz. Solar wind speed sharply increases with the other parameters up to 506 km/s, yet by its nature, it decreases slowly until the end of the storm to its nominal conditions.

In Figure 4.11, in addition to geomagnetic indices Dst and AE, the time series of the electron densities for the active and quiet days, and the difference between them are shown. The chosen quiet day period for this case is 1-4 February 2014. In this case, it can be seen that there is a positive effect on the ionospheric electron density which means the electron density increases during the storm. The maximum electron density during the storm is $2.2x10^{6}$ #/cc on 28 February at 08:40 UTC which means 10:40 LT, before noon. The maximum electron density difference between the quiet and active

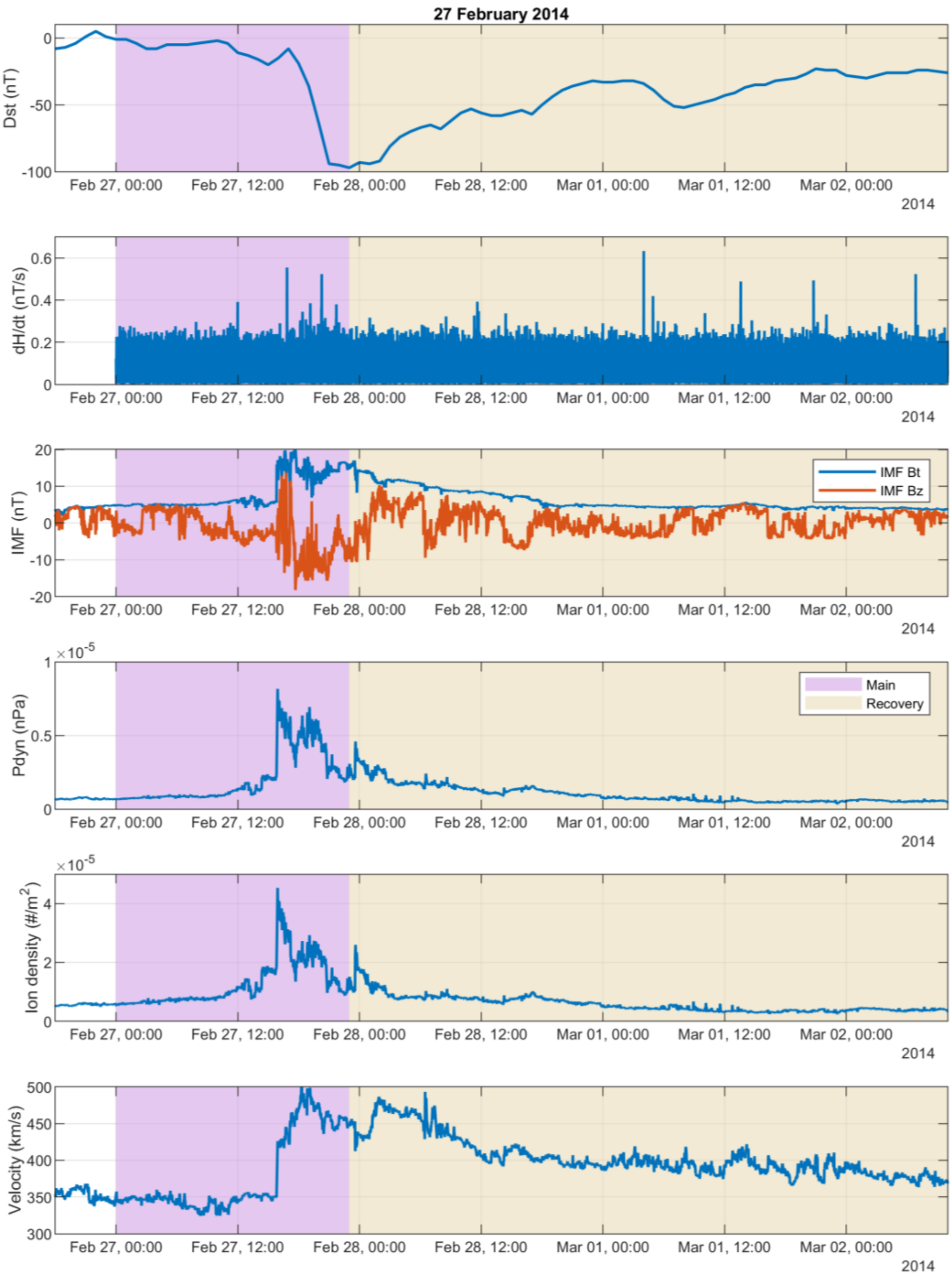

Figure 4.11 : Time series of Dst, dH/dt, IMF Bt and Bz, Pdyn, ion density, and velocity for 27 February 2014 storm.

day 9.9×10^5 #/cc on 2 March at 10:12 UTC which is 12:12 UTC, around noon. When looking at the entire storm period and the electron density differences, there is a constant difference throughout the storm. A new quiet day period should be selected to see whether the difference is caused by the geomagnetic disturbance, or is due to the time difference between the quiet and active days. By this analysis, it can be said that the greatest electron density is seen during the early hours of the recovery phase.

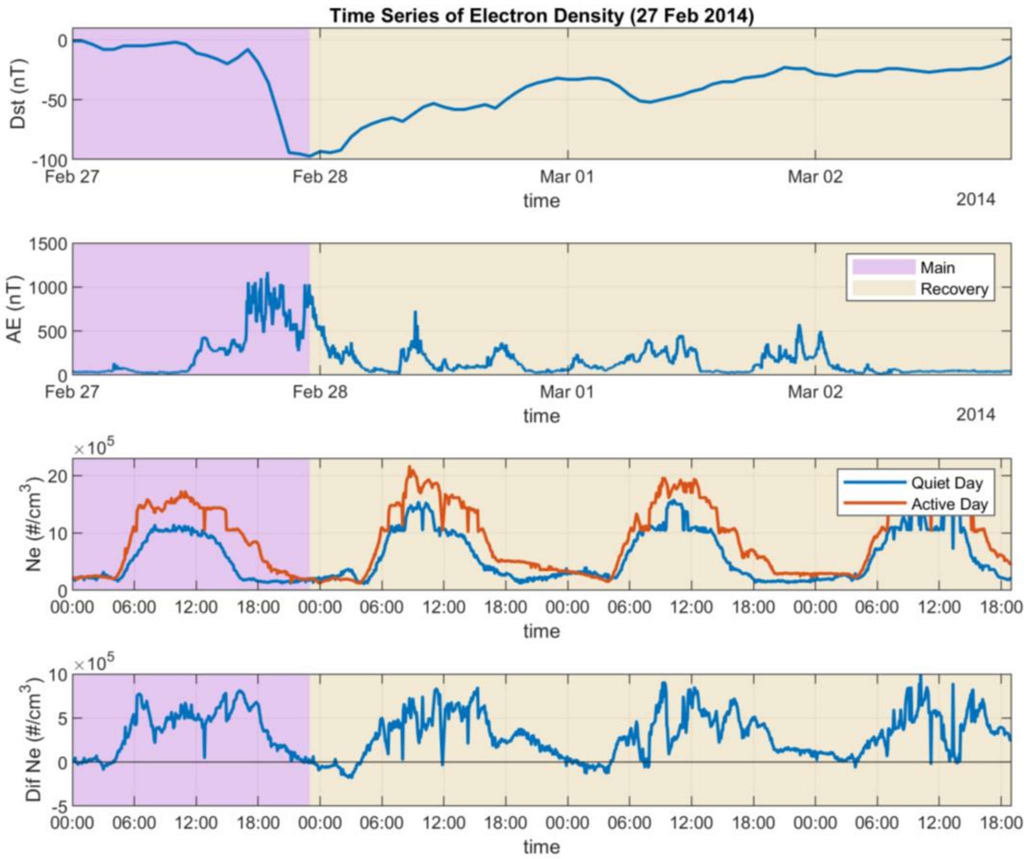

Figure 4.12 : Time series of Dst, AE, electron density, and electron density difference for 27 February 2014 storm.

In the Figure 4.12, the time series of geomagnetic indices Dst, dH/dt, solar wind parameters IMF and dynamic pressure, and the ionospheric electron density difference are seen. According to this figure, it can be said that while the changes in the dH/dt align well with the solar wind parameters, especially with IMF Bz and dynamic pressure, the same alignment cannot be seen clearly with the electron density difference. The value of the electron density difference is almost the same throughout the storm's period. Thus, nothing certain can be said about the ionospheric effect on the storm other than the positive effect of it.

In this Figure 4.13, the electric field measurements are analyzed. The time series for Dst, dH/dt measurement from Iznik and Bozcaada, and the northward and eastward electric field components from Bozcaada are seen. The comparison of dH/dt values from two different stations shows the same main fluctuations around the main phase. The dH/dt measured in Bozcaada shows different peaks than in Iznik measurements. The peak at around 1 March 12:00 UTC at Bozcaada is almost 1 nT/s, and there is also

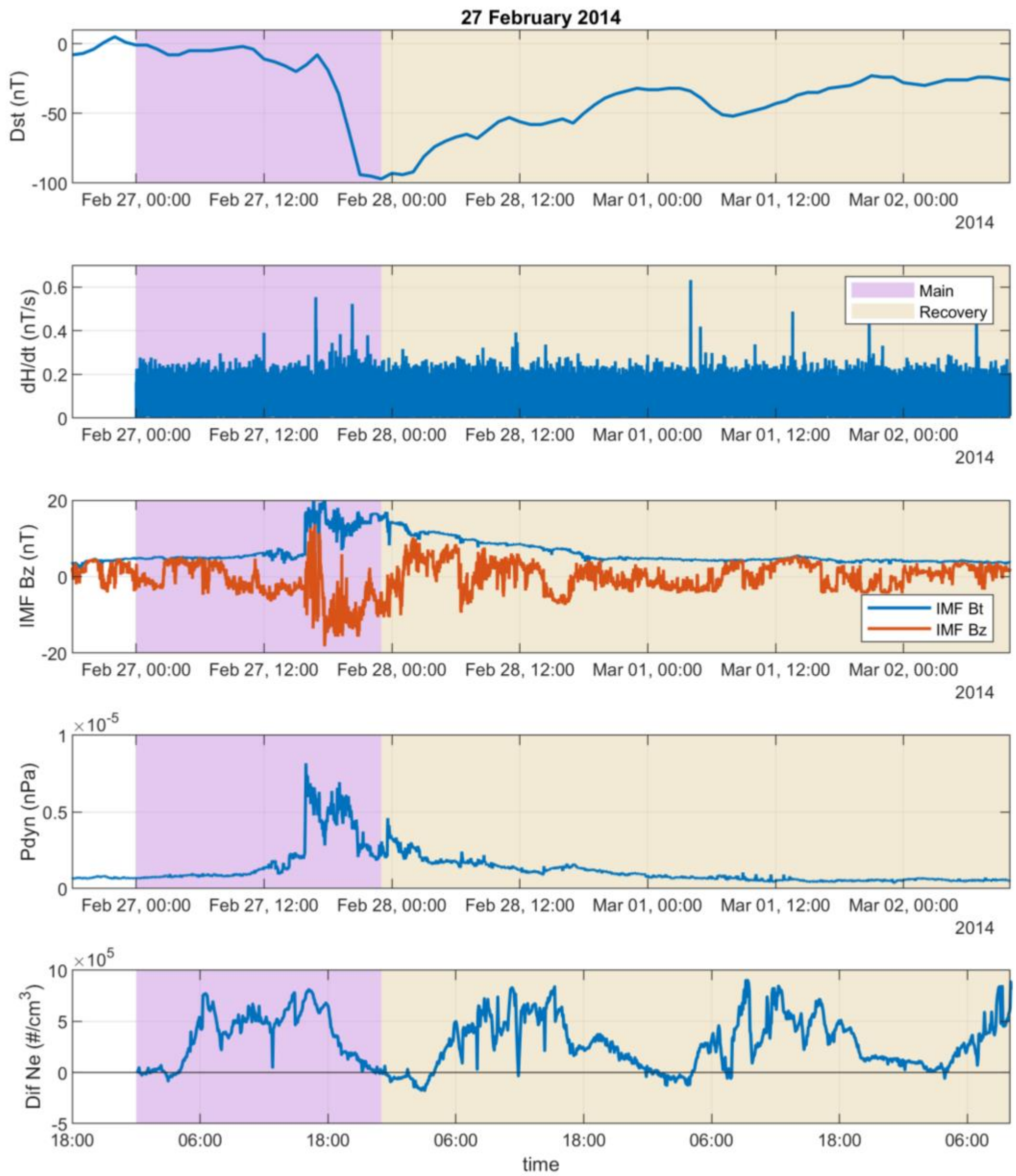

Figure 4.13 : Time series of Dst, dH/dt, IMF Bt and Bz, Pdyn, and electron density difference for 27 February 2014 storm.

a peak at the Iznik but the value is much less and insignificant among the other small peaks. Thus, the reason behind this high-value peak is unclear. Yet, the main fluctuations around the peak of the storm are considered significant and expected. Northward and eastward electric field measurements are aligned with the main fluctuations at both measurements for dH/dt. Especially, Ex shows highly clear fluctuations between the first main dH/dt peak at Iznik measurement and the decreases its degree slowly as the storm continues and returns to nominal conditions hours after the recovery phase. The fluctuations at Ey are less clear than Ex, yet highly clear during the main phase and continue to fluctuate in smaller frequencies throughout the storm.

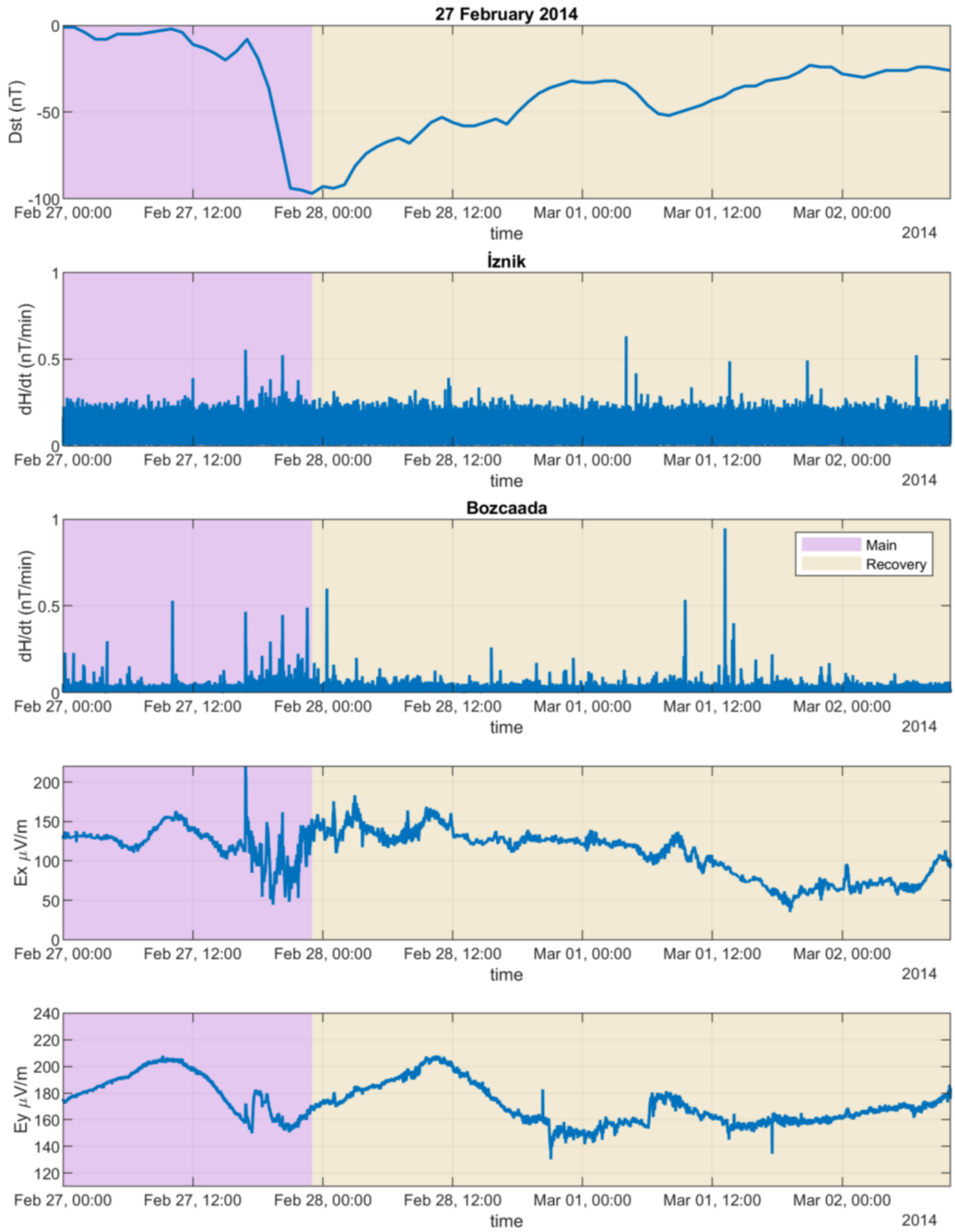

Figure 4.14 : Time series of Dst, dH/dt at Iznik, dH/dt at Bozcaada, Ex, and Ey for 27 February 2013 storm.

In Figure 4.14, Faraday's law has been analyzed by investigating the relationships between dBx/dt and Ey, and dBy/dt and Ex. The figure shows the time series of dBx/dt, dBy/dt, Ex, and Ey. The peak at the recovery phase which was unclear the causation also can be seen in dBx/dt and dBy/dt as expected. There are no signs of these peaks in Ex and Ey, thus, it did not affect the electric field. However, the main fluctuations at the end of the main phase can be clearly seen in every parameter. Thus, it can be said that indeed dBx/dt is related to Ey, and dBy/dt is related to Ex.

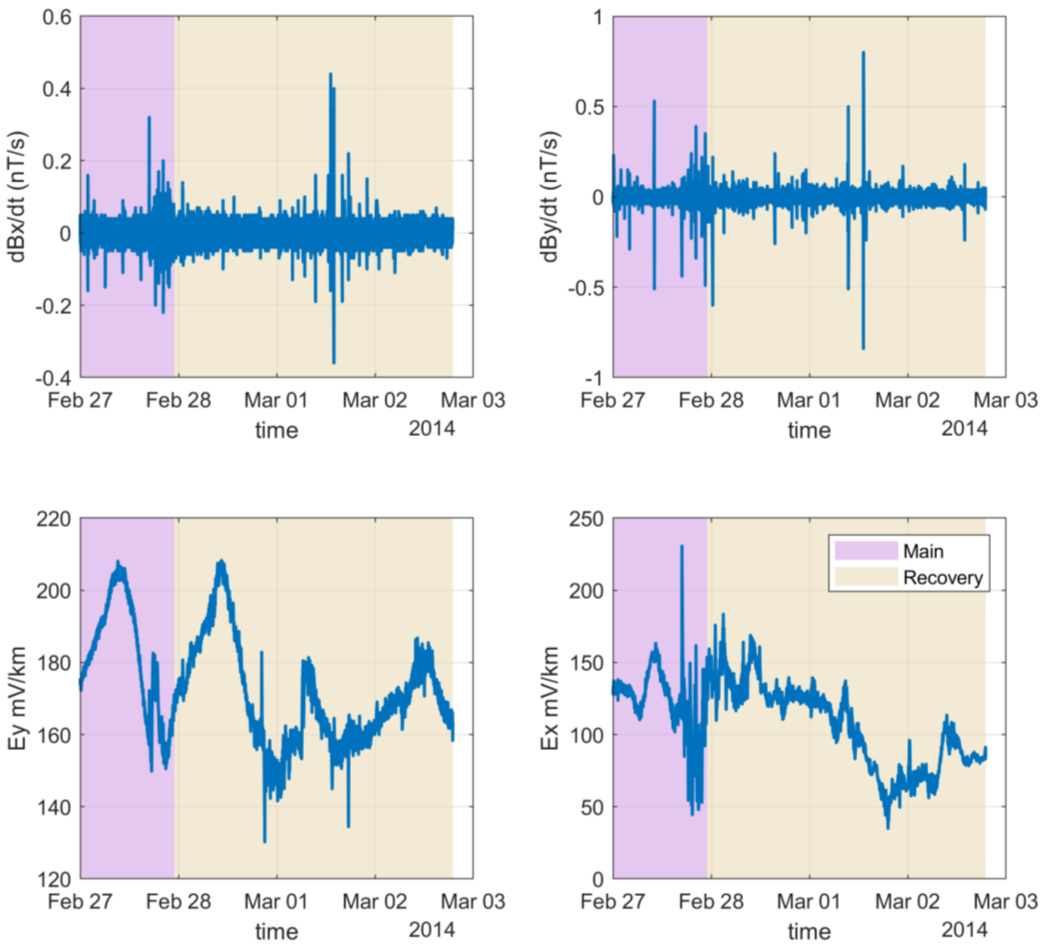

Figure 4.15 : Time series of dBx/dt, dBy/dt, Ex, and Ey for 27 February 2014 storm.

4.3 9 September 2015

9 September 2015 is chosen to analyze in order to show the negative effect on the ionospheric electron density since in the other two cases the effect was positive. This storm has no distinctive sudden commencement, implicitly there are only main and recovery phases. The storm starts on 8 September at 20:00 UTC and ends on 10 September at 21:00 UTC. The minimum Dst value for this case is -105 nT which indicates that this is an intense storm. The Dst reaches its peak on 9 September 2015 at 13:00 UTC. The maximum AE is 1591 nT on 9 September at 03:32 UTC. The Kp level reached 6 on the same day at 03:00 UTC which is considered a moderate storm based on the NOAA storm scale.

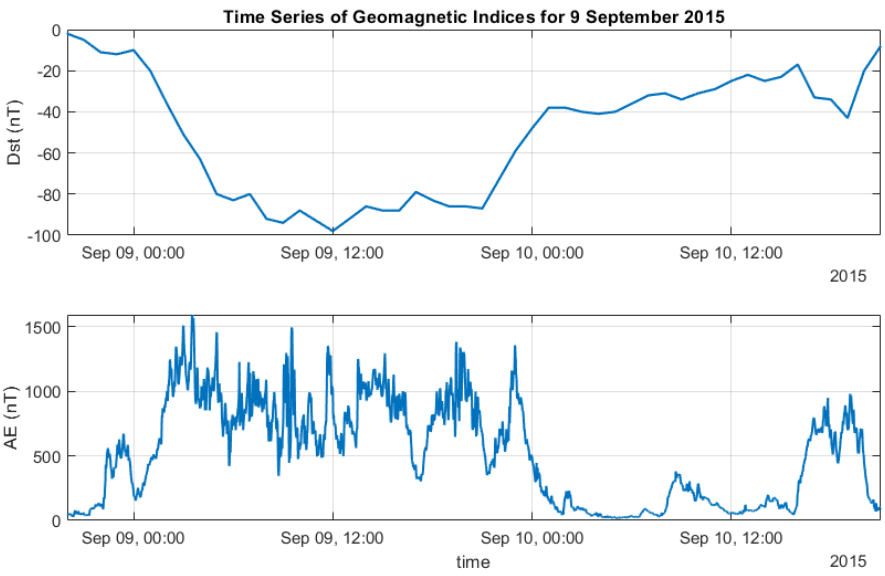

Figure 4.16 : Time series of Dst and AE for 9 September 2015 storm

This is an interesting case based on the solar source of it. According to NASA CCMC Donki Space Weather Activity website, this storm is associated with two separate faint CMEs. Since this was a highly active period, the associations between solar activity and their sources can be tricky. The CMEs can be seen in the figures, yet very vaguely. Both of the CMEs erupted on 4 September 2015. The first eruption is seen on SOHO LASCO C2 at 14:12 UTC with a very low speed of 302 km/s, and the second one was at 19:24 UTC with a speed of 325 km/s. The exact timing of the arrival of the CMEs

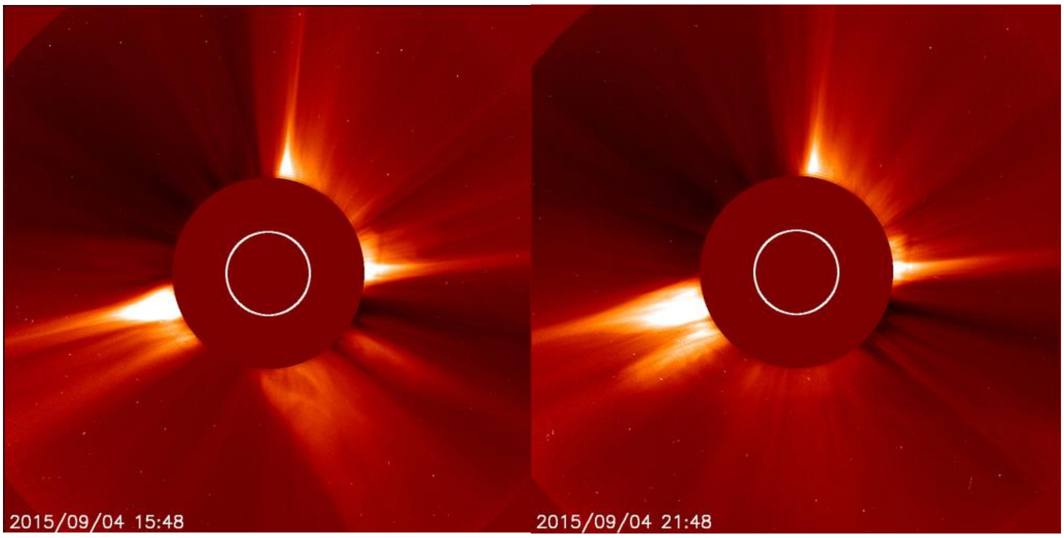

Figure 4.17 : Coronagraph imagery via SOHO LASCO C2 for 4 September 2015.

is unclear based on the satellite data, thus, they did not cause any IPS, yet they arrived in more than 4 days since they were relatively too slow. The CMEs also did not cause SEPs, radiation belt enhancements, or any other event.

The first parameter analyzed is dH/dt. The storm starts on 8 September at 20:00 UTC, so in the Figure 4.17 after the start of the storm, the first fluctuations and the peak is seen in the first hours of the recovery phase which starts on 9 September at 12:00 UTC. The maximum dH/dt is 1.5 nT/s on 9 September at 18:31 UTC which is 8.5 hours after the recovery begins. This agrees well with the statistical results of this study which will be explained in the following chapters. The maximum dH/dt value exceeds the threshold of 1 nT/s. Thus, there might be GIC.

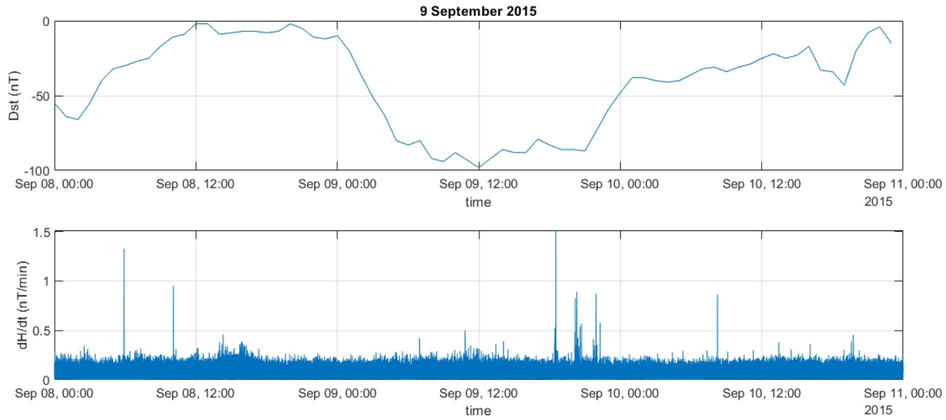

Figure 4.18 : Time series of Dst and dH/dt for 9 September 2015 storm.

In the Figure 4.18, in addition to the time series of geomagnetic indices Dst and AE, dH/dt, and the solar wind parameters IMF Bt and Bz, dynamic pressure, ion density, and velocity are seen. The delay time is calculated as 59 minutes. It has also been mentioned that this case is interesting due to it did not cause any shock and the CME arrival signatures are not seen in the solar wind parameters. The only signatures are seen at the end of the recovery phase, yet those signatures do not belong to this particular storm but rather the following storm on 11 September. However, even though the signatures are not seen clearly by looking at the trends, the continuous disturbance can be detected via the values of some parameters. IMF Bt does not indicate anything significant since it was already at around 20 nT before the storm started. IMF Bz decreases around -20 nT during the main phase and continues to stay at that level until the very late hours of the recovery phase. Dynamic pressure also does not indicate any signature and it was around 0.5×10^{-5} nPa at its maximum during the main phase. Ion density shows the exact same trend as the dynamic pressure and the values of the ion density is around 2x10^{-5} #/m^3. Both the dynamic pressure and ion density values are expected for this level of the geomagnetic storm. Velocity shows a different trend due to its nature. It starts at around 450 km/s at the beginning of the storm and continues to decrease slowly until the very late hours of the recovery phase where exactly the same time as the IMF Bz starts to increase and fluctuate.

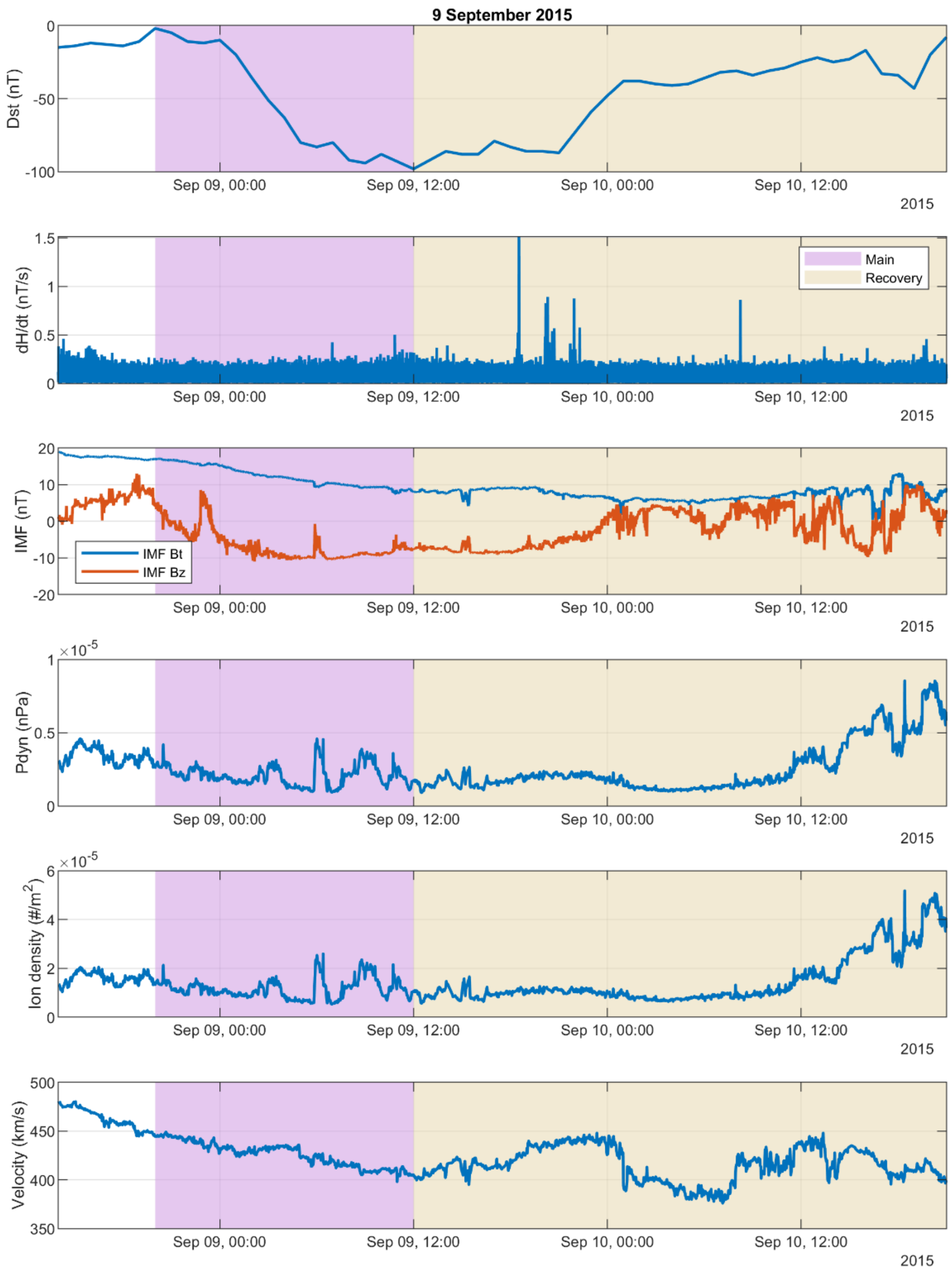

Figure 4.19 : Time series of Dst, dH/dt, IMF Bt and Bz, Pdyn, ion density, and velocity for 9 September 2015 storm.

In the Figure 4.19, the time series of geomagnetic indices Dst and AE, the ionospheric electron density on quiet and active days, and the difference between them are seen for the entire storm period. The quiet day period chosen for this case is 27-29 October 2015 is chosen. In this case, the storm has a negative effect on the electron density which means that the electron density decreases during the storm. The difference reaches -9.5x10^5 #/cc on 9 September at 06:36 UTC which is 09:36 LT. The effect can be seen when the Dst approaches its minimum around 04:00 UTC and aligns well with Dst. The same negative effect can be seen the following day as well, yet not in the same strength.

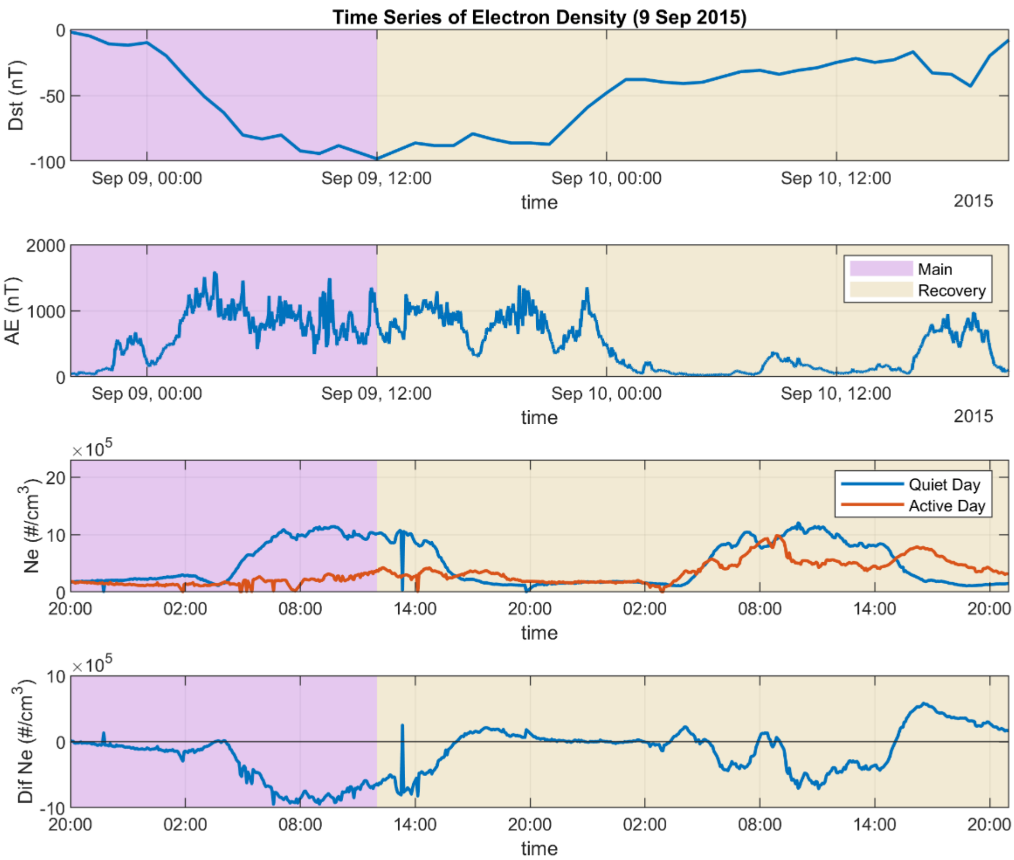

Figure 4.20 : Time series of Dst, AE, electron density, and electron density difference for 9 September 2015 storm.

In the Figure 4.20, the time series of Dst, dH/dt, IMF Bt and Bz, dynamic pressure, and electron density differences are seen. When all of the parameters are considered together with this figure, it is clear that the cause-and-effect relationships are not as clear as in the other cases in this study. The solar wind parameters do not show any alignment with either dH/dt not electron density difference. The only interesting point is the alignment with the dH/dt peak on 10 September at 08:14 UTC and the increase in electron density difference at the same time. This is unexpected and the reason behind is unclear even if there is a relationship between them. The first reason is that while mostly there is the negative effect on ionospheric electron density throughout the storm, around 08:14 UTC, there is a positive effect, thus the electron density

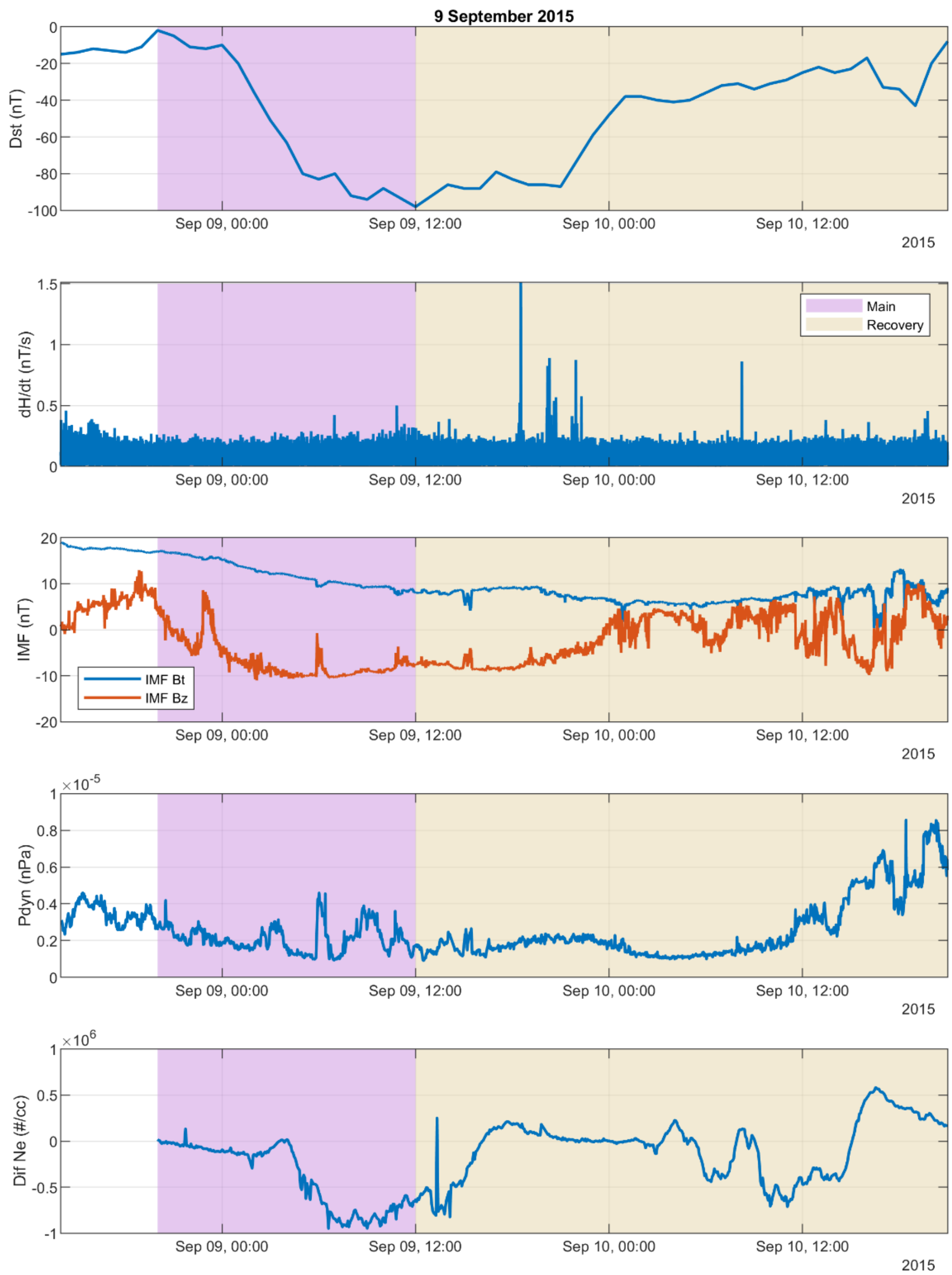

Figure 4.21 : Time series of Dst, dH/dt, IMF Bt and Bz, Pdyn, and electron density difference for 9 September 2015 storm.

increases at that point, and shows a different behavior than the rest of the storm. The second reason is while there are no signatures in the solar wind parameter and Dst, there is a change in AE at that time. Thus, there might be an effect in the ionospheric current due to auroral electrojets, yet it would be interesting to see a clear peak in the ground level dH/dt caused by an electrojet. Further analyses are required to be able to determine the reason behind these signatures.

5. STATISTICAL ANALYSIS AND RESULTS

The statistical analysis of the study consists of two parts as histograms and correlations for 36 cases. Histograms for each parameter have been made in order to determine the distribution of the parameters during geomagnetic storms. In total there are 27 histograms which 4 of them belongs to the geomagnetic indices. The rest of the histograms show the distribution of 23 parameters over mid-latitudes. The correlation part aims to show the linear correlation between physically meaningful pairs. In total, 72 pairs have been analyzed.

5.1 Histograms

In this part, 28 histograms have been formed to see the general distribution of parameters. The histograms of the parameters will be given in four sections which are geomagnetic indices, parameters of the geomagnetic field, ionospheric electron density, electric field, and solar wind.

5.1.1 Geomagnetic indices

The reason behind checking the distributions of the geomagnetic indices is to have an insight on the strengths is the geomagnetic storms that have been selected in this study. The chosen indices are Dst, AE, and Kp. The minimum Dst is used to determine the strength of the storm, yet in this study, the strength of the sudden commencement is also considered which means other than the minimum Dst, the maximum Dst value is also included. Thus, the selected parameters are minimum Dst, maximum Dst, maximum AE, and maximum Kp throughout each 36 storms.

In the Figure 5.1, the histograms of all four indices are seen. The top left panel shows the distribution of minimum Dst values. The distribution is left-skewed which means negative-skewed. The mean is -76.5 nT, the median is -68 nT, and the mode is -59 nT. In approximately 72% of the cases, the minimum Dst is between -50 and -100 nT. In only one of the cases, the minimum Dst is lower than -150 nT which is the St. Patrick storm 2015 where the minimum Dst was -222 nT. Thus, the expected minimum Dst value for a geomagnetic storm is greater than -150 nT most of the time.

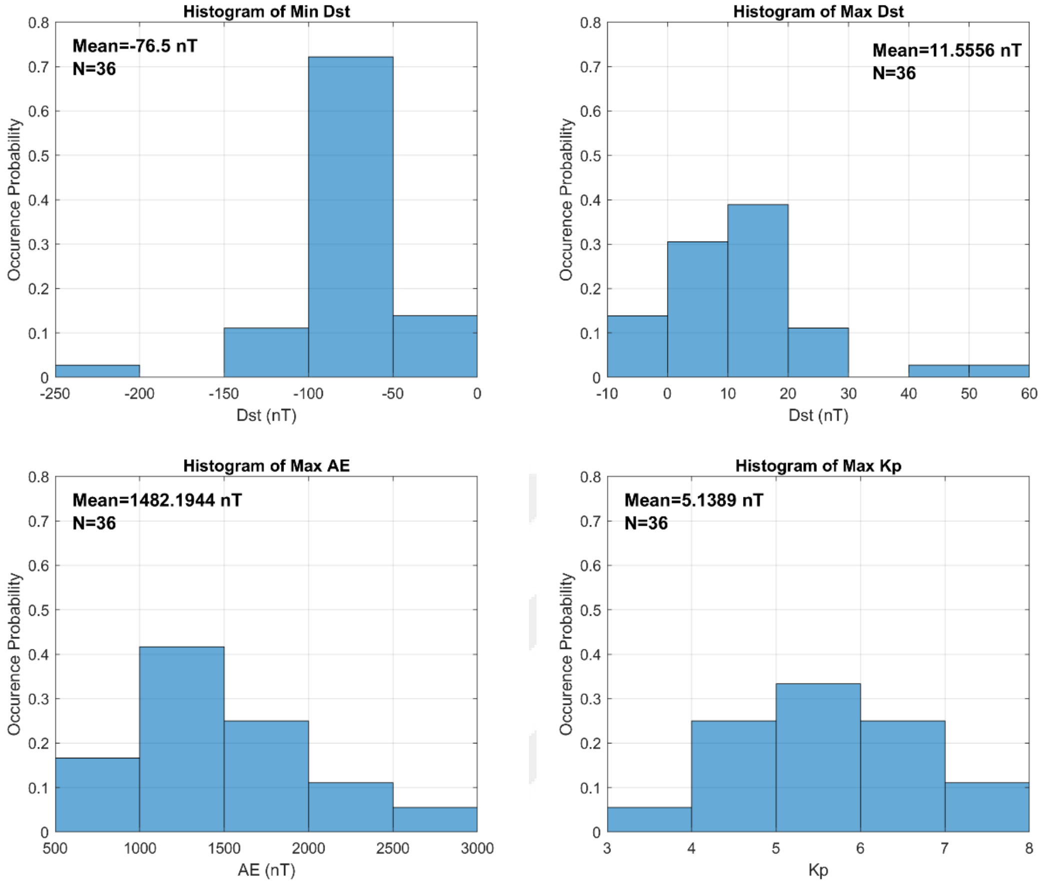

Figure 5.1 : Histograms of minimum Dst, maximum Dst, maximum AE, and maximum Kp.

The maximum Dst histogram can be seen in the top right panel which shows a right-skewed distribution. The mean and the median are 11.5 nT, and the mode is close to them which is 12 nT. This suggests an almost normal distribution, yet it is left-skewed. Based on the histogram, it can be said that in 79% of the cases the maximum Dst value is positive, thus sudden commencement exists. In 68% of the cases, the maximum Dst is between 0 and 20 nT. In only two cases the maximum Dst is greater than 30 nT.

The bottom left panel shows the maximum AE distribution. The mean is 1482 nT, the median is 1283 nT, and there is no mode in this set of data. The distribution is right-skewed. In 41% of the cases, the maximum AE value is between 1000 and 1500 nT. The greatest AE value is 2083 nT, and in only two of the cases, the maximum AE value is greater than 2500 nT.

The last index maximum Kp is at the bottom right panel. The mean, median, and mode of the maximum Kp are all the same which is 5. The Kp threshold for the geomagnetic storm is also 5. The maximum Kp has almost an ideal normal distribution. The criteria to choose the geomagnetically disturbed days was based on the Dst index in this study. Thus, in some of the cases, maximum Kp values are less than 5, yet in 70% of the cases, maximum Kp level is greater than 5. In only one case, the maximum Kp level was 8.

5.1.2 Geomagnetic field parameters

The main parameter considered in this study for the geomagnetic field is the time derivative of the horizontal geomagnetic field (dH/dt). Thus, in this part, the maximum dH/dt and related parameters have been considered. Additionally, the duration of the storm, each phase (initial, main, and recovery), and maximum dH/dt are included in the statistics. Finally, the maximum dH/dt in each phase of the storm has been analyzed in order to determine in which phase of the storm the maximum dH/dt is seen.

Even though the maximum dH/dt of each case is considered, the timing has also been investigated. The maximum dH/dt around minimum Dst, and maximum Dst is included, as well as the Dst value in the hour of maximum dH/dt is included.

In the Figure 5.2, the histograms of mentioned parameters can be seen. On the top left panel, the histogram of the maximum dH/dt throughout the storm is seen. The mean of the distribution is 1.31 nT/s, the median is 0.81 nT/s, and there is no mode. The threshold for GIC might be accepted as 1 nT/s based on the study done for Finnish power systems (Viljanen et al., 2001b). Based on this threshold, approximately in 40% of the cases the maximum dH/dt is greater than 1 nT/s. Although, it should be considered that the 1 nT/s threshold is for high latitudes, thus, another threshold would be more accurate in mid-latitudes. According to this histogram and this reference threshold, it can be said that the possibility of the occurrence of GIC is 40% during a geomagnetic storm. The maximum dH/dt among 36 cases is 4.76 nT/s which belongs to 6 July 2013. In only 3 of the cases, the maximum dH/dt is greater than 3 nT/s.

On the top right panel, the histogram of the maximum dH/dt around the minimum Dst for 36 cases is seen. The mean is 0.33 nT/s, the median is 0.31 nT/s, and there is no mode. The maximum dH/dt value in this set is 0.66 nT/s, and in only 3 cases the dH/dt is greater than 0.6 nT/s. According to this histogram, it can be said that the maximum dH/dt during a storm is not seen when Dst reaches its minimum or 1 hour around it.

On the bottom left panel, the histogram of the maximum dH/dt around maximum Dst which means 1 hour around sudden commencement is seen for 36 cases. The mean is 0.38 nT/s, the median is 0.30 nT/s, and the mode is 0.28 nT/s. In only one case the maximum dH/dt around sudden commencement is greater than 1 nT/s, and that case is St. Patrick Storm 2015. Based on this histogram, it can be concluded that the possibility of the maximum dH/dt of a storm to happen around sudden commencement is highly low.

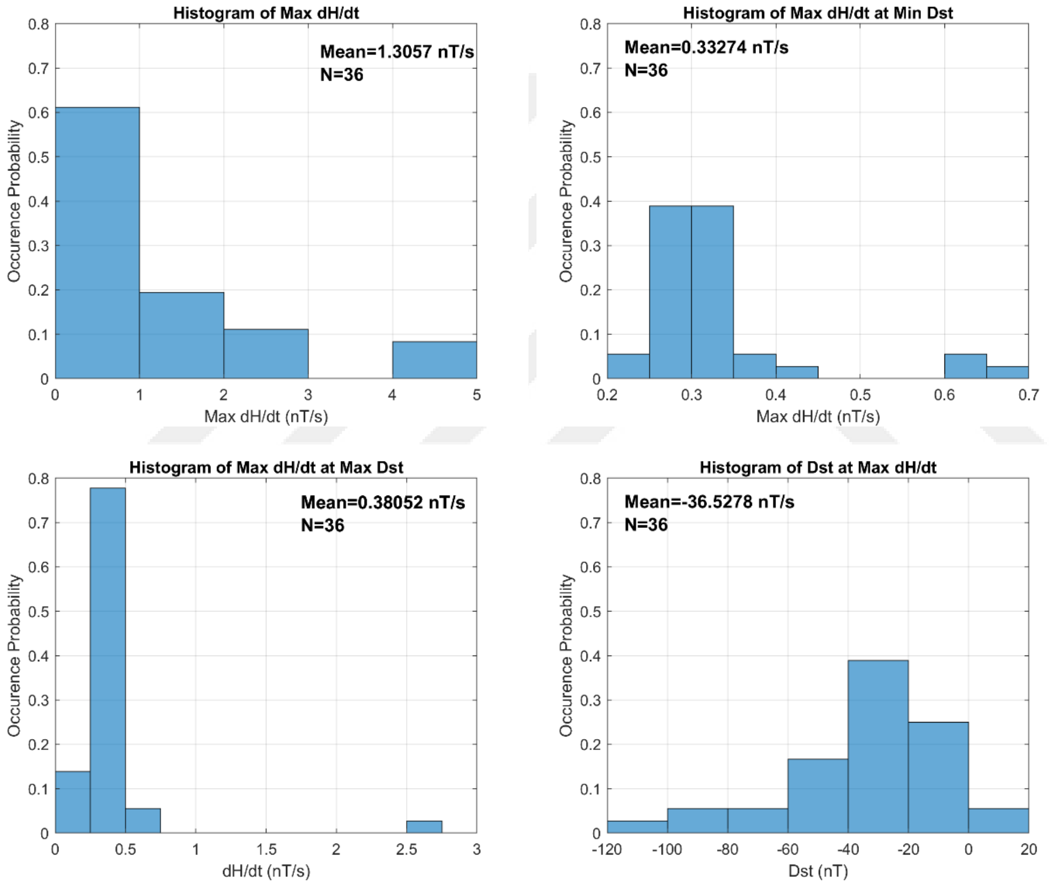

Figure 5.2 : Histograms of maximum dH/dt, maximum dH/dt at minimum Dst, dH/dt at maximum Dst, and Dst at maximum dH/dt.

On the bottom right panel, the histogram of the Dst values in the hour of maximum dH/dt happens for 36 cases is seen. The mean is -36.53 nT, the median is 36 nT, and the mode is -39 nT. The distribution is left-skewed. In 39% of the cases, the Dst value is between -40 and -20 nT. This is followed by a 25% of the interval between -20 and 0 nT. Based on this information it can be said that the maximum dH/dt are tend to be seen mostly when the Dst is between -60 and 0 nT which can be anytime based on the strength of the storm. For example, it can be during the beginning of the main phase or the end of the recovery phase of a storm which has a -100 nT minimum Dst value. This analysis is not enough to conclude a point by its own.

The Figure 5.3 consists of the durations of the storms. The top left panel shows the durations of each storm. The mean is 71.74 hours, the median is 65.25 hours, and the mode is 86 hours. The minimum duration is 18 hours, while the maximum is 236 hours which is approximately 10 days. Almost 90% of the storms last less than 150 hours which is approximately 6 days.

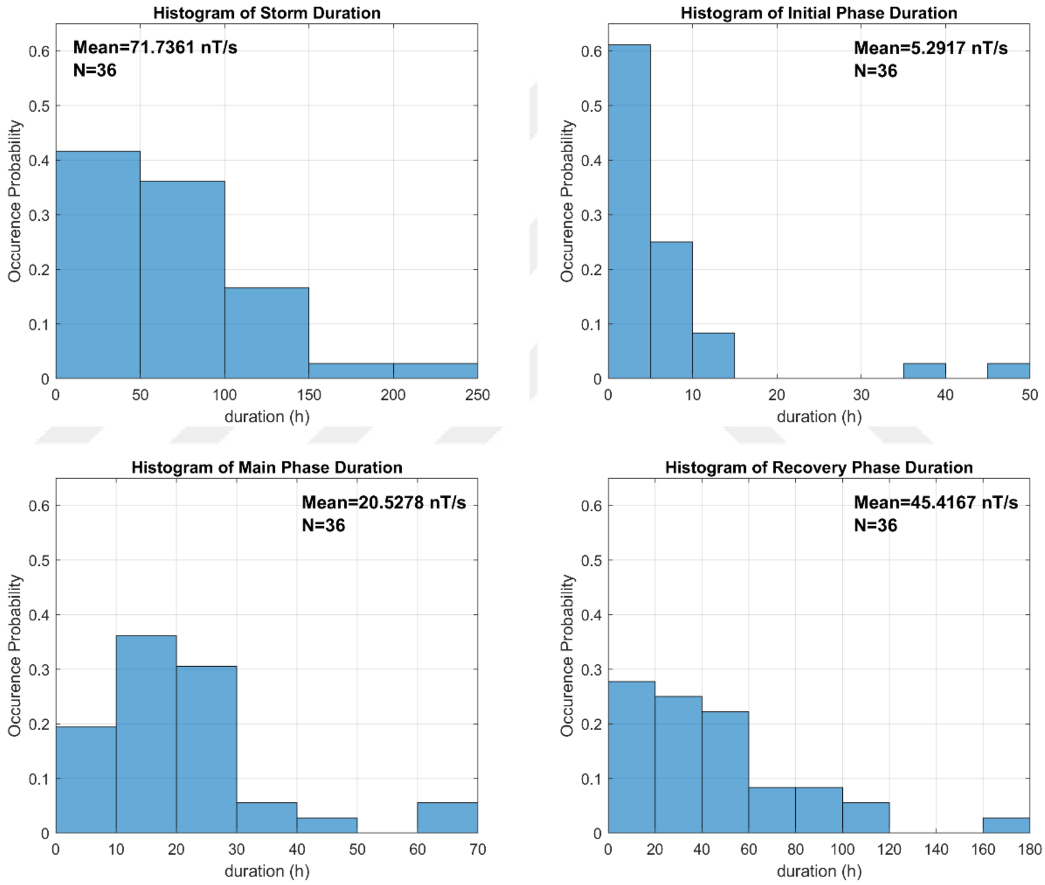

Figure 5.3 : Histograms of durations of storms, initial phases, main phases, and recovery phases.

The other panels show the distributions of the duration of each phase of the storms. The top right panel shows the duration of the initial phase for each case. The mean is 5.29 hours, the median is 1 hour, and the mode is 0. The reason behind that the mode is 0 is that not every storm has sudden commencement, or if there is one it is not distinctive. Thus, the duration of the initial phase of the storms varies a lot and is relatively shorter than other phases. While in 60% of the cases the initial phase lasts less than 5 hours, in only two of the cases the initial phase lasts more than 15 hours.

On the bottom left panel, the histogram of the main phase of each case is seen. The mean is 20.53 hours, the median is 18.5 hours, and there is no mode. The maximum main phase duration is 64 hours. Approximately in 66% of the cases, the main phase lasts between 10 and 30 hours. In only 2 cases the main phase lasts more than 60 hours which makes 5% of the cases.

The bottom right panel shows the histogram of the duration of the recovery phase for 36 cases. The mean is 45.42 hours which is almost 2 days, the median is 33.5 hours, and the mode is 12. The minimum recovery phase duration is 5 hours and the maximum duration is 180 hours which belongs to St. Patrick storm 2015. In almost 95% of the cases, the recovery phase lasts less than 120 hours which is 5 days, and in 75% of the cases, the duration is less than 60 hours which is 2.5 days.

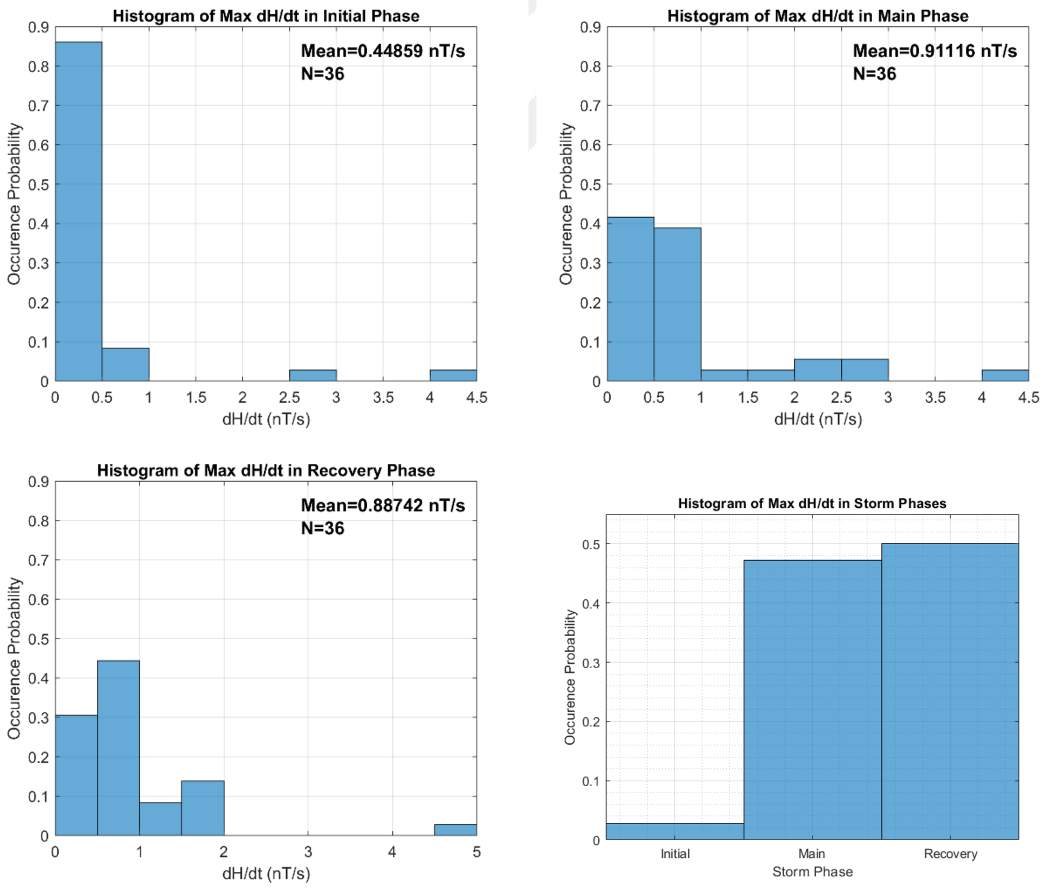

Figure 5.4 : Histograms of maximum dH/dt in initial, main, and recovery phases, and phases when the maximum dH/dt is seen.

In the Figure 5.4, the first three panel shows the maximum dH/dt value in each storm phase, and in the last panel, the histogram of the phases where the maximum dH/dt of the storm is seen.

The top left panel shows the maximum dH/dt in the initial phase for 36 cases. The mean is 0.45 nT/s, the median is 0.29 nT/s, and there is no mode. In almost 86% of the cases, the maximum dH/dt is below 0.5 nT/s, and only in two extreme cases, the maximum dH/dt is greater than 1 nT/s. The greatest dH/dt value in the initial phase in 36 cases is 4.14 nT/s.

The top right panel shows the maximum dH/dt in the main phase for each case. The mean is 0.91 nT/s, the median is 0.56 nT/s, and there is no mode. In 81% of the cases, the maximum dH/dt is less than 1 nT/s, and 39% of them is between 0.5 and 1 nT/s. The maximum dH/dt in the main phase in 36 cases is 4.22 nT/s.

On the bottom left panel, the maximum dH/dt value in the recovery phase for each storm is seen. The mean is 0.89 nT/s, the median is 0.66 nT/s, and there is no mode. In 74% of the cases, the maximum dH/dt is below 1 nT/s. In 44% of the cases, the maximum dH/dt is between 0.5 and 1 nT/s second. This ratio is greater than in the case of the initial and main phases. The maximum dH/dt is greater than 1 nT/s in 9 cases among 36. The only outlier is one case with a 4.76 nT/s dH/dt value.

On the bottom left panel, the histogram of the phases where the maximum dH/dt of the storm is seen. The purpose of this analysis is to determine in which phase of the storm the possibility of seeing the highest dH/dt is higher and understand the physical meaning behind this. This is one of the most surprising outcomes of this study since the maximum dH/dt is expected to be seen during the initial phase due to the sudden commencement and equatorial ring current. Surprisingly, in half of the cases as 18 of them, the maximum dH/dt was observed in the recovery phase, and in 17 of them, it is observed during the main phase. In only one of the cases, the maximum dH/dt is observed during the initial phase. This raises questions about the triggering mechanism behind the sudden changes in the geomagnetic field.

5.1.3 Ionospheric electron density differences

The ionospheric electron density part of this section involves four parameters. The difference between the active and quiet day maximum electron densities is the main parameter here. Since the effect can be negative or positive, the first parameter is the maximum absolute difference for each storm. This is followed by the average of absolute difference, and the maximum negative and positive differences.

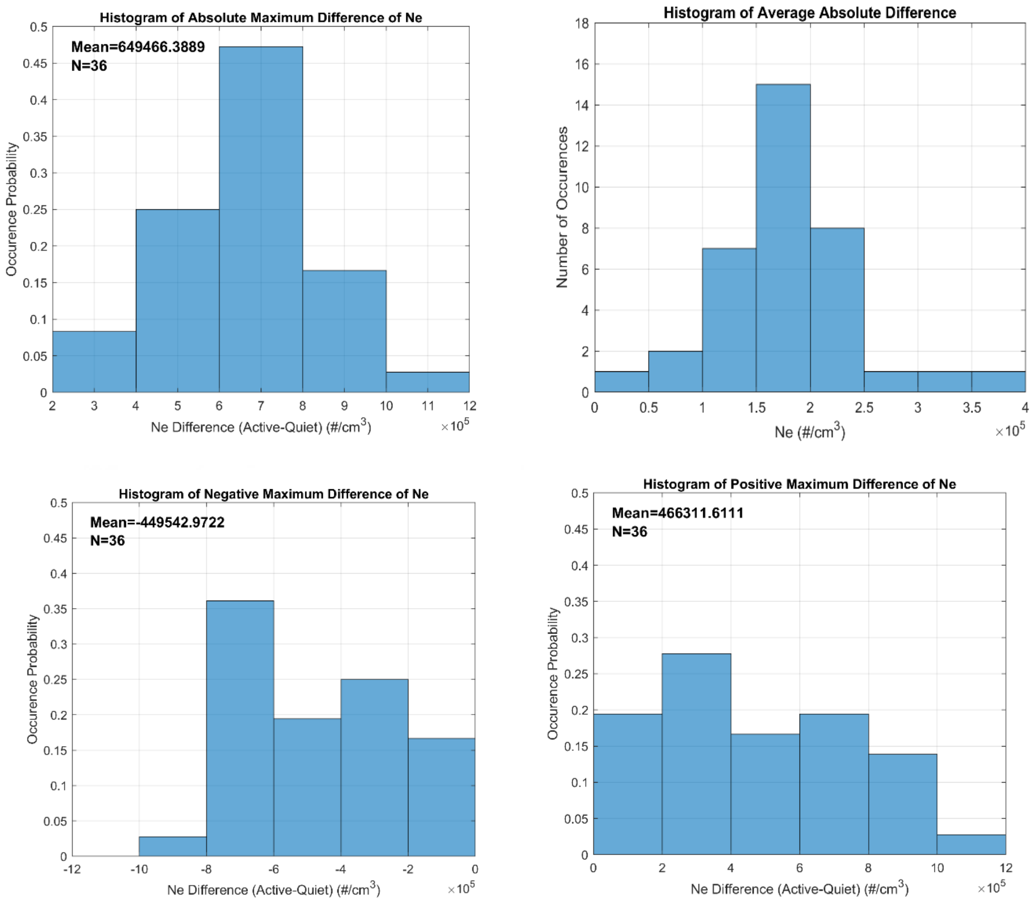

Figure 5.5 : Histograms of absolute maximum difference of electron density, average absolute difference of electron density, negative maximum difference of electron density, positive maximum difference of electron density.

The panel on the top left in Figure 5.5 shows the histogram of the maximum absolute difference for each storm. The mean is $6.5x10^5$ #/cc, the median is $6.6x10^5$ #/cc, and there is no mode. The distribution of the absolute differences is almost normal. The distribution varies between $2x10^5$ and $12x10^5$ #/cc. In 42% of the cases, the maximum absolute difference is between $6x10^5$ and $8x10^5$ #/cc.

The panel on the top right illustrates the distribution of the average absolute differences for 36 cases. This histogram aims to estimate the average electron density difference values during geomagnetic disturbances. The mean and the median are the same as $1.8x10^5$ #/cc, and there is no mode. The distribution is close to normal distribution. In 83% of the cases, the average difference is between $1x10^5$ and $2.5x10^5$ #/cc.

The panel on the bottom left shows the distribution of negative maximum difference which represents the situation where the electron density is lower on an active day. The mean is -4.5x10^5 #/cc, the median is -4.6x10^5 #/cc, and there is no mode. In the majority of the cases, the negative maximum difference is greater than -8x10^5 #/cc. The is only one case in which the maximum negative difference is lower than -8x10^5 #/cc, and that is -8.03 #/cc which means that the expected maximum negative difference is -8x10^5 #/cc.

The panel on the bottom left shows the distribution of positive maximum difference which represents the situation where the electron density is greater on the active day. The mean is 4.6x10^5 #/cc, the median is 4.2x10^5 #/cc, and there is no mean. The distribution is right-skewed. In 30% of the cases, the positive maximum electron density difference is between 2x10^5 and 4x10^5 #/cc. There is only one case where the positive maximum electron difference is greater than 1x10^6 #/cc, and that maximum is 11.3x10^5 #/cc.

Additionally, when the histograms for the positive and negative electron density differences are compared, it can be said that the possibility of seeing a greater difference between active and quiet days is higher when the effect is negative.

5.1.4 Electric field

In this section, there are only two parameters and due to the limitations of measurements, there are 10 cases instead of 36. The parameters analyzed here are the maximum northward and eastward components of the electric field, E_x and E_y.

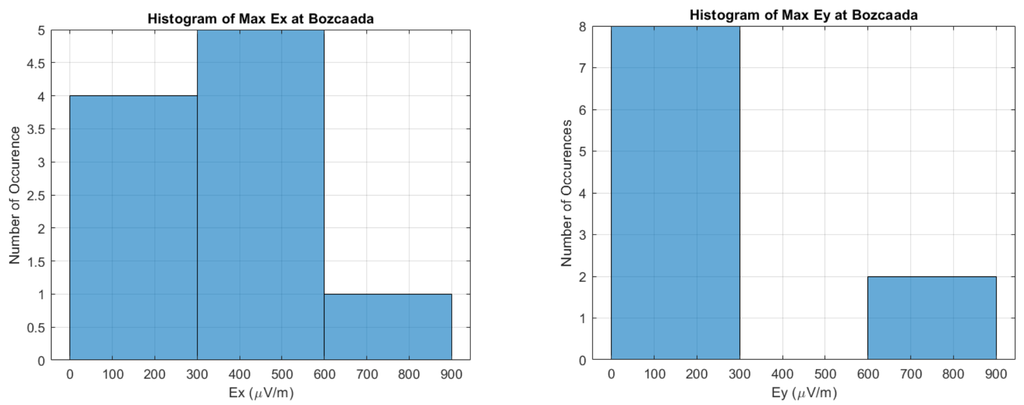

Figure 5.6 : Histograms of maximum Ex and Ey at Bozcaada.

In the Figure 5.6, the panel on the left shows the distribution of the maximum northward electric field for 10 cases. The mean is 338 μV/m, the median is 317 μV/m, and there is no mode. In 60% of the storms, the E_x varies between 200 and 400 μV/m. In only one case which means 10% of the storms, the maximum E_x is greater than 500 μV/m.

On the right panel, the distribution of the maximum eastward electric field for 10 cases is seen which is an interesting distribution since it is difficult to determine if the values between 600 and 700 μV/m are outliers or not with only 10 cases. The mean is 254 μV/m, the median is 187 μV/m, and there is no mode. In 80% of the cases, the maximum E_y is lower than 300 μV/m, and the rest is between 600 and 700 μV/m.

5.1.5 Solar wind parameters

In this part of the statistical analysis, the distributions of maximums of 5 solar wind parameters have been investigated. The reason behind this analysis is to have an insight on what strengths of solar storms have been considered throughout this study. The parameters which have been chosen are ion density, velocity, total IMF, southward IMF, and dynamic pressure.

In the Figure 5.7, on the first panel, the distribution of maximum ion densities for 36 cases is seen. The mean is $3.2\text{x}10^{-5}$ #/m^3, the median is $2.7\text{x}10^{-5}$ #/m^3, and there is no mode. The distribution is right-skewed. The maximum ion densities vary between $1\text{x}10^{-5}$ and $7.2\text{x}10^{-5}$ #/m^3. In 58% of the cases, the ion density is below $3\text{x}10^{-5}$ #/m^3.

On the second panel, the distribution of maximum solar wind velocity for 36 cases is seen. The mean is 515 km/h, the median is 499 km/h, and there is no mode. The distribution is right-skewed. The solar wind velocity varies between 320 and 780 km/h. In 61% of the cases, the velocity is between 400 and 600 km/h.

The next panel shows the distribution of the maximum total IMF for each case. The mean is 18.6 nT, the median is 16.5 nT, and there is no mode. The strength of IMF B_t varies between 9.8 and 44.7 nT. In 64% of the cases, the IMF B_t is between 10 and 20 nT. There is only one case where the IMF B_t is greater than 40 nT.

On the next panel, the distribution of strength of southward IMF for each case is seen. The mean is -15.4 nT, the median is -13.9 nT, and there is no mode. The distribution is left-skewed by its nature. The southward IMF varies between -29.5 and -8.1 nT. In half of the cases, the IMF B_z is between -15 and -10 nT. The other intervals are almost equally distributed.

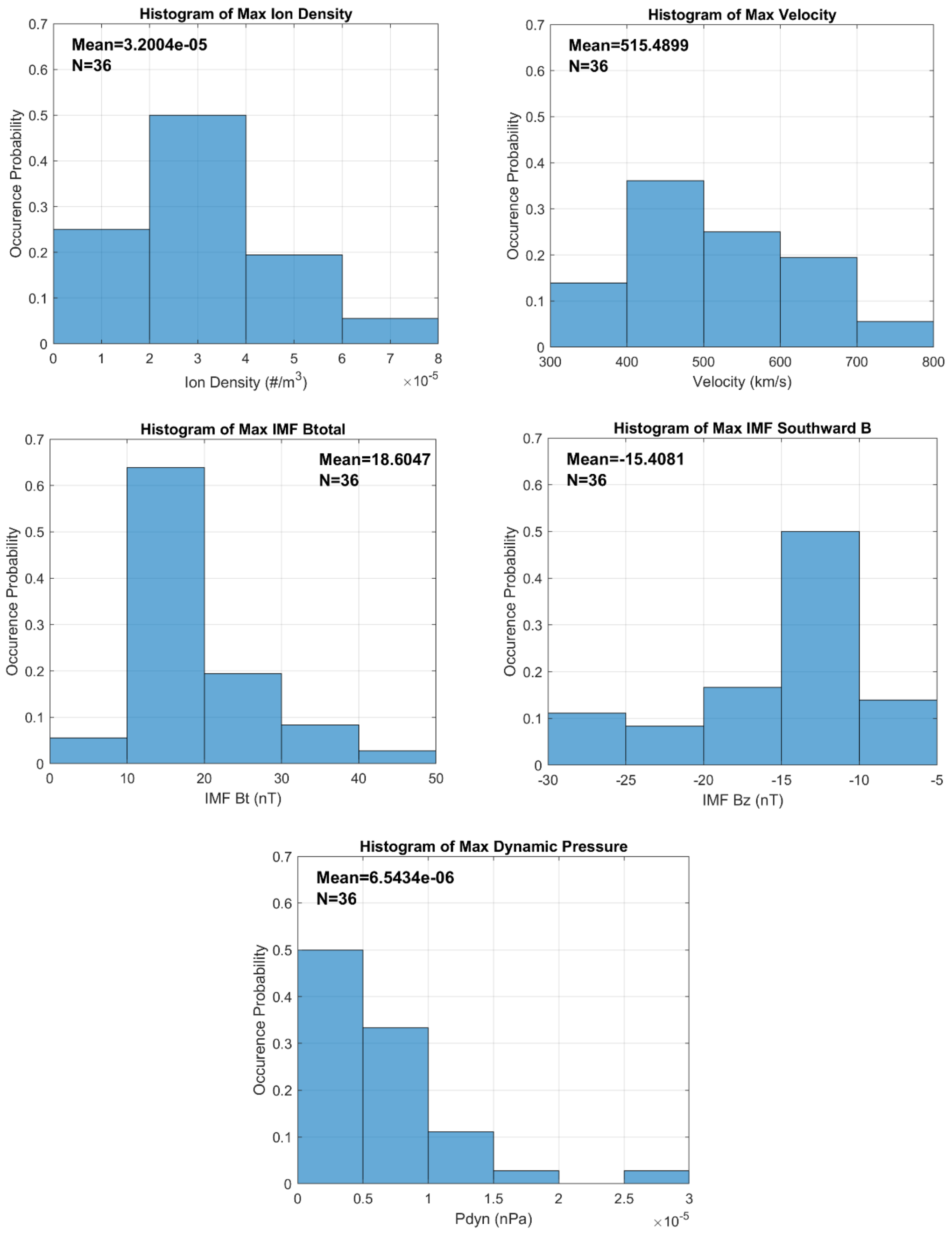

Figure 5.7 : Histograms of maximum solar wind ion density, velocity, IMF Bt and Bz, and Pdyn.

On the last panel, the distribution of maximum dynamic pressure for each case is seen. The mean is 6.5×10^{-6} nPa, the median is 5.2×10^{-6} nPa, and there is no mode. The distribution is highly right-skewed. In 36 cases, the dynamic pressure changes between 1.7×10^{-6} and 2.8×10^{-5} nPa. In half of the cases the maximum dynamic pressure is less than $5x10^{-6}$ nPa, and in 83% of the cases it is less than $1x10^{-5}$ nPa. There are only two cases where the dynamic pressure is greater than $1.5x10^{-5}$ nPa.

5.2 Linear Correlations

In this part of the study 69 physically meaningful pairs have been chosen to answer specific questions toward understanding the linear relationships, thus, the linear correlations between them have been determined by using scatter plots and Pearson correlation, and applying two tailed Student's t-test. The Pearson correlation coefficient is 'r', and the outcome of the t-test is evaluated for 95% significance level. Based on the t-test results, only 22 out of the 69 parameters are considered as statistically significant. For the r values less than 0.36 are considered at statistically insignificant. For the analysis with 36 samples, the critical t-score is 2.032, and for 10 samples it is 2.306.

5.2.1 Geomagnetic indices and dH/dt

In this part of the correlation analysis, maximum dH/dt of the storm and its relation with geomagnetic indices, and the timing of it are considered. It will be explained in two sections as its dependence to geomagnetic indices, and the timing of it.

5.2.1.1 Geomagnetic indices and maximum dH/dt

In this part, the linear correlation between geomagnetic indices and maximum dH/dt is analyzed. The purpose of these analyses is to gain an estimation of the dependence of the magnitude of the dH/dt on the storm strengths, and determine which index is more reliable to estimate the effects. The geomagnetic indices chosen are minimum Dst, maximum Dst (to include sudden commencement effect), maximum Kp, and maximum AE. Among the correlation coefficients of maximum dH/dt with geomagnetic indices, while minimum Dst, maximum AE and Kp are statistically significant, maximum Dst is statistically insignificant with a correlation coefficient of 0.21 which means that there is no linear relationship between the strength of sudden commencement and the maximum dH/dt of a storm.

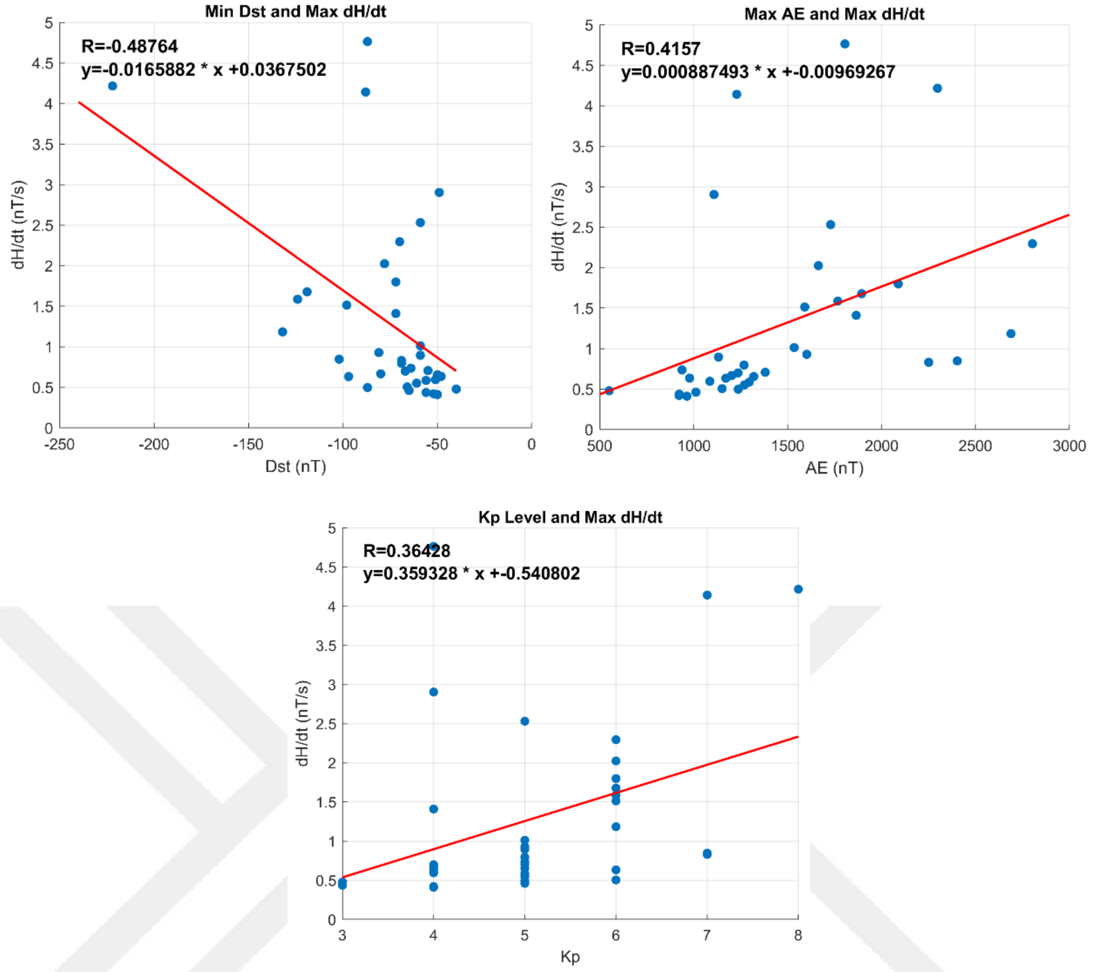

Figure 5.8 : Scatter plots of minimum Dst and maximum dH/dt, maximum AE and maximum dH/dt, maximum Kp and maximum dH/dt.

In the Figure 5.8, on the first panel, the linear relationship between the minimum Dst and the maximum dH/dt of each storm is seen. The correlation coefficients, t-values, p-values and the acceptance of the null hypothesis is seen in the Table 5.1. The Pearson correlation coefficient for minimum Dst and maximum dH/dt pair is -0.48 which is the highest among three significant indices. On the second panel, the maximum AE can be seen with a correlation coefficient 0.41. The last one is with maximum Kp level, and the coefficient is 0.36 which is the significance limit for this analysis.

Table 5.1 : Pearson correlation coefficients, t-values, p-values, and acceptence of H0 for geomagnetic indices and maximum dH/dt.

		r	t-value	p-value	H0
Min Dst	Max dH/dt	-0,4876	-3,2569	0,002-0,005	Reject
Max Dst (SC)	Max dH/dt	0,2178	1,301	<0,20	Accept
Max AE	Max dH/dt	0,4157	2,6651	0,01-0,02	Reject
Max Kp	Max dH/dt	0,3643	2,2808	0,02-0,05	Reject

Even though, none of these correlation coefficients indicate a strong relationship, coefficients of the minimum Dst and AE are promising. It can be concluded that the maximum dH/dt of a storm is mostly affected by minimum Dst, and followed by AE. This means that at mid-latitudes, the response to equatorial ring current is better than to auroral electrojets, and minimum Dst is the best indicator among these indices for mid-latitudes.

5.2.1.2 Dst and timing of dH/dt

The aim of the linear correlations is to determine how closely related the strength of the dH/dt is with the timing of important points during the storms such as maximum dH/dt, maximum or minimum Dst. Three analysis have been made to understand the timing of the maximum dH/dt, and only one of them was statistically significant. The correlation coefficients, t-values, p-values and the acceptance of the null hypothesis is seen in the table 5.2.

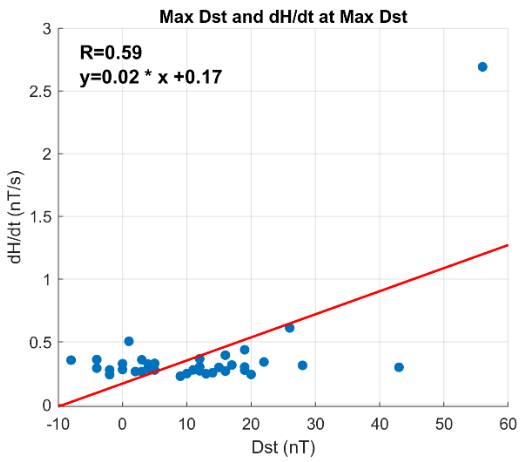

Figure 5.9 : Scatter plot of maximum Dst and dH/dt at maximum Dst.

The correlation coefficient between the minimum Dst value and the maximum dH/dt value at the time interval where the minimum Dst is seen has been calculated and the outcome is -0.07 which is statistically insignificant. Thus, it can be said that the strength of the storm does not affect the maximum dH/dt value during the most intense hour of the storm. The other insignificant correlation is between the Dst value where the maximum dH/dt of the storm occurs and the maximum dH/dt which is -0.32. The only significant coefficient among these three pairs is the one between maximum Dst and the maximum dH/dt in the interval during maximum Dst which is -0.59, yet the scatter plot for this pair shows that this coefficient might not be trusted due to the extreme point. Thus, the relationship between the geomagnetic indices and the timing of the maximum dH/dt is not clear based on these analyses.

Table 5.2 : Pearson correlation coefficients, t-values, p-values, and acceptence of H0 for Dst and timing of dH/dt.

		r	t-value	p-value	H0
Min Dst	dH/dt at min Dst	-0,0732	-0,4281	<0,20	Accept
Max Dst (SC)	dH/dt at max Dst	0,5939	4,3039	>0,001	Reject
Dst at max dH/dt	Max dH/dt	-0,3267	-2,0156	0,10-0,05	Accept

5.2.2 Geomagnetic indices and durations

This part of the study contains the relationship between the geomagnetic indices and the durations of the storms, and duration of each phase. The aim of this part is to understand which geomagnetic indices and mechanism directly affects the storm durations and its phases.

5.2.2.1 Geomagnetic indices and storm durations

In this section, the linear correlations between the duration of each storm and chosen 4 geomagnetic indices. All of the coefficients are statistically significant in 95% significance level based on the t-test results. The correlation coefficients, t-values, p-values and the acceptance of the null hypothesis is seen in the Table 5.3.

Table 5.3 : Pearson correlation coefficients, t-values, p-values, and acceptence of H0 for geomagnetic indices and storm durations.

		r	t-value	p-value	H0
Min Dst	Storm duration	-0,687	-5,5122	>0,001	Reject
Max Dst (SC)	Storm duration	0,4104	2,6242	0,01-0,02	Reject
Max AE	Storm duration	0,4164	2,6709	0,01-0,02	Reject
Max Kp	Storm duration	0,4496	2,9351	0,005-0,01	Reject

In the Figure 5.10, the scatter plots of these relationships are seen. The Pearson correlation coefficients between the duration and the geomagnetic indices are found as -0.69, 0.41, 0.42, and 0.45 for minimum Dst, maximum Dst, maximum AE, and maximum Kp, respectively. Based on these results, it can be said that the duration of a storm indeed depends on the strength of the storm at some level. The best indicator between the four parameters seems like minimum Dst, yet when looking at the scatter plot it can be seen that there is one outlier that might have affected the result. That outlier is St. Patrick storm 2015 with a -222 nT Dst value. In order to be able to make a more definitive decision, the outliers should be removed.

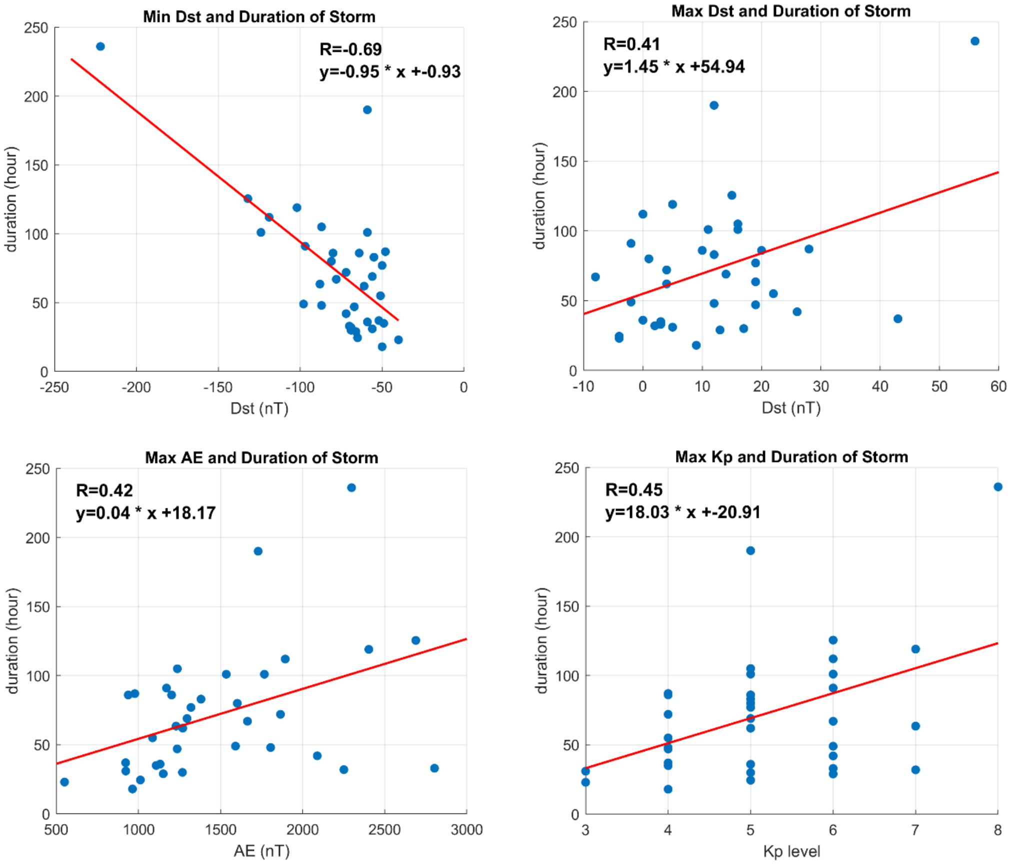

Figure 5.10 : Scatter plots between storm duration and minimum Dst, maximum Dst, maximum AE, maximum Kp.

5.2.2.2 Geomagnetic indices and initial phase durations

In this section, a similar process has been followed for the initial phase of the storm. The initial phase of the storm is more difficult to identify due to the lack of sudden commencement in some of the storms, yet it is investigated if the duration of the initial phase of a storm depends on the strength of the storm. The correlation coefficients, t-values, p-values and the acceptance of the null hypothesis is seen in the Table 5.4.

Table 5.4 : Pearson correlation coefficients, t-values, p-values, and acceptence of H0 for geomagnetic indices and initial phase durations.

		r	t-value	p-value	H0
Min Dst	Initial phase duration	-0,3224	-1,9857	0,05-0,10	Accept
Max Dst (SC)	Initial phase duration	0,6589	5,1082	>0,001	Reject
Max AE	Initial phase duration	0,0024	0,0141	<0,20	Accept
Max Kp	Initial phase duration	0,0578	0,3375	<0,20	Accept

The Pearson correlation coefficients for the duration of the initial phase and geomagnetic index pairs have been found as -0.32, 0.66, 0,002, and 0.06, for minimum Dst, maximum Dst, maximum AE, and maximum Kp, respectively. According to these coefficients, the only significant relationship is between maximum Dst and the initial phase duration. Based on the coefficients it can be said that the duration of the initial phase depends on the strength of the sudden commencement. While there are no relationships with minimum Dst, AE and Kp.

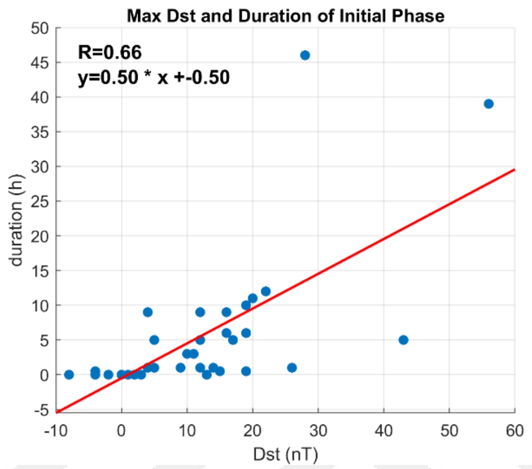

Figure 5.11 : Scatter plot for maximum Dst and duration of initial phase.

5.2.2.3 Geomagnetic indices and main phase durations

In this section, the linear relationship between the selected geomagnetic indices and the duration of the main phase of the storms has been investigated to understand if the duration of the main phase is affected by the strength of the storm. The Pearson correlation coefficients between the duration of the main phase and the geomagnetic indices are found as 0.11, -0.08, 0.11, and -0.04 for minimum Dst, maximum Dst, maximum AE, and maximum Kp, respectively. Thus, none of the pairs are considered as statistically significant, and it can be said that there is no relationship between the strength of the storm and the duration of the main phase. The correlation coefficients, t-values, p-values and the acceptance of the null hypothesis is seen in the Table 5.5.

Table 5.5 : Pearson correlation coefficients, t-values, p-values, and acceptence of H0 for geomagnetic indices and main phase durations.

		r	t-value	p-value	H0
Min Dst	Main phase duration	0,1133	0,665	<0,20	Accept
Max Dst (SC)	Main phase duration	-0,0759	-0,444	<0,20	Accept
Max AE	Main phase duration	0,1062	0,623	<0,20	Accept
Max Kp	Main phase duration	-0,038	-0,2215	<0,20	Accept

5.2.2.4 Geomagnetic indices and recovery phase durations

In this part, the relationship between the selected geomagnetic indices and the duration of the recovery phase of the 36 storms has been analyzed. The purpose of this analysis is to determine whether there is a dependence between the storm strength and the duration of the recovery phase, and which index show is the best indicator. The correlation coefficients, t-values, p-values and the acceptance of the null hypothesis is seen in the Table 5.6.

Table 5.6 : Pearson correlation coefficients, t-values, p-values, and acceptence of H0 for geomagnetic indices and recovery phase durations.

		r	t-value	p-value	H0
Min Dst	Recovery phase duration	-0,8015	-7,8151	>0,001	Reject
Max Dst (SC)	Recovery phase duration	0,3191	1,9634	0,05-0,1	Accept
Max AE	Recovery phase duration	0,444	2,8892	0,005-0,01	Reject
Max Kp	Recovery phase duration	0,535	3,6926	>0,001	Reject

The Pearson correlation coefficients between the duration of the recovery phase and the geomagnetic indices are found as -0.80, 0.32, 0.44, and 0.54 for minimum Dst, maximum Dst, maximum AE, and maximum Kp, respectively. Thus, the relationship between the recovery phase duration and the strength of the sudden commencement is statistically insignificant. Based on the coefficients and the scatter plots, it can be said that the duration of the recovery phase depends on the storm strength at some level, and the minimum Dst is the best indicator of it with the highest correlation coefficient of 0.8 which indicates a strong linear correlation.

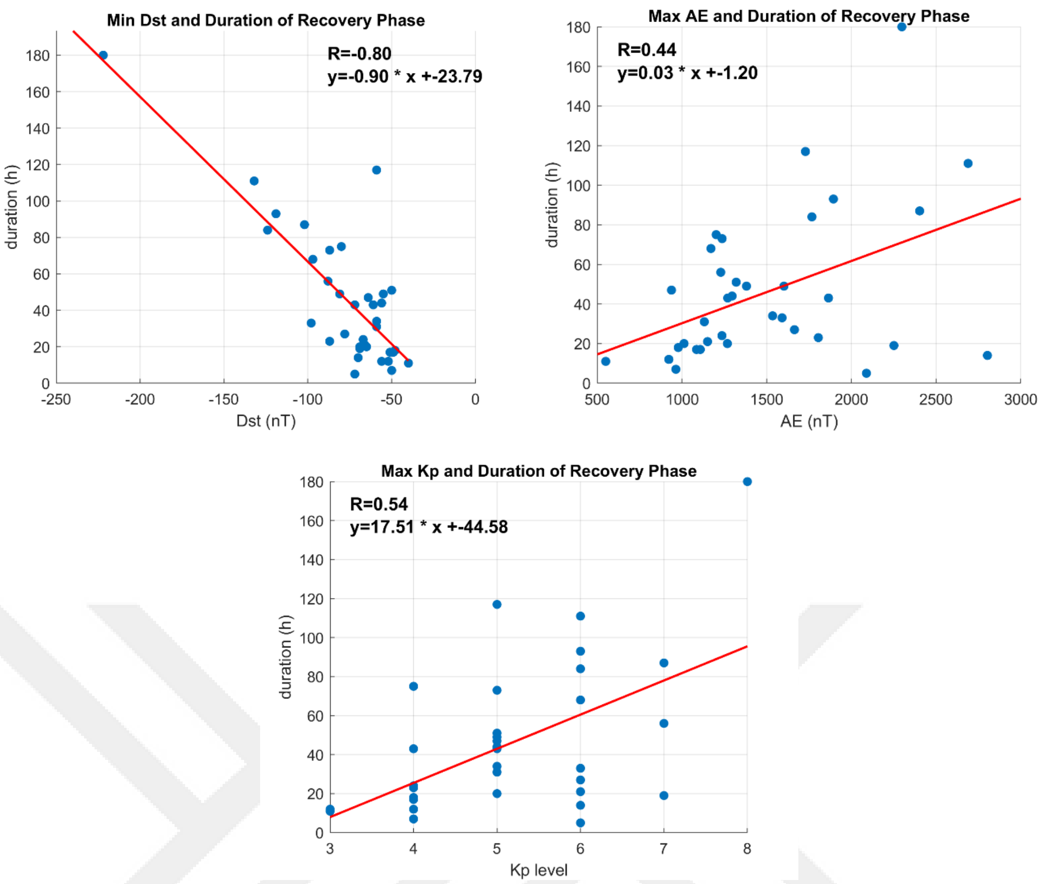

Figure 5.12 : Scatter plots of duration of recovery phase with minimum Dst, maximum AE, and maximum Kp.

5.2.3 Difference of ionospheric electron density

In this section, 30 pairs have been analyzed. Among these pairs, three main electron density difference parameters were used which are absolute maximum electron density difference, negative maximum electron density difference, and positive maximum electron density difference. The relationship of these parameters with 30 different parameters are analyzed. Geomagnetic indices Dst, AE and Kp, maximum dH/dt, and solar wind parameters ion density, velocity, total and southward IMF, and dynamic pressure are included in the analysis. Among 30 pairs, only one correlation coefficient is statistically significant which is the relationship between the absolute maximum electron density difference and minimum Dst as it can be seen in the Figure 5.13. The correlation coefficient is -0.45 which is not high enough to say that there is a direct relationship between the storm intensity and the electron density change in ionosphere.

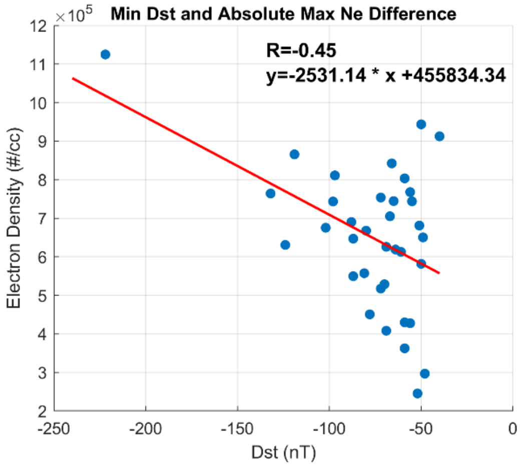

Figure 5.13 : Scatter plot of minimum Dst and absolute maximum electron density difference.

The correlation coefficients, t-values, p-values and the acceptance of the null hypothesis for the 30 pairs is seen in the Table 5.7. Based on this analysis, it can be said that the effect of the solar wind parameters and storm intensity on the ionospheric electron density cannot be seen directly with this kind of a method due to complex mechanisms which affect the ionosphere. Additionally, a direct relationship between the electron density and the geomagnetic field change cannot be found.

Table 5.7 : Pearson correlation coefficients, t-values, p-values, and acceptence of H0 for ionospheric electron density difference related pairs.

		r	t-value	p-value	H0
Min Dst	Absolute max electron density difference	-0,454	-2,9711	0,005-0,01	Reject
Max Dst (SC)	Absolute max electron density difference	0,0224	0,1307	<0,20	Accept
Max AE	Absolute max electron density difference	0,071	0,4151	<0,20	Accept
Max Kp	Absolute max electron density difference	0,2211	1,3218	0,10-0,20	Accept
Min Dst	Negative max electron density difference	0,2345	1,4066	0,10-0,20	Accept
Max Dst (SC)	Negative max electron density difference	0,1036	0,6076	<0,20	Accept
Max AE	Negative max electron density difference	-0,3336	-2,0633	0,02-0,05	Accept
Max Kp	Negative max electron density difference	-0,2164	-1,2922	<0,20	Accept
Min Dst	Positive max electron density difference	-0,3184	-1,9582	0,05-0,10	Accept
Max Dst (SC)	Positive max electron density difference	0,1276	0,75	<0,20	Accept

Table 5.7 (cont.) : Pearson correlation coefficients, t-values, p-values, and acceptence of H0 for ionospheric electron density difference related pairs.

		r	t-value	p-value	H0
Max AE	Positive max electron density difference	-0,0739	-0,4319	<0,20	Accept
Max Kp	Positive max electron density difference	0,1749	1,0358	<0,20	Accept
Max dH/dt	Absolute max electron density difference	0,174	1,0301	<0,20	Accept
Max dH/dt	Negative max electron density difference	-0,2809	-1,7068	0,05-0,10	Accept
Max dH/dt	Positive max electron density difference	-0,03	-0,175	<0,20	Accept
Max solar wind ion density	Absolute max electron density difference	-0,1397	-0,8227	<0,20	Accept
Max solar wind ion density	Negative max electron density difference	0,2291	1,3721	0,10-0,20	Accept
Max solar wind ion density	Positive max electron density difference	-0,016	-0,0936	<0,20	Accept
Max solar wind velocity	Absolute max electron density difference	0,138	0,8124	<0,20	Accept
Max solar wind velocity	Negative max electron density difference	0,0417	0,2435	<0,20	Accept
Max solar wind velocity	Positive max electron density difference	0,1928	1,1455	<0,20	Accept
Max IMF Bt	Absolute max electron density difference	0,1498	0,8835	<0,20	Accept
Max IMF Bt	Negative max electron density difference	0	-0,0026	<0,20	Accept
Max IMF Bt	Positive max electron density difference	0,1468	0,8653	<0,20	Accept
Max IMF Bz	Absolute max electron density difference	-0,0875	-0,5122	<0,20	Accept
Max IMF Bz	Negative max electron density difference	-0,1014	-0,5943	<0,20	Accept
Max IMF Bz	Positive max electron density difference	-0,1669	-0,9869	<0,20	Accept
Max dynamic pressure	Absolute max electron density difference	0,0812	0,4748	<0,20	Accept
Max dynamic pressure	Negative max electron density difference	0,0721	0,4218	<0,20	Accept
Max dynamic pressure	Positive max electron density difference	0,1353	0,7964	<0,20	Accept

5.2.4 Maximum dH/dt and solar wind parameters

In this section, the linear relationships between the maximum dH/dt of a storm and various solar wind parameters have been analyzed. The aim of this analysis is to determine whether the solar wind parameters affect the maximum dH/dt of a storm. The correlation coefficients, t-values, p-values and the acceptance of the null hypothesis is seen in the Table 5.8.

Table 5.8 : Pearson correlation coefficients, t-values, p-values, and acceptence of H0 for maximum dH/dt and solar wind parameters.

		r	t-value	p-value	H0
Max dH/dt	Max solar wind ion density	0,0293	0,1708	<0,20	Accept
Max dH/dt	Max solar wind velocity	0,3542	2,2085	0,02-0,05	Reject
Max dH/dt	Max IMF Bt	0,2133	1,2732	<0,20	Accept
Max dH/dt	Max IMF Bz	-0,19	-1,1283	<0,20	Accept
Max dH/dt	Max dynamic pressure	0,2927	1,7848	0,05-0,10	Accept

These parameters are ion density, velocity, IMF Bt, IMF Bz, and dynamic pressure and the correlation coefficients are 0.03, 0.35, 0.21, -0.19, and 0.29, respectively. Thus, among these correlation coefficients only the one between maximum dH/dt and the solar wind velocity is statistically significant and the scatter plot for this relationship is seen in the Figure 4.14. It can be concluded that the effect of the solar wind on the geomagnetic field cannot be seen directly with this analysis even though it knows that the reason behind the geomagnetic field variations is the solar wind.

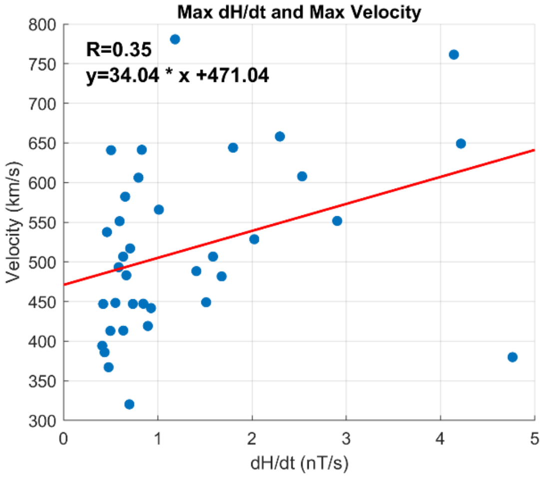

Figure 5.14 : Scatter plot of maximum dH/dt and maximum solar wind velocity.

5.2.5 Electric Field

In this part of the analysis the electric field components and their relationships with the geomagnetic indices are analyzed. The difference of this part is that the analyses are made with 10 samples which makes the critical t-value 2.306.

5.2.5.1 Geomagnetic indices and Ex

In this section, the relationships between the maximum Ex and geomagnetic indices have been analyzed. The aim of this analysis is to determine whether the strength of the northward electric field depends on the storm strength and if so which geomagnetic index is the best indicator. The correlation coefficients, t-values, p-values and the acceptance of the null hypothesis is seen in the Table 5.9.

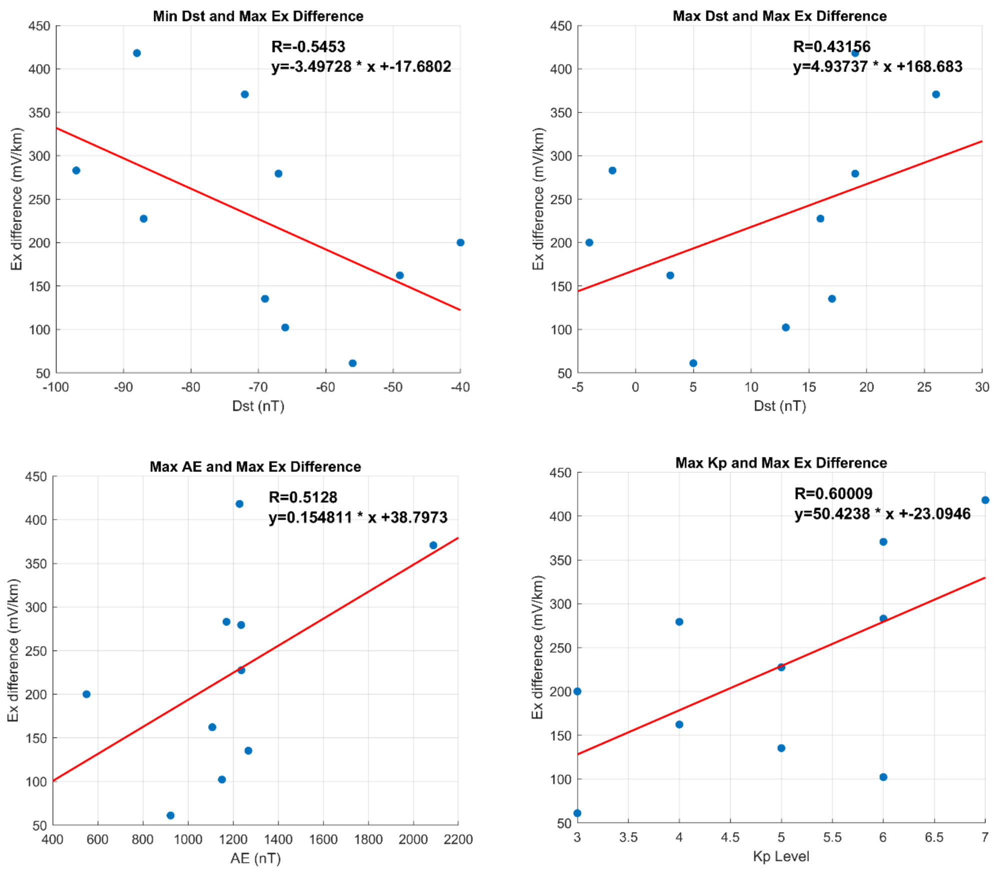

Figure 5.15 : Scatter plots of maximum Ex difference for minimum Dst, maximum Dst, maximum AE, and maximum Kp.

The correlation coefficients for all of the geomagnetic indices are statistically significant. The best relationship is between Kp level, and it is followed by minimum Dst. Thus it can be said that the electric field variations at mid-latitudes are affected by the geomagnetic storms and the variations increase as the storm strength increases. The scatter plots for these relationships can be seen in the Figure 5.14.

Table 5.9 : Pearson correlation coefficients, t-values, p-values, and acceptence of H0 for geomagnetic indices and Ex.

		r	t-value	p-value	H0
Min Dst	Max Ex difference	-0,5453	-3,7932	0,005-0,01	Reject
Max Dst (SC)	Max Ex difference	0,4316	2,7895	0,02-0,05	Reject
Max AE	Max Ex difference	0,5128	3,4829	0,005-0,01	Reject
Max Kp	Max Ex difference	0,6001	4,3743	0,002-0,005	Reject

5.2.5.2 Geomagnetic indices and Ey

In this section, the relationships between the maximum Ey and geomagnetic indices have been analyzed. The aim of this analysis is to determine whether the strength of the eastward electric field depends on the storm strength and if so which geomagnetic index is the best indicator. The correlation coefficients, t-values, p-values and the acceptance of the null hypothesis is seen in the Table 5.10.

Table 5.10 : Pearson correlation coefficients, t-values, p-values, and acceptence of H0 for geomagnetic indices and Ey.

		r	t-value	p-value	H0
Min Dst	Max Ey difference	-0,5702	-4,0475	0,002-0,005	Reject
Max Dst (SC)	Max Ey difference	0,3402	2,1096	0,05-0,1	Accept
Max AE	Max Ey difference	0,0366	0,2138	<0,20	Accept
Max Kp	Max Ey difference	0,486	3,2421	0,01-0,02	Reject

Based on the analysis, while the correlation coefficients for minimum Dst and Kp are statistically significant, the ones for maximum Dst and AE are statistically insignificant. As is was with the Ex, minimum Dst is shows the best relationship with the Ey variation. Thus, it can be said that at mid-latitudes the magnetospheric ring current is more dominant when it comes to the westward component of the electric field, and as the storm gets more intense, the westward electric field variation increases. The scatter plots for these relationships can be seen in the Figure 5.15.

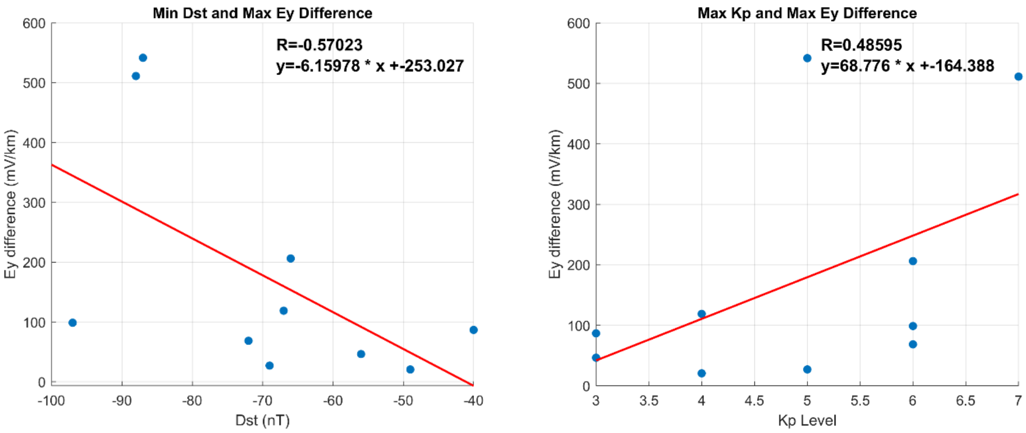

Figure 5.16 : Scatter plots of maximum Ey difference for minimum Dst and maximum Kp.

5.2.5.3 Verification of Faraday's law

In this section, Faraday's law has been tested for mid-latitudes. According to Faraday's law, Ex is closely related to dBy/dt, and Ey is closely related to dBx/dy. In order to test this, the maximums of each parameter for 10 cases have been analyzed. The correlation coefficients, t-values, p-values and the acceptance of the null hypothesis is seen in the Table 5.11.

Table 5.11 : Pearson correlation coefficients, t-values, p-values, and acceptence of H0 Ex and dBy/dt, Ey and dBx/dt.

		r	t-value	p-value	H0
Max Ex difference	Max dBy/dt	0,668	5,2336	>0,001	Reject
Max Ey difference	Max dBx/dt	0,455	2,9792	0,01-0,02	Reject

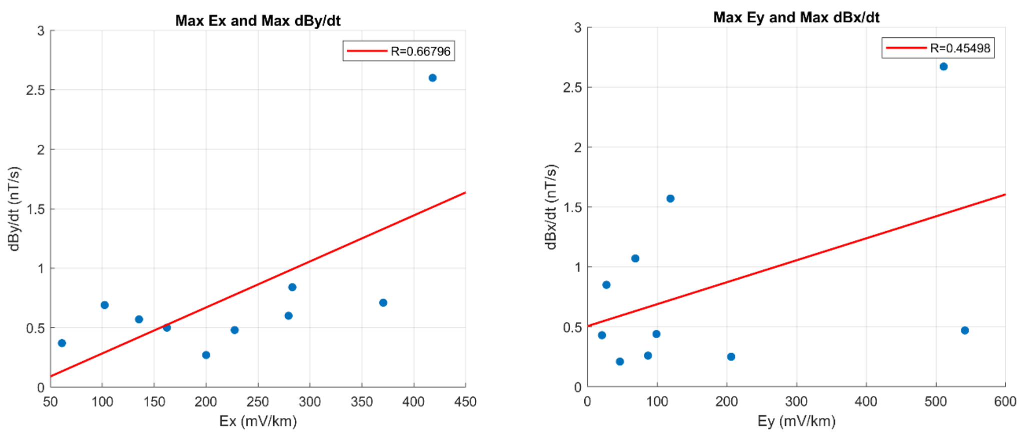

Figure 5.17 : Scatter plots of maximum Ex difference and maximum dBy/dt, maximum Ey difference and maximum dBx/dt.

Both of the correlation coefficients are statistically significant. The relationship between the maximum Ex and dBy/dt shows better correlation with 0.67, while the coefficient between Ey and dBx/dt is 0.45. Thus, it can be said that the Faraday's law is acceptable at mid-latitudes. . The scatter plots for these relationships can be seen in the Figure 5.16.

6. CONCLUSIONS AND FUTURE WORK

6.1 Summary and Conclusions

In thesis research, geomagnetically induced currents (GICs) have been investigated both in terms of case studies and statistically over the latitudes of Türkiye. The analyses were carried out in three parts depending on the availability of data sets. Table below gives the information about the data sets:

Tablo 6.1: Three main data sets and their details.

Group	Location	Type of Data	Variables	Resolution	Time Coverage	Source
1	Iznik 40°N, 29°E	Magnetic field	B_x, B_y, B_z, B_{total}	1 sec	2013-2015 Three years	Kandilli Observatory, Iznik
2	Bozcaada 39°N, 26°E	Magnetic field Electric field	B_x, B_y, B_z E_x, E_y	1 sec	2013-2014 Two years	ITU-UASWLab
3	Istanbul 41ºN, 28ºE	Ionospheric Electron density	F2 region critical frequency (foF2)	4 min, 2 min	2013-2015 Three years	ITU-UASWLab

These data were analyzed in order to find about the chracteristics of geomagnetically induces currents over our latitudes and the role of geomagnetic storms, solar wind plasma and interplanetary magnetic field. Three geomagnetic storm cases were selected and geomagnetic field and electric field data and the electron density data corresponding to these storms were analyzed first in a case basis. This is followed by the statistical analysis that covers 36 geomagnetic storms for the ground level magnetic field and ionospheric electron density data and 10 geomagnetic storms for the ground level electric field data. We present the results from the case studies as follows:

1) The main dH/dt fluctuations for the 17 March 2013 storm start with the sudden commencement and last throughout the main phase, and the maximum dH/dt is greater than 1 nT/s. Ionospheric electron density increases (positive effect) during the main phase.

2) The highest dH/dt value for the 27 February 2014 storm is seen during the recovery phase, yet the main fluctuation period is seen in the main phase. The ionospheric electron density difference between the quiet day is positive throughout the storm. Electric field components fluctuate during the main phase of the storm and they show great alignment with the time derivative of the horizontal components of the geomagnetic field as suggested by Faraday’s law.

3) The main fluctuations in dH/dt for the 9 September 2015 storm are seen in the early recovery phase. The maximum dH/dt is greater than 1 nT/s. Due to the CME arrival without a shock, the relationship between the solar wind parameters and the effects on the ground and ionospheric levels is not clear. The period where ionospheric electron density difference is at its maximum coincides with the main phase of the storm. During the main phase, the electron density decreases, thus, there is a negative effect.

4) The case studies show very good agreement with the solar wind parameters especially with IMF Bz and dynamic pressure, even though the same relationship in the statistical study is not as clear as in the case studies.

In 36 cases;

1) In 40% of them the maximum dH/dt is greater than 1 nT/s.

2) The maximum dH/dt of a storm is not seen around the peak of the storm where Dst reaches its maximum strength. In most of the cases, the maximum dH/dt is not seen around sudden commencement either.

3) 90% of the storms lasts less than 150 hours, and the average duration is 71 hours.

4) The average duration of the initial, main, and recovery phases are 5, 20, and 45 hours, respectively.

5) The average maximum dH/dt during the initial, main, and recovery phases are 0.45, 0.91, and 0.89 nT/s.

6) In half of the storms, the maximum dH/dt is seen during the recovery phase. In only one case the maximum dH/dt occurs during the initial phase.

7) The average absolute maximum ionospheric electron density difference between quiet and active days is 6.5×10^5 #/cc. In half of the cases, the maximum electron density difference is negative, and in the other half, it is positive. Thus; in mid-latitudes possibility of seeing positive and negative effects on ionospheric electron density is

equal. Additionally, the possibility of seeing a greater difference is higher when the effect is negative.

8) The Pearson correlation coefficients are calculated for 68 pairs in order to find whether there are linear relationships between them. The T-test is applied for all the pairs and 22 of them are statistically significant in 95% significance level.

9) The maximum dH/dt of a storm correlates the best with minimum Dst with a correlation coefficient of -0.48. There is no significant relationship between maximum dH/dt and the strength of the sudden commencement.

10) The maximum dH/dt does not occur at the most intense time of the storm which is when the Dst reaches its local minimum at mid-latitudes.

11) The storm strength directly affects the storm duration, more precisely the recovery phase duration. The stronger the storms, the longer the recovery phase.

12) Maksimum absolute electron differences are found to be correlated with the strength of peak Dst.

13) Northward electric fields correlate with all of the indices, while eastward component only shows correlation with minimum Dst and Kp.

14) Faraday's law is acceptable at mid-latitudes based on the correlation coefficients.

6.2 Future Work

In this thesis, geomagnetically induced currents were analyzed using the data available to us as comprehensive as possible. This is actually the first detailed investigation of GICs over midlatitudes in this region of the world. One of the points that needs to be further investigated is the correlations found during the recovery phase of the geomagnetic storms. Normally, the recovery phase of the storms is the stage where the geomagnetic activity in the magnetosphere ceases and the high correlations as also seen in this study are not expected to be seen. This is one of the main outcomes of this thesis. Obviously there are physical and dynamical processes even during the recovery phase and these need to be resolved. Secondly among the 69 parameters that the relationship between the solar wind and geomagnetic activity, many of the correlations are found to be much lower than the 95% significance level. Yet, while the case studies show excellent visual correlation with the solar wind plasma and IMF Bz, statistical studies are found below significance level. In this case we think that the proper quantity for the solar wind effects are not found. This could be and will be further investigated using better parameter for solar wind relation. Also advanced statistical methods such as superposed epoch analysis, machine learning techniques, wavelet analysis etc. to reveal the effects of the solar wind geomagnetic storms. New techniques are especially needed to understand the behaviour of dB/dt which shows rather peaky variations. In addition, in this study, we have focussed on understanding the general behaviour of dB/dt over midlatitudes and was not able to work and comment on the physical causes. Therefore, further study is required at this point especially to reveal the sources of dB/dt over our latitudes.

REFERENCES

Australian Space Academy. (n.d.). *The Ionosonde*. ttp://www.spaceacademy.net.au/ spacelab/tools/ionosonde.htm

Berényi, K. A., Barta, V., & Kis. (2018). Midlatitude ionospheric F2-layer response to eruptive solar events-caused geomagnetic disturbances over Hungary during the maximum of the solar cycle 24: A case study. *Advances in Space Research*, *61*(5), 1230–1243. https://doi.org/10.1016/J.ASR. 2017.12.021

Buresova, D., Franceschi, G. De, & Lastovicka, J. (2007). *Manifestation of Strong Geomagnetic Storms in the Ionosphere above Europe IN THE IONOSPHERE ABOVE EUROPE*. *May*. https://doi.org/10.1007/1-4020-5446-7

Celik, C., Tolak, E., Zobu, M., Sarikaya, N., & Kizmaz, A. I. (2013). The history and future of the geomagnetic observations in Kandilli Observatory & E.R.I., Turkey. *Conductivity Anomaly*, 31–40. http://www.eqh.dpri.kyoto-u.ac.jp/CA/2013/Celik_et_al_CA2013.pdf

ESA. (2018). *Space weather effects*. https://www.esa.int/ESA_Multimedia/Images/ 2018/01/Space_weather_effects

Fiori, R. A. D. ., Boteler, D. H. ., & Gillies, D. M. (2014). Assessment of GIC risk due to geomagnetic sudden commencements and identification of the current systems responsible. *Space Weather*, *12*(1), 1–109. https://doi.org/https://doi.org/10.1002/2013SW00096

Gerontidou, M., Mavromichalaki, H., & Daglis, T. (2018). High-Speed Solar Wind Streams and Geomagnetic Storms During Solar Cycle 24. *Solar Physics*, *293*(9). https://doi.org/10.1007/s11207-018-1348-8

GFZ Postdam. (n.d.). *What is the Kp index? - Space Weather*. Retrieved December 20, 2022, from https://spaceweather.gfz-potsdam.de/products-data/nowcasts/nowcast-kp-index/what-is-the-kp-index

Gonzalez, W. D., Joselyn, A., Kroehl, H. W., Ros, G., Tsuru, B. T., & Vasyliunas, V. M. (1994). *What is a geomagnetic storm ? 99*, 5771–5792.

Kalafatoglu, E. C., Kaymaz, Z., Moral, A. C., & Caglar, R. (2015). Geomagnetically induced current (GIC) observations of geomagnetic storms in Turkey: Preliminary results. *RAST 2015 - Proceedings of 7th International Conference on Recent Advances in Space Technologies*, 501–503. https://doi.org/10.1109/RAST.2015.7208396

Kalafatoğlu Eyigüler, E. C., & Kaymaz, Z. (2017). Magnetic and electric field variations during geomagnetically active days over Turkey. *Advances in Space Research*, *60*(9), 1921–1948. https://doi.org/ 10.1016/j.asr.2017.07.019

Kalkan, E. (2019). *spikeRemoval* (2.1.0.). MATLAB File Exchange. https://www.mathworks.com/ matlabcentral/fileexchange/69614-spikeremoval

Kappenman, J. G. (2003). Storm sudden commencement events and the associated geomagnetically induced current risks to ground-based systems at low-latitude and midlatitude locations. *Space Weather*, *1*(3), n/a-n/a. https://doi.org/10.1029/2003sw000009

Lastovicka, J. (1996). Effects of geomagnetic storms in the lower ionosphere, middle atmosphere and troposphere. *Journal of Atmospheric and Terrestrial Physics*, *58*(7), 831–843. https://doi.org/10.1016/0021-9169(95)00106-9

McElroy, M. B. (n.d.). *Ionosphere and Magnetosphere*. Retrieved December 1, 2022, from https://www.britannica.com/science/ionosphere-and-magnetosphere

Moral, A. C., Kaymaz, Z., Kalafatoglu Eyigüler, E. C., Zabotin, N., & Livingston, R. (2020). First results from ITU-Dynasonde, Istanbul, Turkey on the ionospheric characteristics. *Advances in Space Research*, *66*(11), 2537–2555. https://doi.org/10.1016/j.asr.2020.08.034

NASA. (n.d.-a). *CCMC DONKI*. Retrieved December 20, 2022, from https://kauai.ccmc.gsfc.nasa.gov/DONKI/

NASA. (n.d.-b). *SOHO Movie Theater*. Retrieved December 1, 2022, from https://soho.nascom.nasa.gov/data/Theater/

NASA. (n.d.-c). *SPDF - OMNIWeb Service*. Retrieved December 20, 2022, from https://omniweb.gsfc.nasa.gov/

NASA. (2012). *Coronal Hole on the Sun*. https://www.nasa.gov/multimedia/imagegallery/image_feature_2268.html

NASA. (2014). *NASA's SDO Observes an X-class Solar Flare*. https://www.nasa.gov/content/goddard/sdo-observes-an-x-class-solar-flare/

NASA. (2015). *Earth-like exoplanets may have magnetic fields capable of protecting life*. https://exoplanets.nasa.gov/news/217/earth-like-exoplanets-may-have-magnetic-fields-capable-of-protecting-life/

Natural Resources Canada. (2020). *Magnetic Components*. https://geomag.nrcan.gc.ca/mag_fld/comp-en.php

NOAA. (n.d.-a). *NOAA Space Weather Scales | NOAA / NWS Space Weather Prediction Center*. Retrieved December 20, 2022, from https://www.swpc.noaa.gov/noaa-scales-explanation

NOAA. (n.d.-b). *Planetary K-index | NOAA / NWS Space Weather Prediction Center*. Retrieved December 20, 2022, from https://www.swpc.noaa.gov/products/planetary-k-index

Odenwald, S. (2017). *The Day the Sun Brought Darkness*. https://www.nasa.gov/topics/earth/features/sun_darkness.html

Oyedokun, D. T. O., & Cilliers, P. J. (2018). Geomagnetically induced currents: A threat to modern power systems. In *Classical and Recent Aspects of Power System Optimization*. Elsevier Inc. https://doi.org/10.1016/B978-0-12-812441-3.00016-1

Partamies, N., Juusola, L., Tanskanen, E., & Kauristie, K. (2013). Statistical properties of substorms during different storm and solar cycle phases. *Annales Geophysicae, 31*(2), 349–358. https://doi.org/10.5194/angeo-31-349-2013

Pulkkinen, A., Lindahl, S., Viljanen, A., & Pirjola, R. (2005). Geomagnetic storm of 29-31 October 2003: Geomagnetically induced currents and their relation to problems in the Swedish high-voltage power transmission system. *Space Weather*, *3*(8). https://doi.org/10.1029/2004SW000123

Richardson, I. G., & Cane, H. V. (2012). Solar wind drivers of geomagnetic storms during more than four solar cycles. *Journal of Space Weather and Space Climate*, *2*, 1–9. https://doi.org/10.1051/swsc/2012001

Scott, C. (2022). *Climate Change In The Ionosphere*. https://blogs.reading.ac.uk/weather-and-climate-at-reading/2022/climate-change-in-the-ionosphere

Solomon, O. M., Larson, D. R., & Paulter, N. G. (2001). Comparison of some algorithms to estimate the low and high state level of pulses. *Conference Record - IEEE Instrumentation and Measurement Technology Conference*, *1*, 96–101. https://doi.org/10.1109/IMTC.2001.928794

t-distribution table (two-tailed). (n.d.). Retrieved December 19, 2022, from https://www.medcalc.org/manual/t-distribution-table.php

Turney, S. (2022). *Pearson Correlation Coefficient (r) | Guide & Examples*. https://www.scribbr.com/statistics/pearson-correlation-coefficient/

UCAR. (2012). *"Parts" of the Sun*. https://scied.ucar.edu/learning-zone/sun-space-weather/sun-regions

United States Geological Survey. (n.d.). *Geomagnetic field*. Retrieved December 1, 2022, from https://ec.europa.eu/health/scientific_committees/opinions_layman/en/electromagnetic-fields07/glossary/ghi/geomagnetic-field.htm

Viljanen, A., Nevanlinna, H., Pajunpää, K., & Pulkkinen, A. (2001a). Time derivative of the horizontal geomagnetic field as an activity indicator. *Annales Geophysicae*, *19*(9), 1107–1118. https://doi.org/10.5194/angeo-19-1107-2001

Viljanen, A., Nevanlinna, H., Pajunpää, K., & Pulkkinen, A. (2001b). Time derivative of the horizontal geomagnetic field as an activity indicator. *Annales Geophysicae*, 1107–1118. https://doi.org/10.5194/angeo-19-1107-2001

Viljanen, A., Tanskanen, E. I., & Pulkkinen, A. (2006). Relation between substorm characteristics and rapid temporal variations of the ground magnetic field. *Annales Geophysicae*, *24*(2), 725–733. https://doi.org/10.5194/angeo-24-725-2006

Zhang, J. J., Wang, C., Sun, T. R., Liu, C. M., & Wang, K. R. (2015). GIC due to storm sudden commencement in low-latitude high-voltage power network in China: Observation and simulation. *Space Weather*, *13*(10), 643–655. https://doi.org/10.1002/2015SW001263

CURRICULUM VITAE

Name Surname **:** Ezgi GÜLAY

EDUCATION **:**

- **B.Sc.** **:** 2020, Istanbul Technical University, Faculty of Aeronautics and Astronautics, Meteorological Engineering

LIST OF PRESENTATIONS

Gülay, E., Kaymaz, Z., Kalafatoğlu, E. C. (2022, October 24-28). *Investigation of Ionospheric and Ground Level Signatures of Space Weather over Turkey* [Conference presentation]. 18th European Space Weather Week, Zagreb, Croatia.

Gülay, E., Kaymaz, Z., Kalafatoğlu, E. C. (2022, July 11-15). *Investigation of Ionospheric and Ground Level Effects of Space Weather over Turkey* [Virtual oral presentation]. 8th Workshop on Vertical Coupling in the Atmosphere-Ionosphere System, Sopron, Hungary.

Gülay, E., Kaymaz, Z., Kalafatoğlu, E. C. (2022, June 13-15). *Investigation of Ionospheric and Ground Level Effects of Space Weather over Turkey* [Poster presentation]. 8th International HEPPA-SOLARIS Meeting, Bergen, Norway.

Gülay, E., Kaymaz, Z., Kalafatoğlu, E. C. (2022, May 23-27). *Investigation of Ionospheric and Ground Level Signatures of Geomagnetic Storm over Turkey* [Oral presentation]. EGU General Assembly, Vienna, Austria.

Gülay, E., Kaymaz, Z., Kalafatoğlu, E. C. (2021, August 21-27). *Variations in Ground Magnetic Field and Ionospheric Electron Density over Turkey during Geomagnetically Disturbed Days* [Virtual poster presentation]. IAGA-IASPEI 2021 Virtual Conference, Virtual.

Gülay, E., Kaymaz, Z., Kalafatoğlu, E. C. (2021, March 8-12). *Geomagnetic Field Variations During Quiet and Disturbed Days Over Iznik, Turkey* [Virtual oral presentation]. 3rd ISEE Symposium PWING-ERG Conference and School on the Inner Magnetosphere, Nagoya, Japan.